A study of interplanetary shock geoeffectiveness controlled by impact angles using simulations and observations

BY

DENNY M. OLIVEIRA

B.S., University of São Paulo (2005)

M.S., University of São Paulo (2010)

DISSERTATION

Submitted to the University of New Hampshire
in partial fulfillment of
the requirements for the degree of

Doctor of Philosophy

in

Physics

April, 2015

This dissertation has been examined and approved in partial fulfillment of the requirements for the degree of Doctor of Philosophy in Physics by:

Dissertation Director, Joachim Raeder
Professor of Physics

Charlie Farrugia
Research Professor of Physics

Martin Lee
Professor of Physics

Benjamin Chandran
Professor of Physics

Karsten Pohl
Professor of Physics

On April 16, 2015

Original approval signatures are on file with the University of New Hampshire Graduate School.

Dedication

To my wife Patricia and my daughters, Isabela and Eduarda.

Acknowledgments

I could write names of so many people in this section! I would like to thank my adviser, Professor Joachim “Jimmy” Raeder, for the way you conducted me on the road to reach this point. You gave me the opportunity to think and freely explore this branch of space physics research. Thank you for sending me out to summer schools, meetings, workshops, and conferences (even in Japan!), where I had the opportunity to have contact with the cutting-edge science and discussions. The opportunity of meeting researchers of our field had a remarkable importance in my career as a researcher and scientist. Thank you Jimmy for teaching me how to write scientific papers (I am not saying I learned it). With your encouragement to use the SuperMAG data, I was able to get the results that correspond to Chapter 6 of this dissertation and two published papers.

I would like to thank the members of my thesis committee, which was composed by Professor Karsten Pohl, Professor Benjamin Chandran, Professor Martin Lee, and Professor Charlie Farrugia. I had the pleasure to have most of you as my instructors in my Ph.D. program, with exception to Ben who was my supervisor in my first year as a TA. Thank you for all your lectures, instructions, and comments, from classroom, thesis proposal defense, to my final defense.

Concerning the computational aspect of this work, I would like to thank specially two people: Matthew Gilson and Kris Maynard. Matt, your pyggcm package and the pyprobe package you presented to me were of fundamental importance in the plotting of figures for my first paper. Kris, your answers for my python questions helped me to move fast and get the data ready for analysis. Without your help, this work would have taken longer to be accomplished. Thank you my colleagues in graduate school: Kristoff, Sam, Kyle, Steve, and others. Your help with homework and TA assignments were of crucial importance to me. Your tips on English language were also important at the beginning of my journey in the U.S.

There are three people in Brazil who deserve credit here: Professor Adílson José da Silva, Professor Marcelo Gomes, and Professor Emerson Passos. You all have my gratitude for your lectures and discussions in my undergraduation and my master's. Thank you for encouraging me to adventure in this country and take a long road called doctorate program.

This work would not have been completed without the financial support by grant NNX13AK31G from NASA, grant AGS-1143895 from the National Science Foundation, and grant FA-9550-120264 from the Air Force Office of Sponsored Research. I would like to thank the WIND and ACE teams for providing their data through NASA's CDAWeb interface, which definitely sped up the completion of this work. For the ground magnetometer data I gratefully acknowledge a bunch of people: Intermagnet; USGS, Jeffrey J. Love; CARISMA, PI Ian Mann; CANMOS; The S-RAMP Database, PI K. Yumoto and Dr. K. Shiokawa; The SPIDR database; AARI, PI Oleg Troshichev; The MACCS program, PI M. Engebretson, Geomagnetism Unit of the Geological Survey of Canada; GIMA; MEASURE, UCLA IGPP and Florida Institute of Technology; SAMBA, PI Eftyhia Zesta; 210 Chain, PI K. Yumoto; SAMNET, PI Farideh Honary; The institutes who maintain the IMAGE magnetometer array, PI Eija Tanskanen; PENGUIN; AUTUMN, PI Martin Conners; DTU Space, PI Dr. Jrgen Matzka; South Pole and McMurdo Magnetometer, PI's Louis J. Lanzarotti and Alan T. Weatherwax; ICESTAR; RAPIDMAG; PENGUIn; British Artarctic Survey; McMac, PI Dr. Peter Chi; BGS, PI Dr. Susan Macmillan; Pushkov Institute of Terrestrial Magnetism, Ionosphere and Radio Wave Propagation (IZMIRAN); GFZ, PI Dr. Jrgen Matzka; MFGI, PI B. Heilig; IGFPAS, PI J. Reda; University of LAquila, PI M. Vellante; SuperMAG, PI Jesper W. Gjerloev. Specially I say thank you to the SuperMAG

PI J. W. Gjerloev for the straightforward SuperMAG website and its convenience of data visualization and download.

My highest gratitude goes to my family. Patricia, your support during these years made this work happen. Thank you for watching the girls while I was traveling. When I said it was not possible, you said yes, it is possible. In all these years you have been at my side, you have been the fuel of my existence. I had been a student since we met each other. Finally this cycle has ended. Thank you so much for your love and patience!

Isabela and Eduarda, I hope I make you proud when you read these lines in the future. Your curiosity and questions about science really make me proud. Your knowledge about the solar system at your ages is really impressive. I hope both of you grow not only in age, but also in wisdom and knowledge.

I would like to say thank you to my parents as well. Thank you for your support during the years of my undergraduation. Dad, I wish you could read those lines. But something inside of me makes me think you are proud of me, wherever you are in this universe.

Table of Contents

List of Tables

List of Figures

ABSTRACT

A study of interplanetary shock geoeffectiveness controlled by impact angles using simulations and observations

by

Denny M. Oliveira

University of New Hampshire, April, 2015

In this dissertation, we study the influence of interplanetary (IP) shock impact angles in the IP shock geoeffectiveness focusing on simulations and observations. In our simulations, we use OpenGGCM global MHD code to study the nightside magnetospheric, magnetotail, and ionospheric responses to IP fast forward shocks. Three cases are presented in this study: two inclined oblique shocks, hereafter IOS-1 and IOS-2, where the latter has a Mach number twice stronger than the former. Both shocks have impact angles of 30^o in relation to the Sun-Earth line. Lastly, we choose a frontal perpendicular shock, FPS, whose shock normal is along the Sun-Earth line, with the same Mach number as IOS-1. We find that, in the IOS-1 case, due to the north-south asymmetry, the magnetotail is deflected southward, leading to a mild compression. The geomagnetic activity observed in the nightside ionosphere is then weak. On the other hand, in the head-on case, the FPS compresses the magnetotail from both sides symmetrically. This compression triggers a substorm allowing a larger amount of stored energy in the magnetotail to be released to the nightside ionosphere, resulting in stronger geomagnetic activity. By comparing IOS-2 and FPS, we find that, despite the IOS-2 having a larger Mach number, the FPS leads to a larger geomagnetic response in the nightside ionosphere. As a result, we conclude that IP shocks with similar upstream conditions, such as magnetic field, speed, density, and Mach number, can have different geoeffectiveness, depending on their shock normal orientation. In the second part of this dissertation, we present a survey of fast forward IP shocks using WIND and ACE satellite data from January 1995 to December 2013 to study how IP shock geoeffectiveness is controlled by IP shock impact angles. A shock list covering one and a half solar cycle is compiled. The yearly number of IP shocks is found to correlate well with the monthly sunspot number. We use data from SuperMAG, a large chain with more than 300 geomagnetic stations, to study geoeffectiveness triggered by IP shocks. The SuperMAG SML and SME indices, enhanced versions of the familiar AL and AE indices, are used in our statistical analyses to quantify substorm strength and auroral power (AP) intensity, respectively. The jumps of the SML index and the calculated AP intensity triggered by IP shock impacts on the Earth's magnetosphere are investigated in terms of IP shock orientation and speed. We find that, in general, strong (high speed) and almost frontal (shock normal almost parallel to the Sun-Earth line) shocks are more geoeffective than inclined shocks with low speed. The highest correlations (correlation coefficient R = 0.78 for SML, and R = 0.79 for AP) occur for fixed IP shock speed and varying the IP shock impact angle. We attribute this result, predicted previously by simulations, to the fact that frontal shocks compress the magnetosphere symmetrically from all sides, which is a favorable condition for the release of magnetic energy stored in the magnetotail, which in turn can produce moderate to strong auroral substorms, which are then observed by ground based magnetometers. These results confirm our previous numerical simulations.

Chapter 1

Introduction

1.1 The heliosphere, the sun, and the solar wind

The discipline originally called solar-terrestrial physics has been expanded to regions beyond the near-Earth space environment. The modern magnetospheric physics, the discipline that studies the interaction of phenomena that originate at the Sun with the Earth's magnetic field, is only a small section of a much broader (and more recent) discipline, called heliophysics. The heliosphere is the region in space whose frontiers reach out the vicinity of the interstellar space. In July 2013, the *Science* journal published a series of papers in which researchers speculated whether or not Voyager 1 had reached the limits of the heliosphere by crossing the edges of the heliosheath and the interstellar medium [see, e.g. *Burlaga et al.*, 2013; *Krimigis et al.*, 2013]. *Gloecker and Fisk* [2014] suggested that Voyager 1 may cross a new limit in the heliosphere still in this year of 2015, which in fact leaves this question still open to discussions.

The Sun is at the center of the heliosphere. The understanding of the solar dynamics is important because the Sun is the closest star to Earth. For example, it is known today that the solar activity has a cycle of approximately 11 years, which varies accordingly to the number of sunspots observed on the Sun. The time period between a solar minimum (low sunspot number), passing by a solar maximum (high sunspot number), and then another solar minimum defines a solar cycle. Observations of sunspot number variations for more than 400 years have shown that the solar cycle influences geomagnetic activity at Earth [*Eddy*, 1976]. This star is a gigantic reservoir of ionized particles and strong variable magnetic field. The strength of sunspot magnetic fields is about 0.3 T, or approximately 10,000 times the field strength at Earth. The corona, the Sun's outer atmosphere, is hotter than the visible layer which is located in the solar disk. Because the temperature in the solar corona is higher than the temperature in the lower layers, electrons of atoms in it are constantly knocked off the nuclei to form a constantly flowing gas, called the solar wind, that travels toward the frontiers of the heliosphere [*Schrijver and Siscoe*, 2009]. The term solar wind was coined by Eugene Parker in his theoretical papers from the 1950s and 1960s [see, eg. *Parker*, 1958, 1961]. Parker was influenced by Chapman and Ferraro's work (see next section) and the work of *Biermann* [1957], who observed that comet tails were directed oppositely to the Sun. Parker found several solutions for the expanding gas from the solar corona and chose the one whose thermal pressure goes to zero at infinity, in which the outflow becomes supersonic at large distances from the Sun.

The solar wind contains mostly electrons and positive particles, with 95% of protons and 5% of alpha particles and heavier ions. Positive and negative particles are closely at the same number, which makes the space plasma a quasi-neutral gas. The first measurements of the solar wind, as a confirmation to Parker's theory, was made by instruments onboard the Mariner 2 spacecraft as reported by *Neugebauer and Snyder* [1962]. The solar wind speed changes from approximately 200 km/s to 800 km/s, with average of 400 km/s at 1 AU, or at the Earth's orbit, depending on the solar cycle [*Marsch*, 2006]. The solar wind speed was found to increase in regions of high solar latitudes [*McComas et al.*, 2003]. The solar wind density has been observed to be even more variable, ranging from 0.1 cm^{-3} to 100 cm^{-3} [*Newbury*, 2000; *Russell*, 2001]. Typical values for the solar wind density at 1

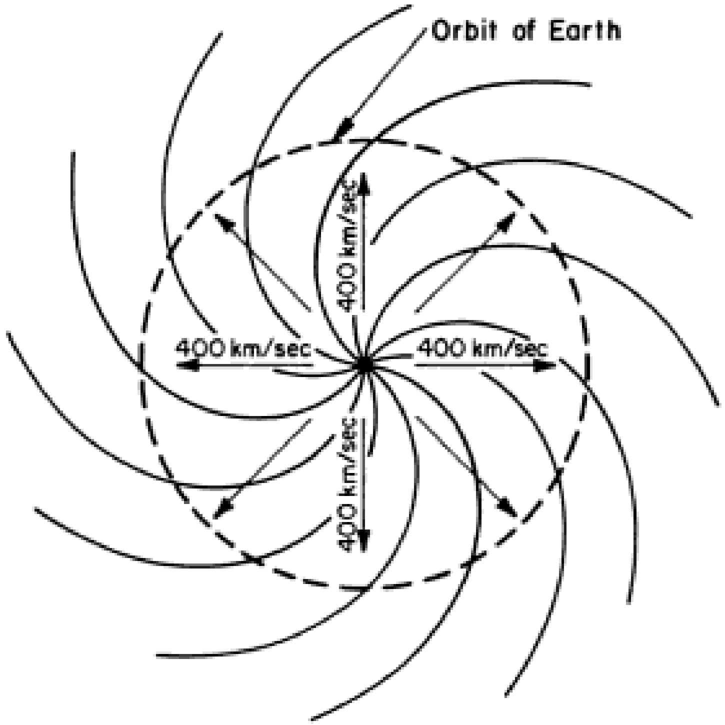

Figure 1-1: The Parker spiral, as suggested by *Parker* [1958]. Figure from *Kivelson and Russell* [1996].

AU are 5 cm^{-3} [*Russell*, 2001]. The plasma beta, the ratio of the thermal pressure to the magnetic pressure is generally between 0.4 and 0.8 for the solar wind near Earth [*Eastwood et al.*, 2014]. The Mach number (either Alfvén or magnetosonic) often lies between 6 and 12 at 1 AU.

The solar wind is a plasma with large electric conductivity. In the limit of infinity conductivity, a theorem, first introduced by *Alfvén* [1942], states that the magnetic field lines of the fluid are attached to it, or *frozen-in*, and are forced to propagate throughout the heliosphere with the solar wind. The Interplanetary Magnetic Field (IMF) has the shape of the Parker spiral, as shown in Figure 1-1. The IMF then flows at a speed of 400 km/s throughout the heliosphere with the solar wind. At 1 AU, the angle between the IMF and the Sun-Earth line is 45^o on average [*Parker*, 1963]. The interaction of this plasma (solar wind and IMF) with the Earth's geospace environment corresponds to the key point in

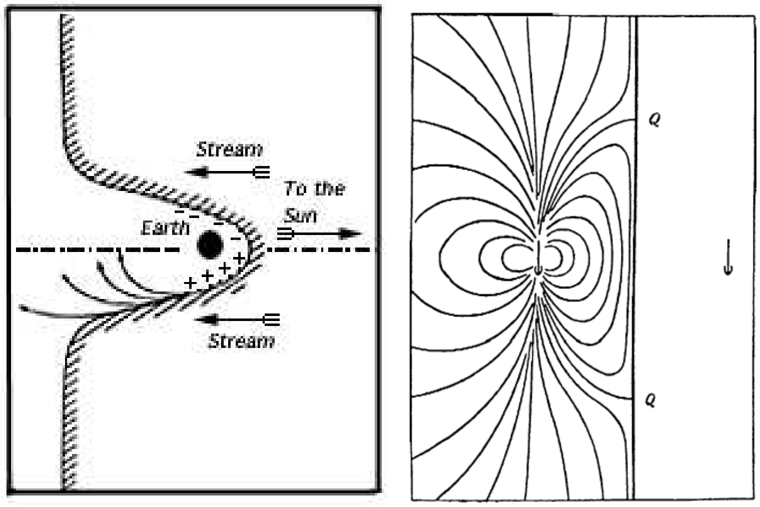

Figure 1-2: The Chapman-Ferraro cavity and dipole. Figures published by *Chapman and Bartels* [1940] and downloaded from `http://www-spof.gsfc.nasa.gov/Education/bh1-3.html`.

studying magnetospheric physics. The first observations of the IMF were made by *Sonett et al.* [1960] using data from instruments onboard the spacecraft Pioneer 5. The magnitude of the IMF is also variable at 1 AU. High values of the IMF are found in periods of solar maximum [*Luhmann et al.*, 1993; *Russell*, 2001]. The IMF strength is typically measured as 5 nT at 1 AU [*Russell*, 2001].

1.2 The Earth's magnetosphere

It is known since long ago that the Earth emits a magnetic field from its interior [*Gilbert*, 1600]. Near the Earth's surface this field behaves like a dipole field, and its existence is believed to be due to motion of electrically charged material inside the core [*Jacobs*, 1984] explained by a dynamo mechanism [*Buffett*, 2000; *Stacey and Davis*, 2008]. In the regions farther away from the Earth's surface, this field interacts with the solar wind. As the solar wind impinges on the dipole field, an electric current, known today as the "Chapman-Ferraro current", is formed due to the $\mathbf{J}\times\mathbf{B}$ force in the plasma front [*Chapman and Ferraro*, 1931a,b]. This current switches off the Earth's field. The Chapman-Ferraro

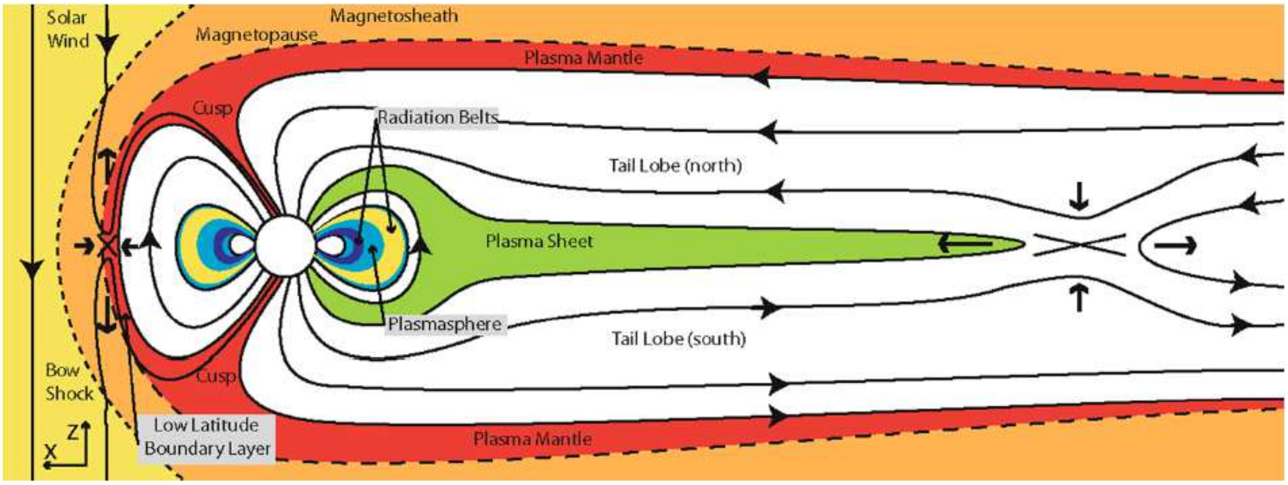

Figure 1-3: Noon-meridian cut representation of the Earth's magnetosphere, with some of its main regions. Figure extracted from *Eastwood et al.* [2014].

dipole is represented in the right-hand-side of Figure 1-2 from *Chapman and Bartels* [1940]. The $\mathbf{J}\times\mathbf{B}$ force slows down the plasma and compresses the dipole field, increasing the Earth's field magnitude. That was Chapman and Ferraro's explanation for a phenomenon called storm sudden commencement (SSC), which is a step-like increase of the geomagnetic field strength. This theory was supported by *Cahill and Amazeen* [1963] who studied magnetometer data onboard the Explorer 12 spacecraft.

The presence of the dipole field poses an obstacle to the solar wind flow. As the solar wind moves around this obstacle, the "Chapman-Ferraro cavity" is formed, as first suggested by *Chapman and Ferraro* [1930, 1931a,b, 1932]. Their first conception of this cavity is shown in Figure 1-2, left-hand-side. The plasma motion around this cavity was later explained by *Gold* [1959]. In that paper, Gold suggested to call the limit layer of the magnetic field domain the "magnetosphere". That was the first time the term magnetosphere appeared in the literature. A schematic representation of the magnetosphere in the noon-meridian plan, with its main regions, is shown in Figure 1-3.

The IMF topology plays an important role in the magnetospheric dynamics. As suggested by J. W. Dungey in his seminal works [*Dungey*, 1961, 1963], the z component of

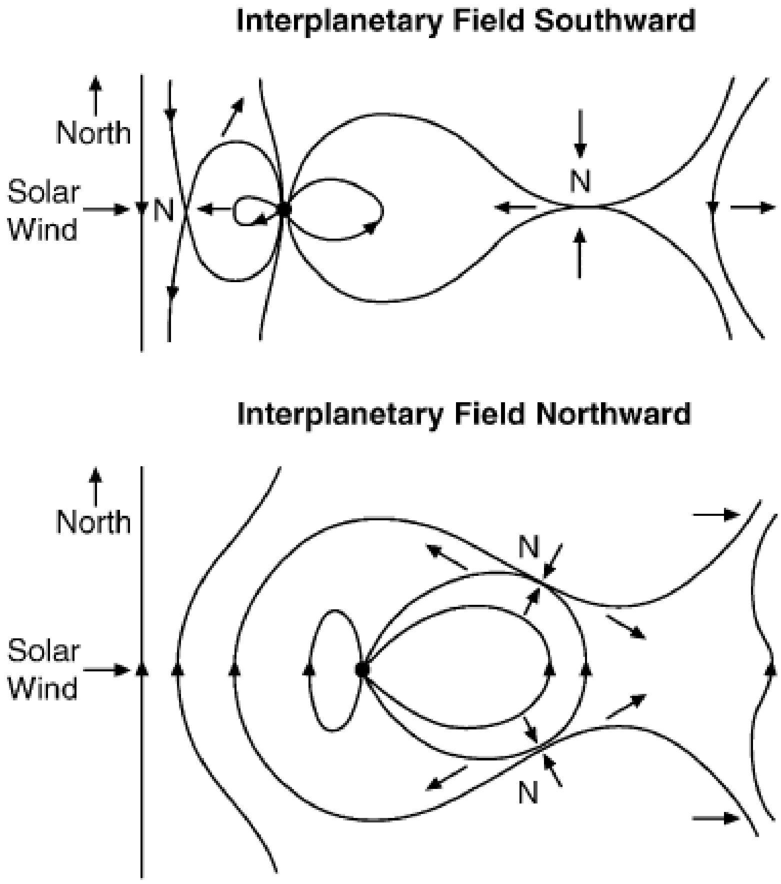

Figure 1-4: Model of open (top) and closed (bottom) terrestrial magnetic field as proposed by *Dungey* [1961, 1963]. In the first case, reconnection takes place in two different locations indicated by "N", the neutral point: the dayside magnetopause and the magnetotail.

the IMF, or IMF B_z, determines whether magnetic reconnection at the dayside magnetopause occurs or not. Magnetic reconnection is a phenomenon in which magnetic field lines of oppositely direction interact with each other and release magnetic energy [*Gurnett and Bhattacharjee*, 2005]. When the IMF B_z is southward, magnetic reconnection at the dayside magnetopause occurs. Then, according to Dungey's model, the magnetosphere is said to be open, particles can be accelerated and access low regions of the ionosphere, and what is known today as simply substorms may occur due to the nightside reconnection [*Dungey*, 1961, 1963]. Figure 1-4 represents this model. For the cases in which B_z is northward, the magnetosphere is said to be closed, and access of plasma into the magnetosphere is drastically reduced.

The solar wind interaction with the Earth's magnetosphere from a modern perspective is shown in Figure 1-5 from *Boyd and Sanderson* [2003]. Solid lines indicate the IMF direction, and arrowed lines indicate plasma flow. In that case, IMF B_z is southward and magnetic reconnection takes place at the nose of the magnetopause.

1.3 Collisionless shocks in the solar wind

Gold [1955] suggested in a conference held in Cambridge, England, that geomagnetic SSCs result from interplanetary (IP) shocks that generate jumps in interplanetary gas (plasma) velocity, magnetic field, thermal pressure, and density. Such disturbances are heliospheric structures of large scale. According to Gold's words,

> I should like to discuss, in connection with the subject of shock waves, some of the magnetic disturbances on the Earth that are caused by solar outbursts. The initial magnetic disturbance at Sudden Commencement of a magnetic storm can be accounted for very roughly by an increase of pressure of the tenuous gas around the Earth. This increase of pressure may perhaps be described as the effect of a wave sent out by the Sun through the tenuous medium between Sun and Earth. In the complete absence of any such medium this description would then correspond to that of a stream of particles, while in the presence of a medium the correct description may lie anywhere between an acoustic wave, a supersonic shock wave or an unimpeded corpuscular stream. The observations of magnetic storms may hence give us a fairly direct proof of the existence of shock waves in the interplanetary medium.

The possibility of the existence of shocks in the interplanetary space was then accepted.

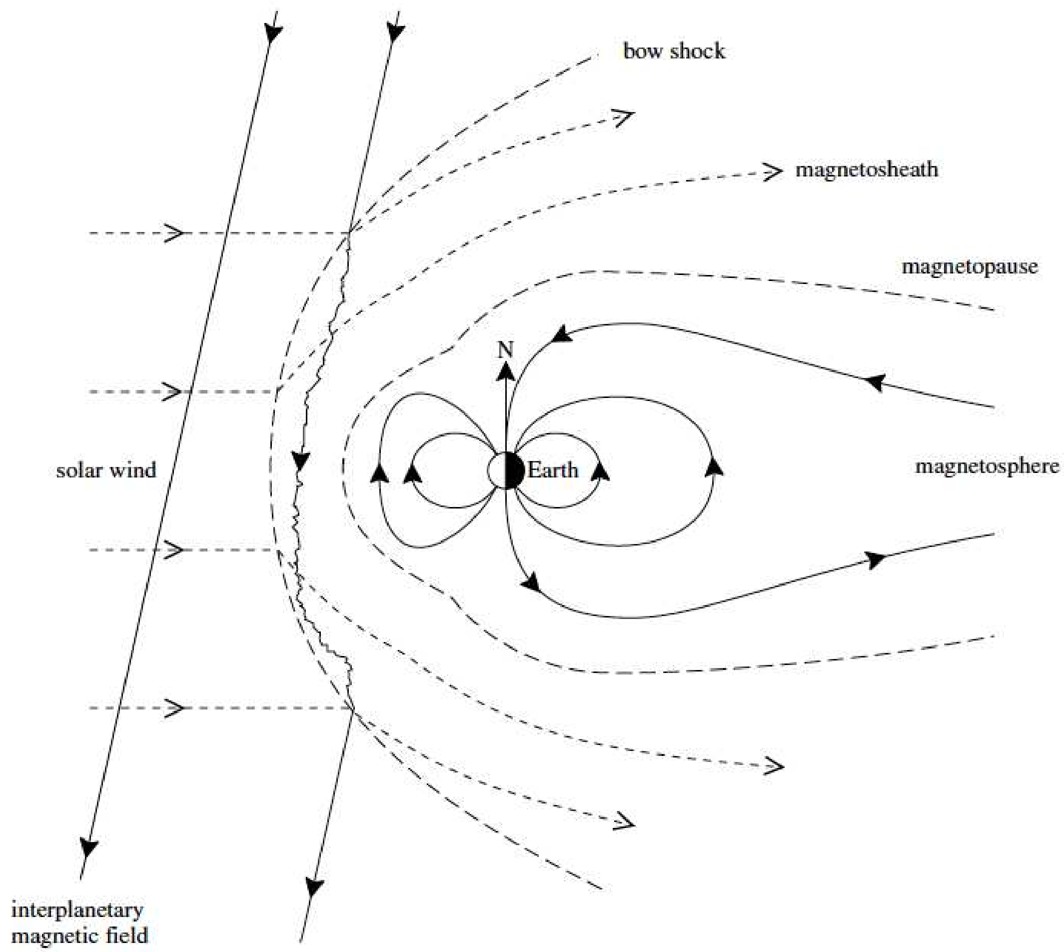

Figure 1-5: Interaction of the solar wind and the Earth's magnetosphere. Solid lines show IMF direction, and arrowed lines indicate plasma flow. Figure from *Boyd and Sanderson* [2003].

Parker [1961] suggested a model for shock propagation in the interplanetary space. His idea was further extended by *Hundhausen and Gentry* [1969]. Although the existence of collisionless shocks were suggested theoretically [for a historical perspective, see, e.g., *Balogh and Treumann*, 2013, Chapter 2], the first evidences of collisionless shocks in nature were observed in the interplanetary space. As seen above, the existence of the magnetosphere suggested the formation of a stationary collisionless shock at the front of the magnetosphere. Curiously, the existence of a stationary shock, i.e., a shock at rest in the Earth's reference frame, was suggested in the same edition of the *Journal of Geophysical Research* by *Axford* [1962] and *Kellog* [1962]. The bow shock was first observed by *Sonett and Abrams* [1963] and *Ness et al.* [1964]. The bow shock is the region in which the solar wind becomes subsonic. Another limit in the magnetosphere is the magnetopause, a region where the solar wind pressure is balanced by the Earth's magnetic field pressure. The region between the bow shock and the magnetopause is called the magnetosheath. The magnetosheath nose is located approximately between $10R_E$ to $13R_E$ toward the Sun from the Earth. This region is highly turbulent because it is mainly composed by the shocked solar wind [*Paschmann et al.*, 2005]. The bow shock, the magnetopause, and the magnetosheath are shown in Figure 1-3. After the first bow shock observations, the concevtive gas dynamic model by *Spreiter et al.* [1966] predicted a bow shock formation and a magnetosheath flow between the shock and the obstacle without MHD (magnetohydrodynamic) formalism.

1.4 Shocks in the heliosphere at 1 AU

IP shocks are ubiquitous features of the solar wind. IP shocks occur throughout the heliosphere as a result of the interaction of solar disturbances with the solar wind [*Burlaga*, 1971; *Hundhaunsen*, 1972a,b; *Richter et al.*, 1985]. As they encounter Earth they interact with the magnetosphere, causing disturbances that can be seen everywhere in the magneto-

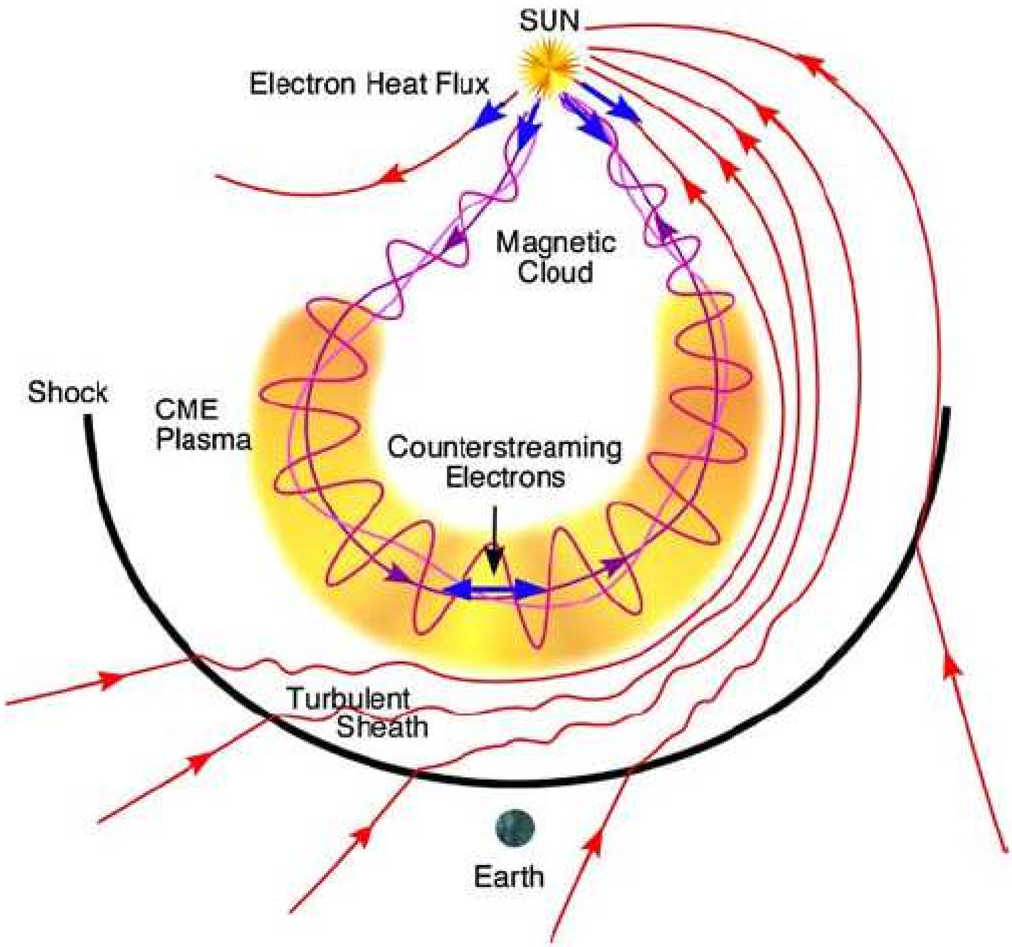

Figure 1-6: Schematic representation of a shock formation in front of an ICME, as shown in *Zurbuchen and Richardson* [2006]

sphere. Because the disturbances alter the magnetospheric current systems, the ionosphere is also affected, and the magnetic field on the ground is perturbed as well. The most dramatic shock-induced ground perturbations are the SSCs [*Chao and Lepping*, 1974; *Smith et al.*, 1986]. SSCs are driven by a strong IP shock preceding a geomagnetic storm driven by coronal mass ejections (CMEs) [*Gonzalez et al.*, 1994].

Early works [*Schieldge and Siscoe*, 1970; *Kawasaki et al.*, 1971; *Burch*, 1972; *Kokubun et al.*, 1977; *Akasofu and Chao*, 1980] associated geomagnetic activity with the appearance of SSCs. For example, *Kokubun et al.* [1977] examined geomagnetic activity following SSC events and concluded that events with intense auroral activity always occurred when SSC amplitudes were greater than 40 nT. *Smith et al.* [1986] showed that ∼80-90% of shocks caused SSCs. Therefore, the statements of geomagnetic activity following either SSC or IP shock events are similar arguments.

The interaction of IP shocks with the Earth's magnetosphere is both complex and important. For example, the shock-shock interactions such as between an IP shock and the Earth's bow shock may occur in many contexts, for example, in the heliosphere and in astrophysical systems. Such remote interactions are difficult to observe, but can be readily observed with in-situ measurements in the magnetosphere. On the other hand, strong IP shock impacts on the magnetosphere have substantial space weather effects, for example, they produce geomagnetically induced currents (GICs), which can impact power grids [*Bolduc*, 2002; *Kappenman*, 2010] leading so severe economic losses [*Schrijver et al.*, 2014], and they can energize particles in the inner magnetosphere [*Hudson et al.*, 1997; *Zong et al.*, 2009]. *Echer et al.* [2004] reported that 22% of all interplanetary shocks are intensely geoeffective while 35% are moderately geoeffective. Thus, the study of IP shock impacts is of fundamental and also of practical importance.

At 1 AU IP shocks are almost exclusively fast shocks. Slow shocks may exist at closer

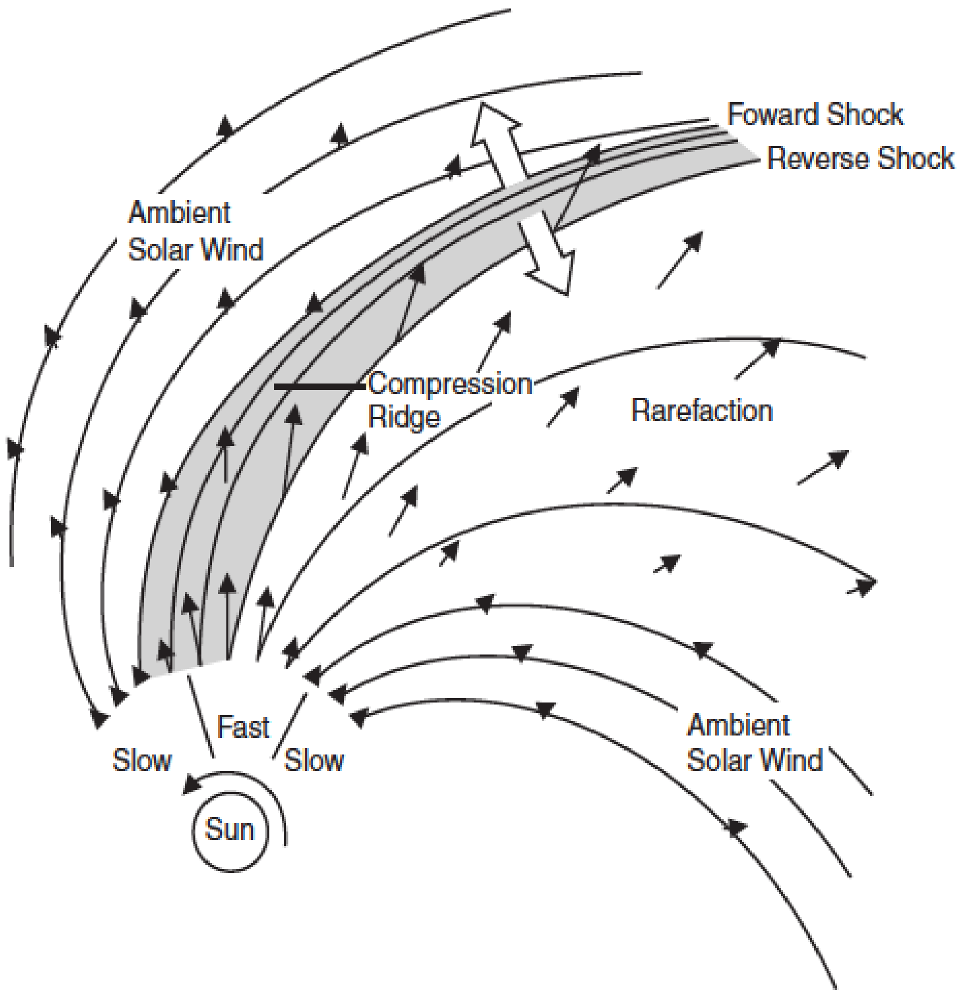

Figure 1-7: Schematic representation of the stream interaction in the inertial frame after *Pizzo* [1978]. When the difference between the fast and slow streams becomes greater than the magnetosonic speed of the medium, a shock may occur. Figure from *Russell* [2005].

distances to the Sun according to theoretical [*Whang*, 1982, 1983], simulation [*Hada and Kennel*, 1985; *Wu et al.*, 1996], and observational [*Chao and Olbert*, 1970; *Burlaga and Chao*, 1971; *Whang et al.*, 1996] results, but they are subject to Landau damping [*Richter et al.*, 1985]. IP shocks may further be classified as propagating away from the Sun, i.e., forward shocks, or as propagating towards the Sun, i.e., so-called reverse shocks. Since the solar wind speed is almost always supermagnetosonic, a reverse shock will still propagate away from the Sun in the Earth's frame. IP shocks may then be further classified by their strength, i.e., their Mach number in the solar wind reference frame, their orientation, and by the orientation of their upstream field with respect to the shock normal. The compression ratio, i.e., the ratio of downstream to upstream plasma density, is an alternative measure for the shock strength, which is often more convenient to use than the Mach number. Assuming a γ (specific heat ratio) of 5/3 appropriate for a monoatomic gas, the compression ratio must lie between 1 and 4 [*Priest*, 1981]. IP shocks are typically weak (compared to planetary bow shocks) with a compression ratio between 1.2 and 2 [*Berdichevsky et al.*, 2000]. The Rankine-Hugoniot relations provide the jump conditions between the upstream and downstream plasma parameters in the MHD context [*Jeffrey and Taniuti*, 1964; *Boyd and Sanderson*, 1969; *Priest*, 1981; *Boyd and Sanderson*, 2003; *Parks*, 2004; *Gurnett and Bhattacharjee*, 2005]. Thus, given the upstream plasma and field parameters, as well as the shock normal, the downstream parameters can easily be calculated. The inverse calculation, i.e., determining the shock speed and orientation from measured upstream and downstream values, is generally a much more difficult problem, because the critical parameters that cannot be measured directly, such as the shock normal, depend in a very sensitive manner on the upstream and downstream plasma and field measurements. Near 1 AU, IP shocks can generally be assumed to be planar structures on the scale size of the Earth's magnetosphere. For example, *Russell et al.* [1983a] found the assumption of planarity consistent with measurements from four widely spaced solar wind monitors. Also using the assumption of shock planarity, *Russell et al.* [2000] estimated the shock normal orientation of a large IP shock with accuracy by comparing results of different IP shock normal determination methods.

The IP shock normal vector determines how the shock propagates through the heliosphere. Early studies showed that the shock normal of most IP shocks at 1 AU are aligned with the Sun-Earth line [*Bavassano et al.*, 1973; *Chao and Lepping*, 1974; *Heinemann and Siscoe*, 1974; *Siscoe*, 1976]. Normals of most IP shocks generated by CMEs at 1 AU are concentrated near the Sun-Earth line [*Richter et al.*, 1985]. Figure 1-6 represents schematically a shock formation in an ICME (a CME propagating in the heliosphere) front [*Zurbuchen and Richardson*, 2006]. However, shocks driven by corotating interaction regions (CIRs), as a result of the slow solar wind compression by a fast stream, have normals inclined in relation to the Sun-Earth line, as shown theoretically and in observations [see, e.g., *Hundhaunsen*, 1972a; *Siscoe*, 1976; *Pizzo*, 1978, 1991, and references therein]. Figure 1-7 shows how shocks are formed in CIR fronts. For CIR-driven shocks, the normal angles in the azimuthal direction in relation to the solar coordinate system are generally equal or larger than the inclination angle [*Siscoe*, 1976; *Pizzo*, 1991]. It is seen in Figure 1-7, extracted from *Russell* [2005], that the rotating geometry of CIRs may propitiate a good condition for shock inclinations in relation to the Sun-Earth line. The view is from above the north pole of the Sun, looking down on the ecliptic plane. Spatial differences in the nearly radial expansion (indicated by the dark vectors) couple with solar rotation to produce compression regions (shaded) and rarefactions in the interplanetary medium. Secondary nonradial motions are driven by pressure gradients built up in the stream interaction (large open arrows). Magnetic field lines, which correspond to streamlines of flow in the rotating frame, are drawn out into the spiral configuration as shown in Figure 1-7. Shocks may occur if

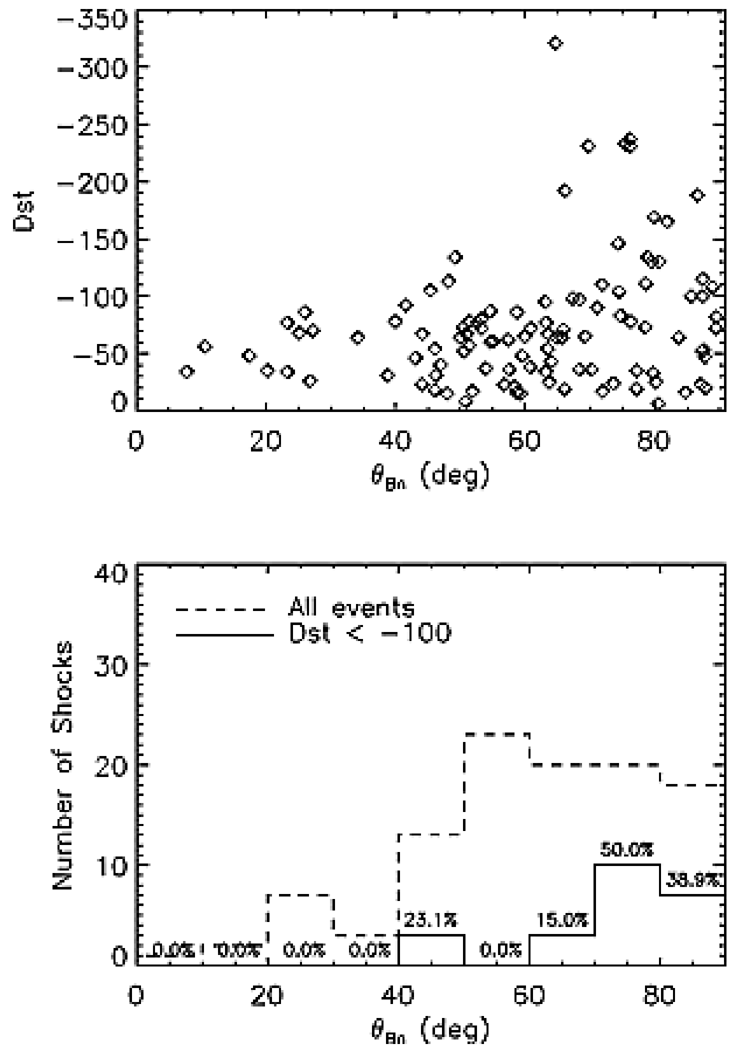

Figure 1-8: Upper panel: Dst strength plotted against θ_{B_n} , the angle between the upstream magnetic field vector and the shock normal. Almost perpendicular shocks (θ_{B_n} close to 90^o) showed to be more geoeffective. Lower panel: percentage of all shocks (dashed) and shocks associated with intense geomagnetic storms (Dst $<$ -100 nT, solid). In the latter case, most intense geomagnetic activities were associated with almost perpendicular shocks. Figure taken from *Jurac et al.* [2002].

the difference between the fast speed stream and slow speed stream is greater than the magnetosonic speed of the medium [*Russell*, 2005].

In the next section, we will review a few cases in the literature that studied the interaction of inclined IP shocks with the Earth's magnetosphere. In most cases, the shock normal was inclined in relation to the Sun-Earth line in the equatorial plane. The most studied effect was on the SSC rise time, not only in simulations, but also in satellite and geomagnetic data observations.

1.5 Previous works on shock normal inclinations

Several authors have studied the interaction of IP shocks with the Earth's magnetosphere in the context of numerical MHD simulations. However, almost always the IP shock hit the bow shock at the subsolar point head-on. For instance, *Ridley et al.* [2006] simulated an extreme IP shock driven by a Carrington-like CME [*Manchester et al.*, 2006] that pushed the magnetopause toward the Earth to the limit of their code boundary, which was at 2 R_E. They also observed a secondary shock wave reflected back by the magnetopause that encountered the bow shock that was moving inward. Then the combined motion propagated down the flanks of the magnetosphere. *Wang et al.* [2012] also studied the interaction of a very strong IP shock with the Earth's magnetosphere, where they observed the same Earth-ward movement of the bow shock as well. Similar bow shock Earth-ward motion was observed by *Šafránková et al.* [2007] in their numerical simulation for a much weaker IP shock as well. The interaction of IP shocks with the Earth's magnetosphere can also lead to generation of two ionospheric current systems [*Ridley et al.*, 2006; *Guo and Hu*, 2007; *Samsonov et al.*, 2010]. The appearance of an anomalous region I current, which flowed oppositely to the region I current, followed by a frontal IP shock impact with no IMF B_z was found by *Guo and Hu* [2007]. This anomalous region I current formed

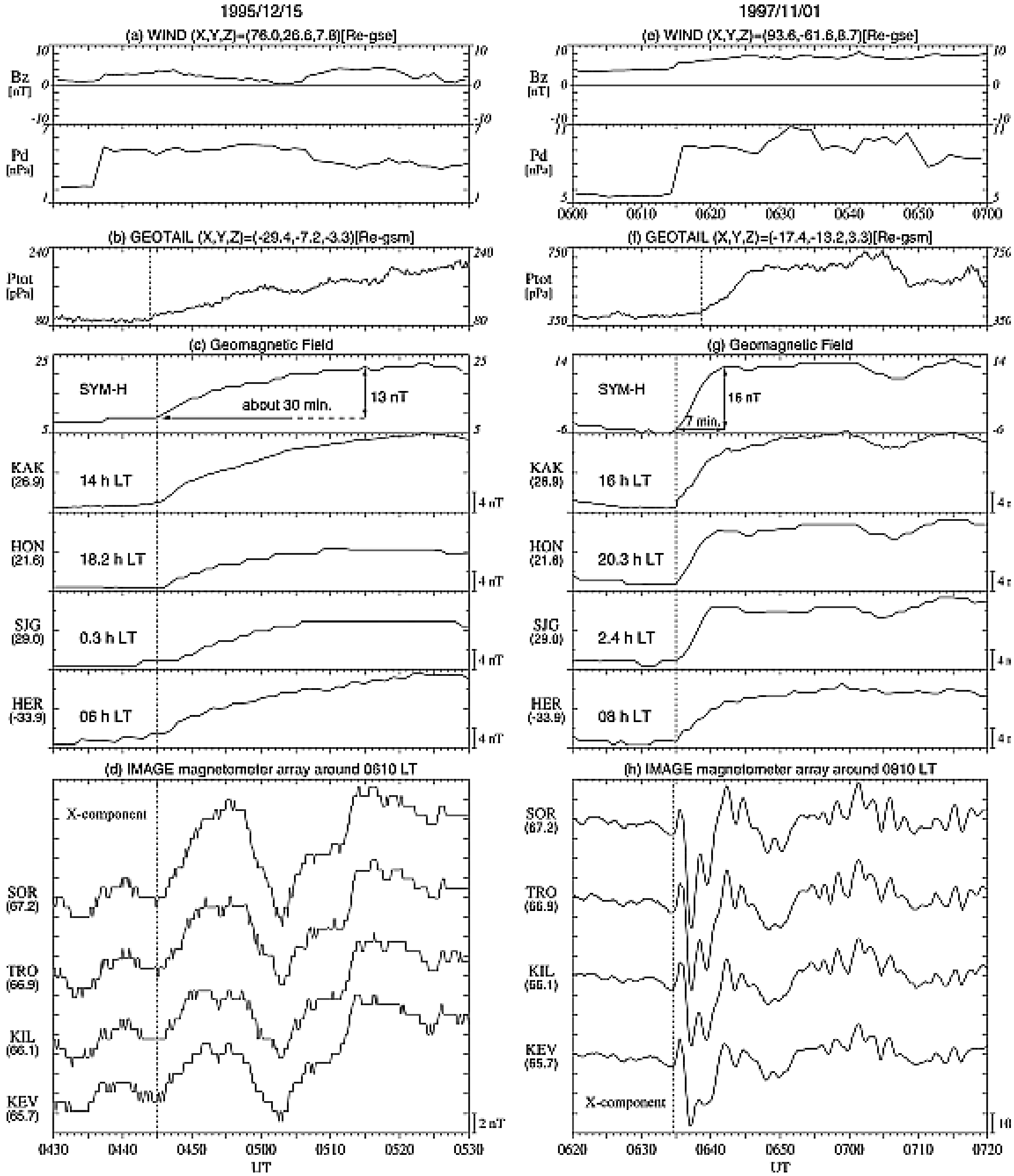

Figure 1-9: Comparison between two interplanetary shock-related events after *Takeuchi et al.* [2002]. The right column represents an event with a typical SSC rise time (∼7 minutes). The dynamic pressure increase is almost sharp (g). The left column shows a gradual increase in the dynamic pressure (b). Associated with this event, an unusually high SSC rise time of approximately 30 minutes was observed by ground stations. *Takeuchi et al.* [2002] suggested that such atypical effects resulted from a large angle of the shock normal vector and the Sun-Earth line in the equatorial plane.

at noon, developed and then moved toward the evening side until it vanished. Such a response depends on the strength of the IP shock. In other MHD simulations concerning the magnetosheath, three new discontinuities appeared downstream from the bow shock in addition to the impinging fast forward shock (FFS): a forward slow expansion wave, a contact discontinuity, and a reverse slow shock [*Koval et al.*, 2006; *Samsonov et al.*, 2006, 2007]. *Samsonov et al.* [2010] simulated the interaction of an IP shock with the magnetosphere in an artificial case with a northward IMF. The IP shock normal was aligned with the Sun-Earth line. They observed an intensification of two ionospheric current systems (similar to the preliminary and main impulse currents) that coincided in time with the intensification of two corresponding magnetospheric dynamos.

The interaction of IP shocks inclined in relation to the Sun-Earth line with the bow shock was also investigated by *Grib and Pushkar* [2006]. They solved the Rankine-Hugoniot (RH) conditions numerically for different shock inclinations and one of their most important results was that, for shock normal inclinations between 60^o and -60^o, the density changed from dusk to dawn in the bow shock in the case where the discontinuity was an FFS.

The geoeffectiveness of IP shocks was studied experimentally in the past by several authors. For example, *Jurac et al.* [2002] investigated 107 FFS shocks from 1995 to 2000 using WIND data. Their main focus was on θ_{B_n}, the angle between the upstream magnetic field vector and the shock normal. Figure 1-8 extracted from *Jurac et al.* [2002] shows the geoeffectiveness triggered by IP shocks in terms of θ_{B_n}. The upper panel shows the Dst (disturbance storm time) index plotted as a function of θ_{B_n}. According to their results, quasi-perpendicular shocks, i.e., shocks with θ_{B_n} close to 90^o, triggered more intense geomagnetic storms. The lower panel in Figure 1-8 indicates that most shocks had $\theta_{B_n} > 40^o$ (dashed line). Interestingly, cases with Dst $<$ -100 nT, or intense geomagnetic storms, following IP shocks (solid line) occur more frequently for $\theta_{B_n} > 70^o$. As a result, *Jurac et al.*

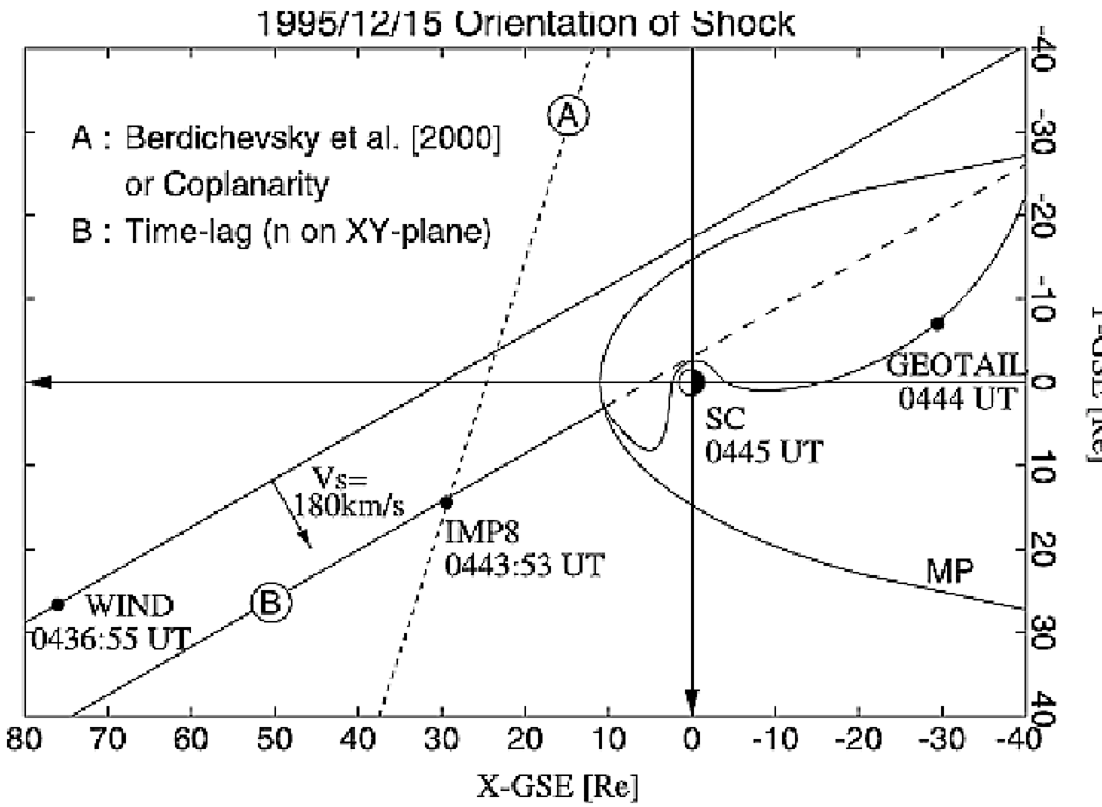

Figure 1-10: Shock frontal lines as calculated by *Berdichevsky et al.* [2000] (dashed) and *Takeuchi et al.* [2002] (solid) in the equatorial plane. The shock inclination in the equatorial plane was higher in the case of *Takeuchi et al.* [2002]. This high angle explained an unusually high SSC rise time observed by ground stations after an IP shock impact on 15 December 1995.

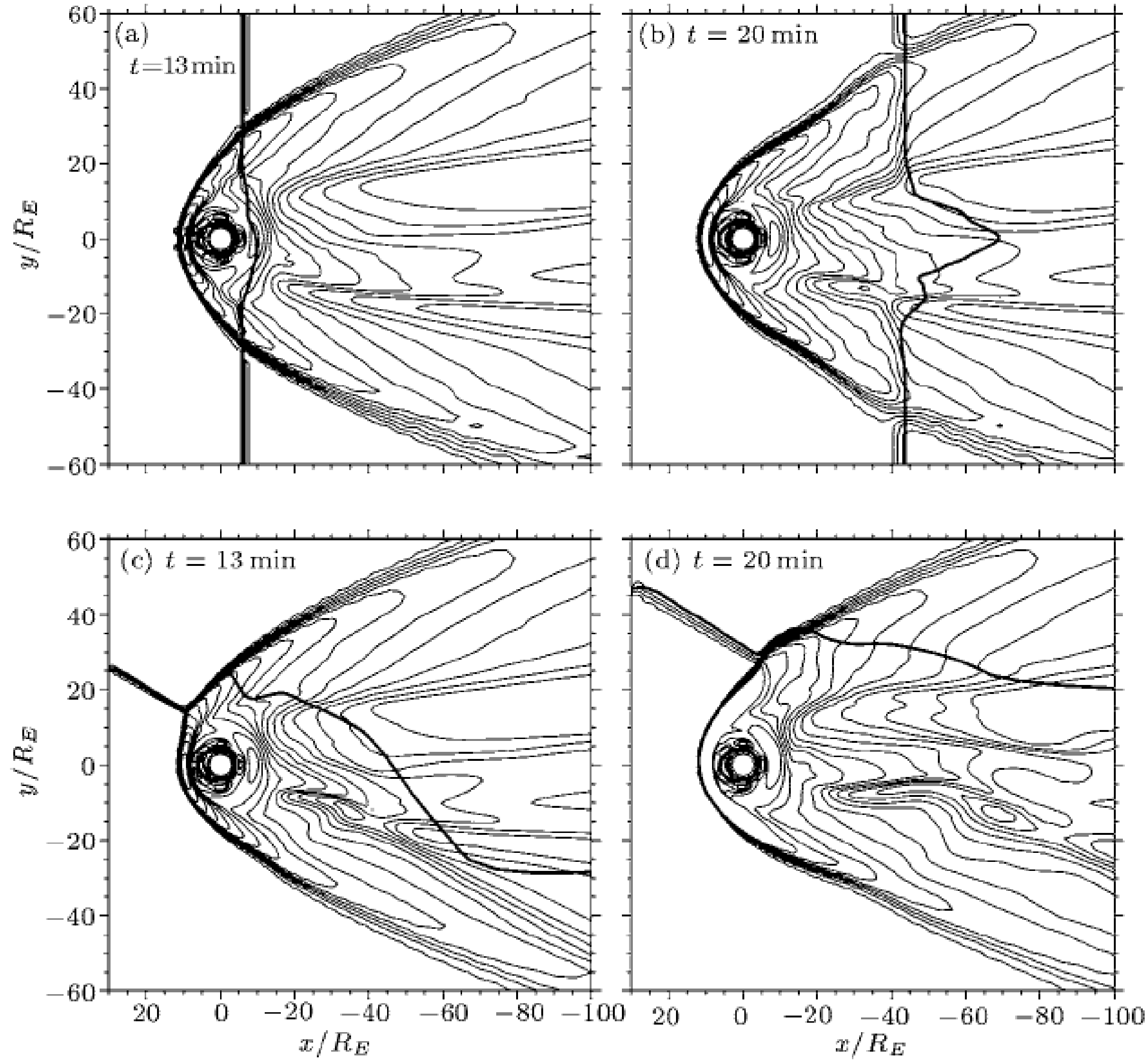

Figure 1-11: Contours of the thermal pressure resulted from global MHD simulations conducted by *Guo et al.* [2005] for two IP shocks with different shock normal inclinations. The frontal IP shock is represented by the two upper panels, and the inclined shock, by the two lower panels. Both shock normals lay in the equatorial plane. In the case of the inclined shock, the geoeffective magnetopause took longer to be compressed in comparison to the frontal shock.

[2002] concluded that almost perpendicular shocks are more geoeffective than quasi-parallel shocks.

The effects of IP shock inclinations on the SSC rise time were first pointed out by *Takeuchi et al.* [2002]. They observed an unusually long SSC rise time associated with an IP shock observed by WIND on 15 December 1995, shown in the left column of Figure 1-9 from *Takeuchi et al.* [2002], and another event on 01 November 1997 with a standard SSC rise time, shown in the right column of Figure 1-9. Figure 1-9 compares these two events. Typically, after an IP shock impact, the increase in total pressure (magnetic pressure plus thermal pressure) occurs sharply. In the standard case the total pressure increased from nearly 350 pPa to 550 pPa in approximately 8 minutes, as seen by GEOTAIL and represented in Figure 1-9(f). The jump of 16 nT in SYM-H, a version of the Dst index with 1-min time resolution, took only $\sim$7 minutes to occur, as represented by Figure 1-9(g). However, the dynamic pressure associated with the inclined shock event on 15 December 1995 in the inner magnetosphere as seen by GEOTAIL increased from 100 to 170 pPa in $\sim$30 minutes (Figure 1-9(b)). The SSC rise time of $\sim$30 minutes was associated with this gradual increase of the dynamic pressure. *Takeuchi et al.* [2002] suggested the existence of a "geoeffective magnetopause" to explain the gradual increase of the dynamic pressure in the inner magnetosphere. They argued that inclined IP shock waves would take more time to sweep by the geoeffective magnetopause. However, by inspecting the IP shock normal associated with the 15 December 1995 shock published previously by *Berdichevsky et al.* [2000], they noticed that the angle of the shock normal with the Sun-Earth line in the equatorial plane should be larger. Figure 1-10 shows the difference in the shock front inclinations in the same plane as predicted by *Berdichevsky et al.* [2000] and determined by *Takeuchi et al.* [2002]. Thus, *Takeuchi et al.* [2002] suggested that more investigations addressing the shock normal inclinations should be taken into account in studies of space

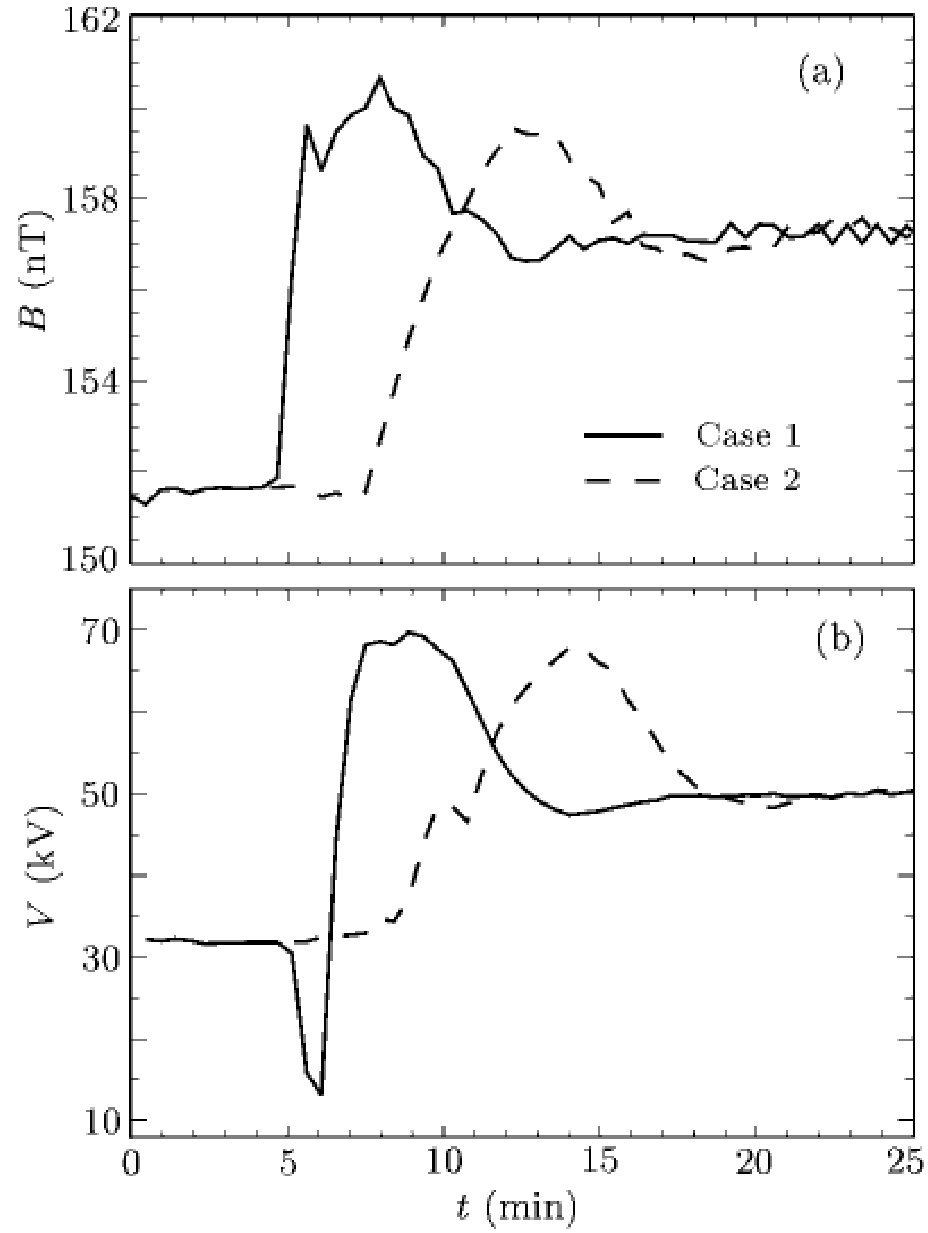

Figure 1-12: MI system evolution due to IP shock impacts simulated by *Guo et al.* [2005]. In both cases, a frontal shock (solid line) and an inclined shock (dashed line) reached about the same final quasi-steady state. However, the system impacted by the inclined shock took a longer time to reach its final state.

weather forecasting.

The observational result reported by *Takeuchi et al.* [2002] led the investigation of their effect of IP shock inclinations on SSC rise time through global MHD simulations. *Guo et al.* [2005] performed global numerical MHD simulations with different shock normal orientations to study the interaction of IP shocks with the Earth's magnetosphere. They simulated two cases in which IP shocks had different shock normal orientations with a Parker-spiral IMF orientation with no B_Z component. Both shocks had similar strength, as represented by their Mach numbers. In their first case, the shock normal was parallel to the Sun-Earth line, and in their second case the shock normal was inclined in relation to this line with an angle of 60^o. Results of both simulations are represented in Figure 1-11 taken from *Guo et al.* [2005]. The two upper panels indicate the thermal pressure contours during the interaction of the frontal shock with the Earth's magnetosphere. The two lower panels show the interaction of the inclined shock with the Earth's magnetosphere. They found that the impact of the inclined IP shock led to a longer evolution time of the system. Although both systems evolved from the same initial conditions in their numerical simulations, as can be seen in Figure 1-12, they did not find any significant difference in the final quasi-steady state of the systems. These results confirmed the observational effect reported by *Takeuchi et al.* [2002]. Similar results were also found by *Wang et al.* [2005]. More recently, similar results have been found by *Samsonov* [2011] as well. He presented a solution and analysis of the problem of an inclined IP shock incident on and propagating through the Earth's magnetosheath. He showed that inclined IP shocks with normals in the equatorial plane result in a dawn-dusk asymmetry in the magnetosheath and predicted that this effect should be present in observations of sudden impulse inside the magnetosphere and on the ground.

By using ACE and WIND satellite data, *Wang et al.* [2006] reported that, in a survey

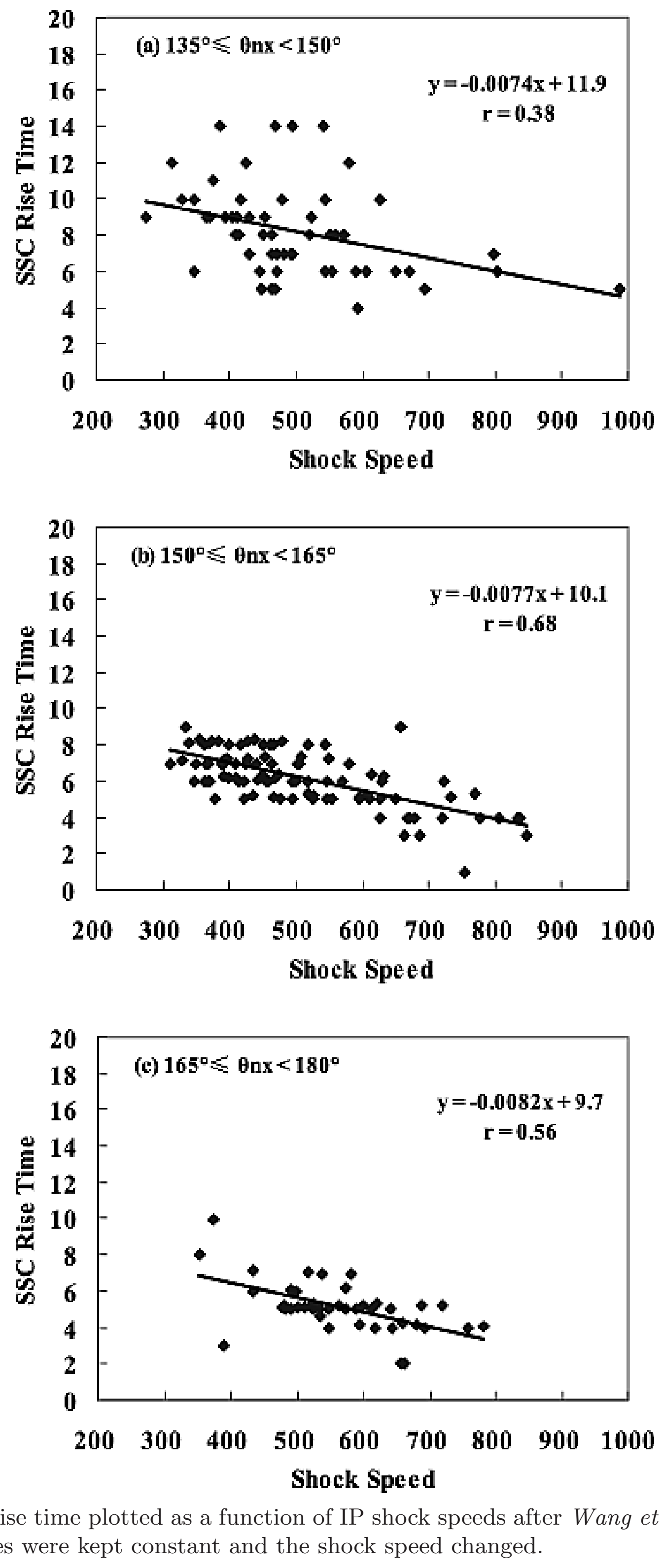

Figure 1-13: SSC rise time plotted as a function of IP shock speeds after *Wang et al.* [2006]. In this case, IP shock impact angles were kept constant and the shock speed changed.

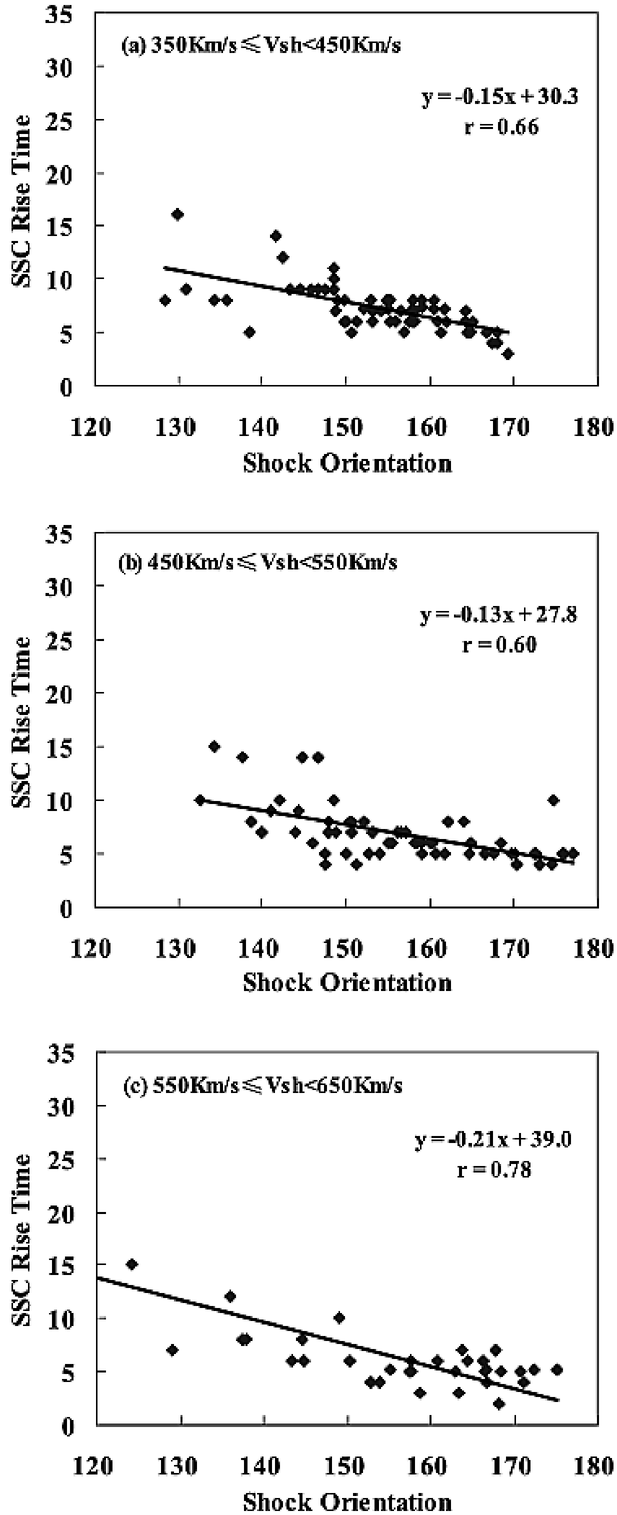

Figure 1-14: SSC rise time plotted as a function of IP shock impact angles after *Wang et al.* [2006]. In this case, IP shock speed intervals were kept constant and the IP shock angles changed.

of nearly 300 FFSs, 75% of them were followed by SSCs observed on the ground, confirming previous results [*Smith et al.*, 1986]. They found the average shock speed of nearly 500 km/s, and that most shocks had impact angles greater than 135^o (a shock with impact angle of 180^o is said to be a frontal shock). They also found that the shock impact angle plays an important role in determining the SSC rise time, as previously suggested by observation [*Takeuchi et al.*, 2002] and simulations [*Guo et al.*, 2005; *Wang et al.*, 2005]. They grouped their events according to the shock speed and impact angle. When the shock speed was fixed, the more parallel the shock normal with the Sun-Earth line, the smaller the SSC rise time. The same occurred when they fixed the shock inclination and changed the shock speed. The faster the shock, the shorter the SSC rise time. The highest correlation result found by *Wang et al.* [2006] occurred when the shock speed was fixed and the impact angle varied. Figures 1-13 and 1-14 summarize their results.

Here, we will show that the IP shock normal orientation is a critical parameter determining the geoeffectiveness of IP shocks. IP shocks that have their normal aligned with the Sun-Earth line have the largest geoeffectiveness, because they compress the magnetosphere from all sides at the same time. By contrast, if the shock normal makes a large angle with the Sun-Earth line in the x-z plane in GSE (Geocentric Solar Ecliptic) coordinate system, the north-south asymmetry of the impact pushes the plasma sheet either to the north or to the south without much compression, which leads to a much weaker response. This effect will be shown to occur in global MHD simulations.

1.6 A note on terminologies

The geometry of IP shocks is often discussed in the literature from a point of view of two different frame of references. Then, to avoid confusion, we will use terminologies connected to these two frame of references. The terminologies *oblique* and *perpendicular* refer to the angle between the upstream magnetic field and the shock normal, namely θ_{B_n} , *in a frame of reference moving with the shock*. On the other hand, the terminologies *inclined* and *frontal* are associated with the angle between the shock normal and the GSE Sun-Earth line, θ_{x_n} , as measured by an observer at Earth or a spacecraft.

1.7 Dissertation goals

The primary goal of this dissertation is to investigate the geoeffectiveness of IP shocks impacting the Earth's magnetosphere with different IP shock normal orientations. This analysis will be twofold. First, we use global MHD simulations to simulate impacts of IP shocks with different shock normal inclinations in relation to the Sun-Earth line meridian plane. Second, we use solar wind and IMF data to determine IP shock speed and impact angle. A description of MHD shocks and their geometries, not only in the shock frame of reference, but also in the spacecraft (or the Earth's) frame of reference, is discussed in Chapter 2. The OpenGGCM is briefly presented in Chapter 3. Chapter 4 discusses our simulation results. This chapter is a version of *Oliveira and Raeder* [2014].

Chapter 5 briefly discusses the geomagnetic data used in this dissertation. We validate our simulation results by using SuperMAG geomagnetic data. The SuperMAG collaboration, a chain of more than 300 ground magnetic stations, is there presented. The advantage in using the SuperMAG data instead of the traditional IAGA auroral electroject indices (AU, AL, AE) showed to be more effective, despite some caveats. The main difference between the SuperMAG and the IAGA indices is that the former are computed with a much larger number of ground stations.

Our observational results are presented in Chapter 6. That chapter is inspired in two papers, *Oliveira and Raeder* [2015] and *Oliveira et al.* [2015]. We then present the statistical results of an IP shock list compiled for this dissertation study. In the shock geoeffectiveness analysis, we found that substorms are stronger when the shock speed is fixed and the shock impact angle varies. Similar results were obtained for the nightside auroral power intensity integrated over the northern hemisphere polar cap.

Finally, we summarize our results and present a plan for future work in Chapter 7.

Chapter 2

Magnetohydrodynamic shocks

2.1 Introduction

The interplanetary medium is an electrically conducting fluid called plasma. When the moving plasma, or the solar wind, interacts with magnetic fields in its way, electric currents are induced, which in turn generate magnetic fields that change the plasma movement. The branch of science that describes the dynamics of the plasma motion is called magnetohydrodynamics, or simply MHD. The MHD theory corresponds to a coupled system of fluid equations and the Maxwell equations. Plasmas have an interesting property related to the formation of discontinuities. Discontinuities are non-linear effects resulting from wave steepening. When MHD discontinuities are driven in this environment, conservation of mass, momentum and energy are necessary to describe the plasma ahead and behind the discontinuity. These equations are called the Rankine-Hugoniot (RH) jump conditions. The type of discontinuity studied in this dissertation is a particular case of discontinuity called MHD shock. In this chapter, we derive the MHD equations and the RH equations commonly used to study shock behavior. We then classify MHD shocks in terms of their shock normal angles in relation to the upstream magnetic field vector in the shock reference frame and their motion relative to the Sun. Then we solve the RH equations for the particular cases of perpendicular and oblique shocks. Finally, we present some formulas used in this dissertation to calculate shock normal and speed both for the simulated and observed shocks described in this dissertation.

2.2 Magnetohydrodynamics

2.2.1 The Vlasov equation

A plasma is an electrically neutral fluid which contains electrically charged particles with positive and negative charges, which means that the overall electric charge in a plasma is zero. Each class of particles, such as protons, He^{2+}, O^{+}, and electrons are named species s. The statistical study involving the large amount of particles requires the use of a space defined in six dimensions called phase space. The phase space is defined in terms of the position $\mathbf{x} = (x, y, z)$ and velocity $\mathbf{v} = (v_x, v_y, v_z)$ vectors. These coordinates are independent of each other. The density of this large number of particles is then written in terms of a distribution function $f_s(\mathbf{x}, \mathbf{v}, t)$ for each species as shown below:

$$dn_s = f_s(\mathbf{x}, \mathbf{v}, t) d^3x d^3v \tag{2.1}$$

The above equation is useful to define macroscopic parameters in terms of different moments of the velocity $\mathbf{v}$. The moment of order zero in $\mathbf{v}$ is obtained by integrating equation (2.1) over the velocity space, and the result is the particle number density for each species in the system:

$$n_s = \int_{-\infty}^{+\infty} f_s(\mathbf{x}, \mathbf{v}, t) d^3v \tag{2.2}$$

The first order moment is obtained by integrating (2.1) again with the first power of $\mathbf{v}$. This is the average velocity distribution for each species in the system (the integral limits are dropped but the integral is still calculated over the velocity space):

$$\mathbf{u}_s = \frac{1}{n_s} \int \mathbf{v} f_s d^3 v \tag{2.3}$$

The second moment of the distribution function is the pressure tensor (m_s is the mass of each species s):

$$\bar{P} = m_s \int (\mathbf{v} - \mathbf{u}_s)(\mathbf{v} - \mathbf{u}_s) f_s d^3 v \tag{2.4}$$

Equations (2.2-4) define macroscopic parameters. Macroscopic MHD equations are derived from the distribution function f_s. Taking the time derivative of the distribution function, where $i = 1, 2, 3$ below, one gets

$$\begin{aligned} \frac{df_s}{dt} &= \frac{\partial f_s}{\partial t} + \sum_{i=1}^{3} \frac{\partial f_s}{\partial x_i} \frac{\partial x_i}{\partial t} + \sum_{i=1}^{3} \frac{\partial f_s}{\partial v_i} \frac{\partial v_i}{\partial t} \\ &= \frac{\partial f_s}{\partial t} + \mathbf{v} \cdot \boldsymbol{\nabla} f_s + \mathbf{a} \cdot \boldsymbol{\nabla}_v f_s \end{aligned}$$

The mean free path of particles in the interplanetary plasma are of the order of nearly 1 AU, or approximately 150 million kilometers. Collisions in the interplanetary plasma occur approximately once every 10^8 seconds. Thus, collisions may be neglected, and this plasma is assumed to be collisionless. If the interplanetary plasma is collisionless, the time derivative of the distribution function vanishes, and the number of particles inside the boundary is conserved [*Baumjohann and Treumann*, 2009]. As a result, the above equation, known as the Vlasov equation, can be written as

$$\frac{\partial f_s}{\partial t} + \mathbf{v} \cdot \boldsymbol{\nabla} f_s + \mathbf{a} \cdot \boldsymbol{\nabla}_v f_s = 0\,, \tag{2.5}$$

where the operators $\boldsymbol{\nabla}$ and $\boldsymbol{\nabla}_v$ act on the position and velocity coordinates, respectively.

The forces acting on the interplanetary plasma are strictly electromagnetic forces. The electric charge of each species s is represented by q_s. Gravitational and rotational forces may be neglected [*Priest*, 1981]. From Newton's second law and the Lorentz force

$$m_s \mathbf{a} = q_s(\mathbf{E} + \mathbf{v} \times \mathbf{B}) \,, \tag{2.6}$$

the Vlasov equation is given by

$$\frac{\partial f_s}{\partial t} + \mathbf{v} \cdot \boldsymbol{\nabla} f_s + \frac{q_s}{m_s}(\mathbf{E} + \mathbf{v} \times \mathbf{B}) \cdot \boldsymbol{\nabla}_v f_s = 0 \tag{2.7}$$

The electric and magnetic fields are obtained from the Maxwell equations. The Vlasov equation as represented above shall be used to determine the one-fluid theory macroscopic equations from which the RH jump conditions will be obtained.

2.2.2 The Maxwell equations in the MHD context

A plasma is composed of positive and negative particles. Therefore, the plasma motion depends on the electric and magnetic fields $\mathbf{E}$ and $\mathbf{B}$ and is governed by Maxwell's equations as described below [*Jackson*, 1999]:

$$\boldsymbol{\nabla} \cdot \mathbf{E} = \frac{\rho_q}{\varepsilon_0} \tag{2.8}$$

$$\boldsymbol{\nabla} \cdot \mathbf{B} = 0 \tag{2.9}$$

$$\boldsymbol{\nabla} \times \mathbf{E} = -\frac{\partial \mathbf{B}}{\partial t} \tag{2.10}$$

$$\boldsymbol{\nabla} \times \mathbf{B} = \mu_0 \mathbf{J} + \mu_0 \varepsilon_0 \frac{\partial \mathbf{E}}{\partial t} \tag{2.11}$$

These equations need some adjustments to be included in the MHD theory. The charge density ρ_q in the interplanetary plasma is null due to the plasma quasi-neutrality condition. The speed of light is defined as $c = 1/\sqrt{\mu_0\varepsilon_0}$. Considering the MHD characteristic dimensions for length, time, and speed as L, τ, and U (non-relativistic speed), the spatial and time derivative of $\mathbf{B}$ and $\mathbf{E}$ can be written as approximately $|\boldsymbol{\nabla} \times \mathbf{B}| \approx B/L$ and $\mu_0\varepsilon_0|\partial\mathbf{E}/\partial t| \approx E/(c^2\tau)$. From the dimensional analysis of Faraday's equation (2.10), one gets $E = UB$. Thus, comparing the above derivatives,

$$\frac{\mu_0\varepsilon_0\partial\mathbf{E}/\partial t}{|\boldsymbol{\nabla} \times \mathbf{B}|} \approx \frac{E/(c^2\tau)}{B/L} = \frac{U^2}{c^2} \ll 1 \tag{2.12}$$

Therefore, the Maxwell equations in the MHD context are reduced to

$$\boldsymbol{\nabla} \cdot \mathbf{E} = 0 \tag{2.13}$$

$$\boldsymbol{\nabla} \cdot \mathbf{B} = 0 \tag{2.14}$$

$$\boldsymbol{\nabla} \times \mathbf{E} = -\frac{\partial\mathbf{B}}{\partial t} \tag{2.15}$$

$$\boldsymbol{\nabla} \times \mathbf{B} = \mu_0\mathbf{J} \tag{2.16}$$

2.2.3 The adiabatic state equation

In thermodynamics, a gas can expand rapidly enough without exchanging heat with the external medium. Such process is called an adiabatic process, in which the heat flux flowing out of the system may be neglected. From the first law of thermodynamics, which is the energy conservation law for thermodynamic fluids, it is possible to show that the adiabatic fluid obeys the relation PV^γ = constant, where γ is the ratio of the heat capacity with constant pressure to the heat capacity with constant volume. This equation can be written in a conservative form as

$$\frac{d}{dt}\left(\frac{P}{\rho^\gamma}\right) = 0\,. \tag{2.17}$$

The adiabatic state equation will be useful later in deriving MHD macroscopic equations in conservative forms.

2.2.4 Multi-fluid MHD theory: macroscopic equations

The problem analysis in plasma physics goes beyond the definition of the distribution function f_s. Often it is necessary to write equations in terms of average macroscopic quantities calculated from the distribution function because we are more interested in macroscopic averages such as density and velocity averages instead of details of the distribution function itself. Such average macroscopic quantities are described by the moment equations. The moment equations are calculated from the Vlasov equation by multiplying equation (2.7) by powers of the velocity $\mathbf{v}$ and integrating the moment equations over the velocity space.

The zeroth macroscopic equation or zeroth moment equation is obtained from the Vlasov equation by multiplying equation (2.7) by v^0 and integrating it in the velocity space V:

$$\int_V \frac{\partial f_s}{\partial t} d^3v + \int_V \mathbf{v} \cdot \boldsymbol{\nabla} f_s d^3v + \frac{q_s}{m_s} \int_V (\mathbf{E} + \mathbf{v} \times \mathbf{B}) \cdot \boldsymbol{\nabla}_v f_s d^3v = 0 \tag{2.18}$$

The time derivative can be pulled out of the integral since the velocity coordinate does not depend on time. Then, the first term yields

$$\frac{\partial}{\partial t} \int_V f_s d^3v = \frac{\partial n_s}{\partial t} \tag{2.19}$$

Since the operator $\boldsymbol{\nabla}$ does not affect the integration over the velocity space, the second term can be rearranged as

$$\int_V \mathbf{v} \cdot \boldsymbol{\nabla} f_s d^3v = \boldsymbol{\nabla} \cdot \int_V \mathbf{v} f_s d^3v = \boldsymbol{\nabla} \cdot (n_s \mathbf{u}_s) \tag{2.20}$$

In the following vectorial identity

$$\boldsymbol{\nabla}\cdot(\varphi\mathbf{A}) = \mathbf{A}\cdot\boldsymbol{\nabla}\varphi + \varphi\boldsymbol{\nabla}\cdot\mathbf{A}\,, \tag{2.21}$$

φ is a scalar function and $\mathbf{A}$ is a vectorial function. Using (2.21), the third term of equation (2.18) is now rewritten as

$$\frac{q_s}{m_s}\int_V(\mathbf{E}+\mathbf{v}\times\mathbf{B})\cdot\boldsymbol{\nabla}_v f_s d^3v = \frac{q_s}{m_s}\int_V\boldsymbol{\nabla}_v\cdot[f_s(\mathbf{E}+\mathbf{v}\times\mathbf{B})]d^3v - \frac{q_s}{m_s}\int_V f_s\boldsymbol{\nabla}_v\cdot(\mathbf{E}+\mathbf{v}\times\mathbf{B})d^3v$$

$$= \frac{q_s}{m_s}\oint_S[f_s(\mathbf{E}+\mathbf{v}\times\mathbf{B})]\cdot d\mathbf{S} - \frac{q_s}{m_s}\int_V f_s\boldsymbol{\nabla}_v\cdot\mathbf{E}d^3v - \frac{q_s}{m_s}\int_V f_s\boldsymbol{\nabla}_v\cdot(\mathbf{v}\times\mathbf{B})d^3v$$

$$= 0$$

where the Gauss theorem was used above. The distribution function vanishes at the boundary S when $v \to \infty$. Due to the fact that the electric field does not depend on the velocity v, $\boldsymbol{\nabla}_v\cdot\mathbf{E} = 0$. The identity $\boldsymbol{\nabla}_v\cdot(\mathbf{v}\times\mathbf{B}) = 0$ was used above as well.

Therefore, with these results, equation (2.18) gives

$$\frac{\partial n_s}{\partial t} + \boldsymbol{\nabla}\cdot(n_s\mathbf{u}_s) = 0$$

By multiplying the above equation by m_s, one obtains the mass density $\rho_{ms} = n_s m_s$, and the first macroscopic equation or the mass conservation equation for each species s is represented by:

$$\frac{\partial\rho_{ms}}{\partial t} + \boldsymbol{\nabla}\cdot(\rho_{ms}\mathbf{u}_s) = 0 \tag{2.22}$$

The first moment equation is obtained by multiplying the Vlasov equation (2.7) by the first power in velocity $\mathbf{v}$ and integrating it over the velocity space:

$$\int_V \mathbf{v}\frac{\partial f_s}{\partial t}d^3v + \int_V \mathbf{v}(\mathbf{v}\cdot\boldsymbol{\nabla} f_s)d^3v + \frac{q_s}{m_s}\int_V \mathbf{v}[(\mathbf{E}+\mathbf{v}\times\mathbf{B})]\cdot\boldsymbol{\nabla}_v f_s d^3v = 0 \tag{2.23}$$

The time derivative operator can be taken out of the integral since the velocity space does not depend on time. Thus, using equation (2.3), the first term in equation (2.23) gives:

$$\int_V \mathbf{v}\frac{\partial f_s}{\partial t}d^3v = \frac{\partial}{\partial t}\int_V \mathbf{v} f_s d^3v = \frac{\partial}{\partial t}(n_s\mathbf{u}_s) \tag{2.24}$$

The operator $\boldsymbol{\nabla}$ does not act on the velocity coordinates and can be written out of the integral in the second term of equation (2.23). Then using equations (2.3) after rewriting the term $\mathbf{vv}$, we get

$$\begin{aligned}
\int_V \mathbf{v}(\mathbf{v}\cdot\boldsymbol{\nabla} f_s)d^3v &= \boldsymbol{\nabla}\cdot\int_V \mathbf{vv} f_s d^3v \\
&= \boldsymbol{\nabla}\cdot\int_V (\mathbf{v}-\mathbf{u}_s)(\mathbf{v}-\mathbf{u}_s)f_s d^3v + \boldsymbol{\nabla}\cdot\int_V [\mathbf{u}_s\mathbf{v}+\mathbf{v}\mathbf{u}_s-\mathbf{u}_s\mathbf{u}_s]f_s d^3v \\
&= \boldsymbol{\nabla}\cdot\left[\int_V (\mathbf{v}-\mathbf{u}_s)(\mathbf{v}-\mathbf{u}_s)f_s\right]d^3v + \boldsymbol{\nabla}\cdot(n_s\mathbf{u}_s\mathbf{u}_s)
\end{aligned} \tag{2.25}$$

Using equation (2.4), the second integral in equation (2.23) is

$$\int_V \mathbf{v}(\mathbf{v}\cdot\boldsymbol{\nabla} f_s)d^3v = \frac{1}{m_s}\boldsymbol{\nabla}\cdot\bar{P}_s + \boldsymbol{\nabla}\cdot(n_s\mathbf{u}_s\mathbf{u}_s) \tag{2.26}$$

The third term of equation (2.23) is rearranged using the identity (2.21):

$$\frac{q_s}{m_s}\int_V \mathbf{v}(\mathbf{E}+\mathbf{v}\times\mathbf{B})\cdot\boldsymbol{\nabla}_v f_s d^3v = \frac{q_s}{m_s}\int_V \boldsymbol{\nabla}_v\cdot[\mathbf{v}(\mathbf{E}+\mathbf{v}\times\mathbf{B})]d^3v - \frac{q_s}{m_s}\int_V f_s\boldsymbol{\nabla}_v\cdot[\mathbf{v}(\mathbf{E}+\mathbf{v}\times\mathbf{B})]d^3v$$

$$= \frac{q_s}{m_s}\oint_S [\mathbf{v}(\mathbf{E}+\mathbf{v}\times\mathbf{B})]\cdot d\mathbf{S} - \frac{q_s}{m_s}\int_V f_s(\mathbf{E}+\mathbf{v}\times\mathbf{B})d^3v$$

$$= -\frac{n_s q_s}{m_s}(\mathbf{E}+\mathbf{u}_s\times\mathbf{B})$$

In the calculation above, after using Gauss's theorem, the distribution function f_s vanishes at the boundary when the velocity goes to infinity. Then, by collecting all results, where $\rho_{qs} = n_s e_s$ is the charge density for the species s, equation (2.23) gives:

$$\frac{\partial}{\partial t}(n_s\mathbf{u}_s) + \frac{1}{m_s}\boldsymbol{\nabla}\cdot\bar{P}_s + \boldsymbol{\nabla}\cdot(n_s\mathbf{u}_s\mathbf{u}_s) - \frac{\rho_{qs}}{m_s}[\mathbf{E}+\mathbf{u}_s\times\mathbf{B}] = 0 \tag{2.27}$$

Therefore, by multiplying the above equation by m_s with some simplifications, one gets the first moment equation or the MHD momentum equation:

$$\rho_{ms}\left[\frac{\partial\mathbf{u}_s}{\partial t} + (\mathbf{u}_s\cdot\boldsymbol{\nabla})\mathbf{u}_s\right] + \boldsymbol{\nabla}\cdot\bar{P}_s - \rho_{qs}[\mathbf{E}+\mathbf{u}_s\times\mathbf{B}] = 0 \tag{2.28}$$

where ρ_{ms} and ρ_{qs} represent the mass and charge densities, respectively. The operator $\partial/\partial t + \mathbf{u}\cdot\boldsymbol{\nabla}$ is named the convective derivative.

2.2.5 One fluid MHD theory

In the last section we presented the macroscopic equations for different plasma species s. The interplanetary plasma is formed by electrons with negative charge $q_e = -e$ and ions with positive charge $q_i = +Ze$. Most ions, or about 95%, correspond to protons ($Z = 1$), and the others are alpha particles and heavier ions. The total thermal pressure is the sum of the electron and ion contributions. As a result, the thermal pressure, the charge density and the current density in a plasma are given by:

$$P = P_e + P_i \,, \tag{2.29}$$

$$\rho_q = e(n_i - n_e) \,, \tag{2.30}$$

$$\mathbf{J} = e(n_i \mathbf{u}_i - n_e \mathbf{u}_e) \tag{2.31}$$

In order to write these equation in terms of only one fluid we use the fact that the mass of the ions are much larger than the mass of electrons, or $m_i \gg m_e$. This implies that the inertial terms in equations (2.22) and (2.28) are dominated by ions. With this assumption and equations (2.29-31), the mass equation and the momentum equation are given by:

$$\frac{\partial \rho_m}{\partial t} + \boldsymbol{\nabla} \cdot (\rho_m \mathbf{u}) = 0 \tag{2.32}$$

$$\rho_m \left[\frac{\partial \mathbf{u}}{\partial t} + (\mathbf{u} \cdot \boldsymbol{\nabla})\mathbf{v} \right] + \boldsymbol{\nabla} P - \rho_q \mathbf{E} - \mathbf{J} \times \mathbf{B} = 0 \tag{2.33}$$

The term dependent on $\mathbf{J}$ in the momentum equation can be substituted by the Ampère law (2.16) to give $\mathbf{J} \times \mathbf{B} = (\boldsymbol{\nabla} \times \mathbf{B}) \times \mathbf{B}/\mu_0$. Due to the fact that plasmas are almost electrically neutral, the electric charge density ρ_q can be neglected. Since the only density term appearing in the mass and momentum equation is the mass density, we can drop the mass index in the mass density terms. Thus, the momentum equation can be written as

$$\frac{\partial}{\partial t}(\rho \mathbf{u}) + \boldsymbol{\nabla} \cdot (\rho \mathbf{u}\mathbf{u}) + \boldsymbol{\nabla} P - \frac{1}{\mu_0}(\boldsymbol{\nabla} \times \mathbf{B}) \times \mathbf{B} = 0 \tag{2.34}$$

We now seek one more equation to complete our set of MHD conservative equations.

This equation is the second moment equation or the energy equation. This task can be accomplished by multiplying equation (2.34) by $\mathbf{u}$:

$$\rho\mathbf{u}\cdot\left[\frac{\partial\mathbf{u}}{\partial t}+(\mathbf{u}\cdot\boldsymbol{\nabla})\mathbf{u}\right]+(\mathbf{u}\cdot\boldsymbol{\nabla})P-\frac{\mathbf{u}}{\mu_0}\cdot[(\boldsymbol{\nabla}\times\mathbf{B})\times\mathbf{B}]=0 \tag{2.35}$$

The first term in equation (2.35) obeys the following identity:

$$\rho\mathbf{u}\cdot\left[\frac{\partial\mathbf{u}}{\partial t}+(\mathbf{u}\cdot\boldsymbol{\nabla})\mathbf{u}\right]=\frac{\partial}{\partial t}\left(\frac{1}{2}\rho u^2\right)+\boldsymbol{\nabla}\cdot\left(\frac{1}{2}\rho u^2\mathbf{u}\right) \tag{2.36}$$

Now let us use the adiabatic state equation (2.17). Using the convective derivative, expanding the time derivative on the right-hand side, and using the mass conservation equation (2.32), one gets

$$\begin{aligned}\frac{\partial P}{\partial t}+(\mathbf{u}\cdot\boldsymbol{\nabla})P &= \frac{\gamma P}{\rho}\left[\frac{\partial\rho}{\partial t}+(\mathbf{u}\cdot\boldsymbol{\nabla})\rho\right]\\ &= -\gamma P\boldsymbol{\nabla}\cdot\mathbf{u}\end{aligned} \tag{2.37}$$

Using the identity $P(\boldsymbol{\nabla}\cdot\mathbf{u})=\boldsymbol{\nabla}\cdot(P\mathbf{u})-\mathbf{u}\cdot\boldsymbol{\nabla}P$ and solving for the second term in equation (2.37), we get

$$(\mathbf{u}\cdot\boldsymbol{\nabla})P=\frac{1}{\gamma-1}\frac{\partial P}{\partial t}+\frac{\gamma}{\gamma-1}\boldsymbol{\nabla}\cdot(P\mathbf{u}) \tag{2.38}$$

The last term in equation (2.35) is given by

$$\mathbf{u}\cdot(\boldsymbol{\nabla}\times\mathbf{B})\times\mathbf{B}=-\frac{\partial}{\partial t}\left(\frac{1}{2}B^2\right)-\boldsymbol{\nabla}\cdot(\mathbf{E}\times\mathbf{B}) \tag{2.39}$$

Finally, after collecting all terms, the macroscopic MHD energy equation can be written as

$$\frac{\partial}{\partial t}\left(\frac{1}{2}\rho u^2 + \frac{P}{\gamma - 1} + \frac{B^2}{2\mu_0}\right) + \boldsymbol{\nabla}\cdot\left[\frac{1}{2}\rho u^2\mathbf{u} + \frac{\gamma P}{\gamma - 1}\mathbf{u} + \frac{1}{\mu_0}(\mathbf{E}\times\mathbf{B})\right] = 0 \qquad (2.40)$$

In these equations, ρ is the plasma density, $\mathbf{B}$ is the magnetic field, $\mathbf{u}$ the plasma bulk speed, $P/(\gamma - 1)$ is the internal energy and $\gamma P/(\gamma - 1)$ is the enthalpy of the system. In summary, the conserved quantities are described as follows. Equation (2.32) indicates conservation of mass in the plasma. The other two equations indicate conservation of both momentum (2.33) and energy (2.40), respectively.

As described by *Priest* [1981], a plasma can be studied in terms of its typical speeds, magnetic field, and some dimensionless parameters. In summary, such speeds are the sound speed

$$c_S = \left(\frac{\gamma P}{\rho}\right)^{1/2}, \qquad (2.41)$$

the Alfvén speed:

$$v_A = \frac{B}{\sqrt{\mu_0 \rho}}, \qquad (2.42)$$

and the magnetosonic speed:

$$v_{MS} = \sqrt{\frac{1}{2}(v_A^2 + c_S^2) \pm \sqrt{(v_A^2 + c_S^2)^2 - 4c_S^2 v_A^2 \cos^2\theta_{B_n}}}\,. \qquad (2.43)$$

whose positive root indicates the fast magnetosonic speed, and the negative root indicates the slow magnetosonic speed. The obliquity θ_{B_n} is the angle between the upstream magnetic field and the discontinuity normal vector.

The dimensionless plasma parameters are represented by the plasma beta, which is the ratio between the plasma thermal pressure and the magnetic pressure:

$$\beta = \frac{2\mu_0 P}{B^2}, \qquad (2.44)$$

and other parameters called Mach numbers, the ratio of the fluid speed u to the characteristic medium speed. Such Mach numbers are the sonic Mach number:

$$M_S = \frac{u}{c_S}\,, \tag{2.45}$$

the Alfénic Mach number

$$M_A = \frac{u}{v_A}\,, \tag{2.46}$$

and, in the same sense, the magnetosonic Mach number is written as

$$M_{MS} = \frac{u}{v_{MS}}\,. \tag{2.47}$$

In the particular case of MHD shocks, the speed considered is the speed of the shock in relation to the medium.

2.3 Magnetohydrodynamic discontinuities

2.3.1 The Rankine-Hugoniot jump conditions for MHD discontinuities

A shock is formed in a medium when a wave suffers a discontinuity in which its main parameters change, such as the fluid density, temperature (pressure), and velocity [*Burguess*, 1995; *Burlaga*, 1995; *Russell*, 2005]. A necessary condition is that the relative speed between the shock and the fluid flow has to be greater than the sound speed in the non-shocked side of the discontinuity. Also, with the increase of pressure and temperature, one can affirm that the entropy increases beyond the shock, which indicates that the kinetic energy of the wave gives rise to the increase in thermal energy of the shocked fluid. Such descriptions are valid for a regular fluid, where particles change energy and momentum due to collisions. In the case of the solar wind, average densities are typically 5 particles per cm^3 at 1 AU.

With mean-free-path of the order of the dimensions of the medium, which is approximately 1 AU, calculated from kinetic theory, collisions in the plasma are unlikely to occur [*Sagdeev and Kennel*, 1991]. Instead, momentum and energy are transmitted amongst particles due to the presence of the magnetic field, which makes the process more complicated. Now, not only the magnetic field magnitude matters, but also its direction in relation to the shock normal is important [*Burlaga*, 1995]. The presence of the magnetic field also adds two other complications: First, the plasma does not have only a typical speed such as the sound speed, since the concepts of Alfvén speed and the fast magnetosonic speed are necessary to explain the wave behavior of the plasma. Second, the shock geometry plays an important role in the shock physics since the magnetic field vector orientation in relation to the shock normal has different consequences when this angle is large or small. This last feature will be discussed further. As a result, a shock only exists when the relative speed between it and the medium is larger than at least the slow magnetosonic speed, or according to expression (2.46), when $M_S \geq 1$ [*Burlaga*, 1995].

The Rankine-Hugoniot (RH) jump conditions are derived from the MHD macroscopic equations written in conservative forms. These equations are (2.32), the mass conservation equation, (2.33), the momentum equation, and (2.40), the energy equation, written slightly different after some minor manipulations:

$$\frac{\partial}{\partial t}(\rho \mathbf{u}) + \boldsymbol{\nabla} \cdot (\rho \mathbf{u}) = 0 \tag{2.48}$$

$$\frac{\partial}{\partial t}(\rho \mathbf{u}) + \boldsymbol{\nabla} \cdot \left[\rho \mathbf{u}\mathbf{u} + \left(P + \frac{B^2}{2\mu_0}\right)\mathbf{1} - \frac{\mathbf{B}\mathbf{B}}{\mu_0}\right] = 0 \tag{2.49}$$

$$\frac{\partial}{\partial t}\left(\frac{1}{2}\rho u^2 + \frac{P}{\gamma - 1} + \frac{B^2}{2\mu_0}\right) + \boldsymbol{\nabla} \cdot \left[\frac{1}{2}\rho u^2 \mathbf{u} + \frac{\gamma P}{\gamma - 1}\mathbf{u} + \frac{1}{\mu_0}(\mathbf{E} \times \mathbf{B})\right] = 0 \tag{2.50}$$

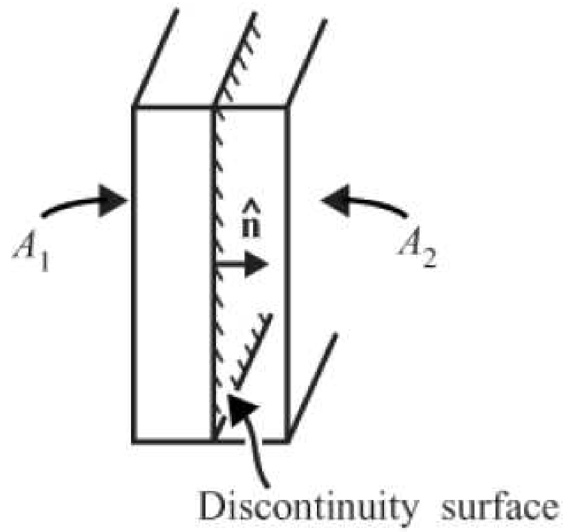

Figure 2-1: Schematic representation of a tiny box across the surface of an MHD discontinuity. Assuming the box thickness to be infinitely small, its volume shrinks to zero. Figure from *Gurnett and Bhattacharjee* [2005]

In order to relate plasma parameters in upstream (unshocked plasma) and downstream (shocked plasma) regions, let us consider a straightforward method as described by *Gurnett and Bhattacharjee* [2005]. Figure 2-1 represents a plasma flowing through a very thin surface across an MHD discontinuity of areas A_1 (unshocked side) and A_2 (shocked side) along, say, the normal $\mathbf{n}$, which is perpendicular to both surfaces. Integrating equation (2.48) and applying the Gauss theorem to its second term, we get:

$$\int_{V_1} \frac{\partial \rho_1}{\partial t} d^3x + \int_{V_2} \frac{\partial \rho_2}{\partial t} d^3x + \int_{V_2} \boldsymbol{\nabla} \cdot (\rho \mathbf{u})_1 d^3x + \int_{V_1} \boldsymbol{\nabla} \cdot (\rho \mathbf{u})_2 d^3x = 0 \qquad (2.51)$$

$$\int_{A_1} (\rho \mathbf{u})_1 \cdot d\mathbf{A}_1 + \int_{A_2} (\rho \mathbf{u})_2 \cdot d\mathbf{A}_2 = 0 \qquad (2.52)$$

Due to the very small box thickness, we can consider both volumes V_1 and V_2 shrinking to zero. This argument implies that the first two terms in equation (2.51) vanish. Assuming both surfaces are parallel to each other, $A_1 = A_2$. The scalar product in the two remaining parts of equation (2.52) are negative for A_1 and positive for A_2 due to the normal vector direction. We also define two unitary vectors, $\hat{\mathbf{n}}$, normal to the shock surface, and $\hat{\mathbf{t}}$, tangential to the normal surface. Therefore, equation (2.52) can be written in a conservative form as

$$\rho_1(\mathbf{u}_1 \cdot \mathbf{n}) = \rho_2(\mathbf{u}_2 \cdot \mathbf{n}) \tag{2.53}$$

Applying the same method to the other equations, the RH jump conditions for conservation of mass, momentum, and energy are written as:

$$[\rho u_n] = 0 \tag{2.54}$$

$$\left[\rho u_n \mathbf{u} + \left(P + \frac{B^2}{2\mu_0}\right)\hat{\mathbf{n}} - \frac{B_n \mathbf{B}}{\mu_0}\right] = 0 \tag{2.55}$$

$$\left[\left(\frac{1}{2}\rho u^2 + \frac{\gamma P}{\gamma - 1}\right)u_n + \frac{1}{\mu_0}(\mathbf{E} \times \mathbf{B})_n\right] = 0 \tag{2.56}$$

The parameters of these equations are the same as those found in the MHD equations: $\mathbf{u}$ is the flow speed in the discontinuity reference frame, the indices n represent normal quantities, and the others are regular plasma parameters. Quantities between squared brackets $[(\bullet)] = 0$ indicate that they are conserved across the discontinuity stream, i.e., $[\Psi] = \Psi_2 - \Psi_1$. Equation (2.54) represents the conservation of mass flux, equation (2.55) the conservation of momentum flux, equation (2.56) represents the energy conservation.

These equations can still be written in a more straightforward way. The electric field in equation (2.56) can be eliminated by using $\mathbf{E} = -\mathbf{u} \times \mathbf{B}$ and the triple vector product identity $(\mathbf{F} \times \mathbf{G}) \times \mathbf{H} = (\mathbf{F} \cdot \mathbf{H})\mathbf{G} - (\mathbf{G} \cdot \mathbf{H})\mathbf{F}$. The scalar products of equation (2.55) with the unitary vectors $\hat{\mathbf{n}}$ and $\hat{\mathbf{t}}$ generate equations (2.58) and (2.59) below. The Maxwell equations require that the normal component of the magnetic field and the tangential component of the electric field are conserved through the discontinuity surface [*Jackson*, 1999]. Then, the complete set of the RH jump conditions is given by

$$[\rho u_n] = 0 \tag{2.57}$$

$$\left[\rho u_n^2 + P + \frac{B_t^2}{2\mu_0}\right] = 0 \tag{2.58}$$

$$\left[\rho u_n u_t - \frac{B_n B_t}{\mu_0}\right] = 0 \tag{2.59}$$

$$\left[\left(\frac{1}{2}\rho u^2 + \frac{\gamma P}{\gamma - 1} + \frac{B^2}{\mu_0} - (\mathbf{u} \cdot \mathbf{B})\frac{B_n}{\mu_0}\right) u_n\right] = 0 \tag{2.60}$$

$$[B_n] = 0 \tag{2.61}$$

$$[E_t] = [\mathbf{u}_n \times \mathbf{B}_t + \mathbf{u}_t \times \mathbf{B}_n] = 0 \tag{2.62}$$

It should be mentioned at this point that MHD shock waves correspond to only one type of discontinuities found in the solar wind. Shock waves correspond to the most complicated type of MHD discontinuities due to the fact that all plasma parameters in the RH equations may vary. The other solar wind discontinuities are the contact discontinuity (CD), the tangential discontinuity (TD), and the rotational discontinuity (RD), first suggested by *Landau and Lifshitz* [1960]. Properties of different discontinuities in the solar wind have been discussed by several authors [*Colburn and Sonett*, 1966; *Siscoe et al.*, 1969; *Ivanov*, 1971; *Gurnett and Bhattacharjee*, 2005; *Tsurutani et al.*, 2011].

There is no plasma flow across a CD surface, which means $v_n = 0$. However, the plasma

	CD[a]	TD[b]	RD[c]	Shock wave
Normal speed	null	null	$\neq 0$	$\neq 0$
Jump in Plasma Density	$\neq 0$	$\neq 0$	null	$\neq 0$
Normal magnetic field	null	$\neq 0$	$\neq 0$	null or $\neq 0$

[a] Contact Discontinuity.
[b] Tangential Discontinuity. A TD is a particular case of a CD in which $B_n = 0$.
[c] Rotational Discontinuity.

Table 2.1: Classification of the MHD discontinuities accordingly to normal speed, normal magnetic field, and density variations across the discontinuity.

density suffers jumps across the CD surface, or $[\rho] \neq 0$. In the particular case of a CD in which $B_n = 0$, this discontinuity is called a TD. This difference was observed by *Smith* [1973] using Mariner 5 data. In a TD the plasma flow and magnetic field are parallel to the discontinuity surface. An RD has no jump in plasma density, $[\rho] = 0$, but plasma flows across an RD surface. The pressure does not change across an RD surface, or $v_n \neq 0$. Table 2.1 summarizes the main properties of CDs, TDs, RDs and shock waves. CDs are much more difficult to be identified due to the rapid diffusion of plasma along the surface magnetic field lines, and the jump becomes very smooth [*Colburn and Sonett*, 1966; *Burlaga*, 1971]. However, more recently, *Hsieh et al.* [2014] discussed the possibility of CD observations. Based on the rarity of identification and consequently the observation of solar wind discontinuities other then MHD shock waves, the former do not take part in the scope of this dissertation. Therefore, from now on, we will only consider MHD shock waves propagating in the interplanetary space in our MHD discontinuity analyses.

2.3.2 Shock normal decomposition

To describe how interplanetary (IP) shocks propagate in the interplanetary medium, it is necessary to define the shock normal in terms of polar angles θ_{x_n} , the angle between the shock normal and the GSE Sun-Earth line, and the clock angle φ_{y_n} , the angle between the shock normal with the GSE Y axis. The ranges of these angles are $0 \leq \theta_{x_n} \leq \pi$ and $0 \leq \varphi_{y_n}$

$\leq 2\pi$ respectively, as described by *Viñas and Scudder* [1986]. In spherical coordinates, the normal components of the vector $\mathbf{n} = (n_x,n_y,n_z)$ are given by the orthonormal system of coordinates

$$\begin{aligned} n_x &= \cos\theta_{x_n} \\ n_y &= \sin\theta_{x_n}\cos\varphi_{y_n} \\ n_z &= \sin\theta_{x_n}\sin\varphi_{y_n} \end{aligned} \tag{2.63}$$

which satisfy $|\mathbf{n}| = 1$ as a normalization condition. Therefore, translated from the shock frame of reference to a Cartesian frame of reference defined in GSE coordinates, the magnetic field (and also the velocity) is written as

$$\begin{pmatrix} B_x \\ B_y \\ B_z \end{pmatrix} = \begin{pmatrix} \cos\theta_{x_n} & -\sin\theta_{x_n} & 0 \\ \sin\theta_{x_n}\cos\varphi_{y_n} & \cos\theta_{x_n}\cos\varphi_{y_n} & -\sin\varphi_{y_n} \\ \sin\theta_{x_n}\sin\varphi_{y_n} & \cos\theta_{x_n}\sin\varphi_{y_n} & \cos\varphi_{y_n} \end{pmatrix} \begin{pmatrix} B_n \\ B_t \\ 0 \end{pmatrix} \tag{2.64}$$

The RH equations are solved in the special frame of reference in which the shock is stationary. The magnetic field is invariant because the system is non-relativistic, so $\mathbf{B}' = \mathbf{B}$ where prime-quantities are in the frame of reference where observations are made [*Jackson*, 1999]. All calculations are computed in the de Hoffmann-Teller frame of reference, where $\mathbf{v} \parallel \mathbf{B}$ and as a result the electric field vanishes in this reference frame [*de Hoffmann and Teller*, 1950]. Then it is necessary to calculate a Galilean transformation, from the shock frame of reference to another frame of reference that may be a spacecraft or the Earth. Therefore, defining the shock speed as $\mathbf{v}_s = v_s\mathbf{n}$, with $\mathbf{n}$ represented by equations (2.62),

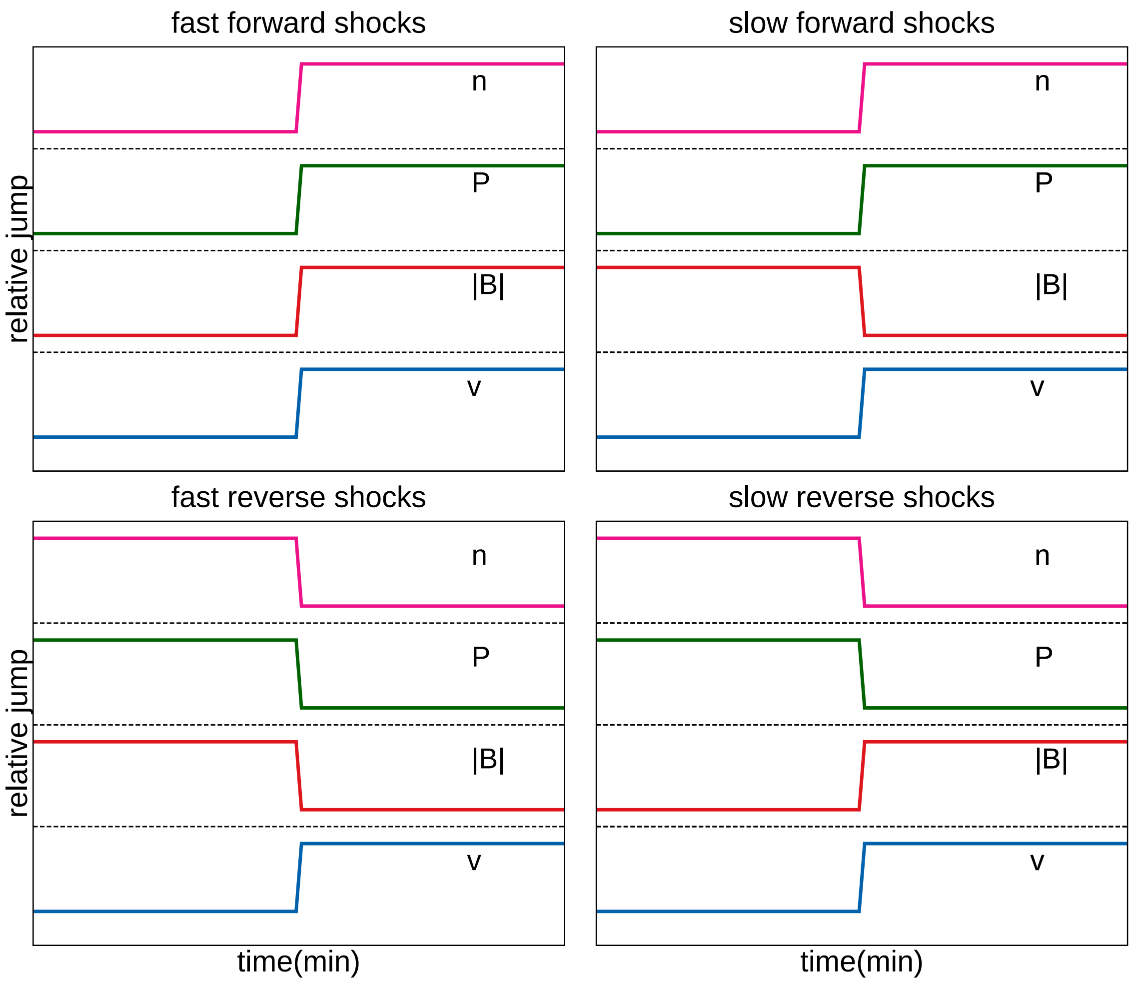

Figure 2-2: Schematic variations of the parameters n, P, B, and v for the four types of interplanetary shocks. Upper panels: left, fast forward, and right, slow forward shocks. Bottom panels, left, fast reverse, and right, slow reverse shocks.

this transformed velocity is given by

$$\mathbf{v} = \mathbf{u} + \mathbf{v}_s \tag{2.65}$$

2.3.3 Types of shocks

The following discussion about types and classifications of shocks is based on descriptions found in *Landau and Lifshitz* [1960], in *Burlaga* [1995], and in a more recent review by

Tsurutani et al. [2011]. As has already been discussed, the solar wind has different typical speeds. The magnetosonic speed depends both on the sound and the Alfvén speeds. When the relative shock speed, calculated in the shock frame of reference, is greater than the magnetosonic speed, the shock is classified as a fast shock. For the other case, the shock is said to be slow. If the shock propagates away from the Sun, it is classified as forward. Then, if the shock propagates toward the Sun, the shock is said to be reverse, although all shocks propagate toward the Earth because they are dragged by the solar wind [*Richter et al.*, 1985]. As a result, shocks can be classified as fast and slow forward, and fast and slow reverse. Figure 2-2 shows qualitatively how the plasma parameters vary after the shock takes place. In the case of IP shocks propagating in the heliosphere, fast forward shocks (FFSs) are more frequent and cause more disturbances in the Earth's magnetosphere [*Berdichevsky et al.*, 2000; *Jurac et al.*, 2002; *Echer et al.*, 2003]. Plasma density, magnetic field, temperature, and speed have positive jumps in FFSs. In all cases, the shock speed is measured in the Earth's or spacecraft's frame of reference.

Figure 2-3 represents a real FFS observed by ACE on 23 June 2000 at 1226 UT. Typically, jumps in plasma parameters and magnetic field associated with FFS are very sharp, as can be seen in Figure 2-3, from top to bottom: magnetic field, thermal plasma pressure, particle number density, speed, and dynamic pressure proportional to ρv^2. The increase in the dynamic pressure is a result of the shock compression and shock enveloping of the Earth's magnetosphere. As a result, a myriad of events can be measured on the ground after the impact of an FFS.

The presence of the magnetic field vector in the space plasma introduces an additional complexity in relation to an ordinary gas because the angle between the magnetic field vector and the shock normal plays an important role in determining downstream plasma parameters. Thus, an IP shock can be classified as either perpendicular or oblique [*Landau*

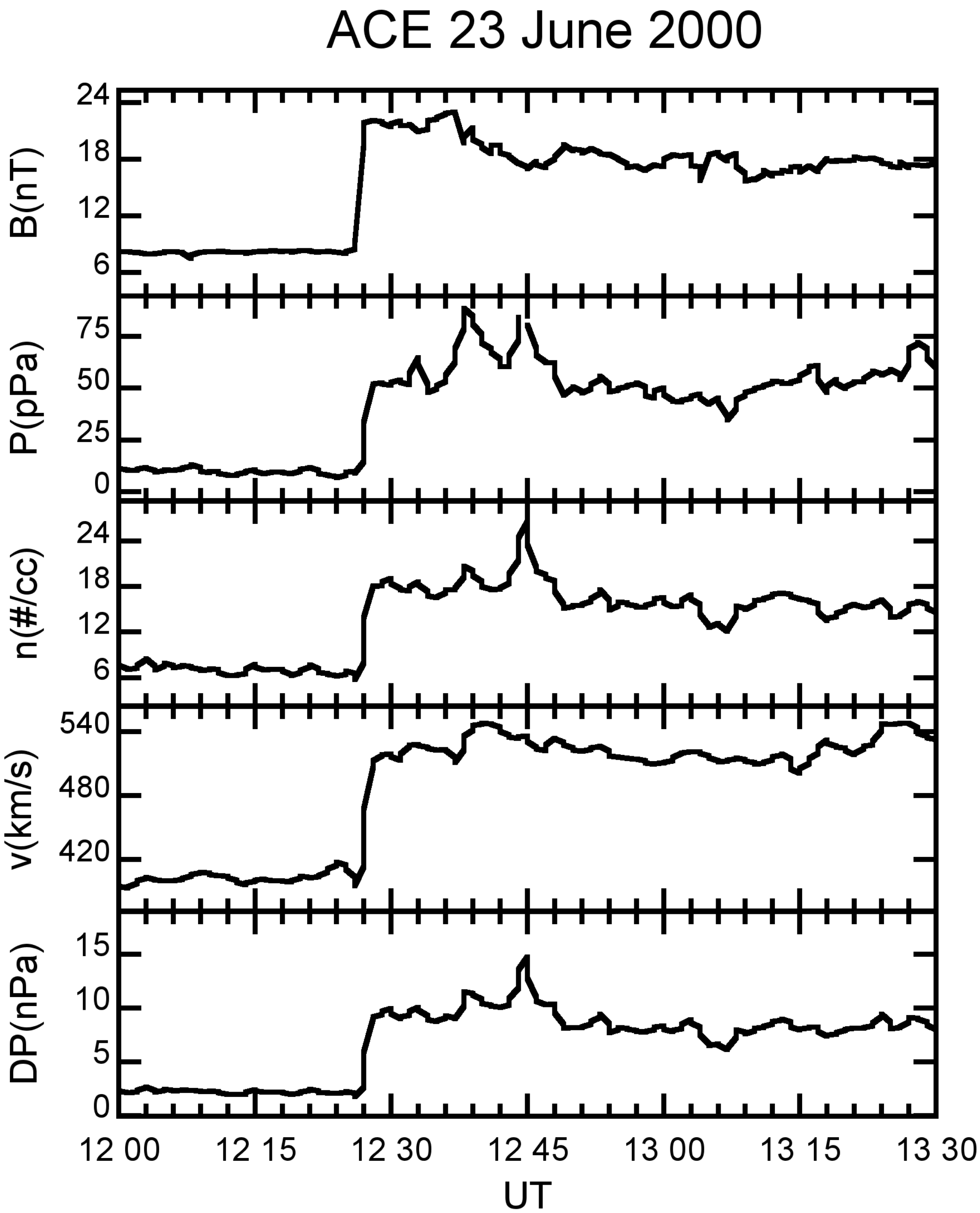

Figure 2-3: A FFS observed by ACE spacecraft on 23 June 2000 at 1226 UT. Jumps in all plasma parameters are step-like and positive. The increase of the dynamic pressure ρv^2 indicates the occurrence of an IP shock as well.

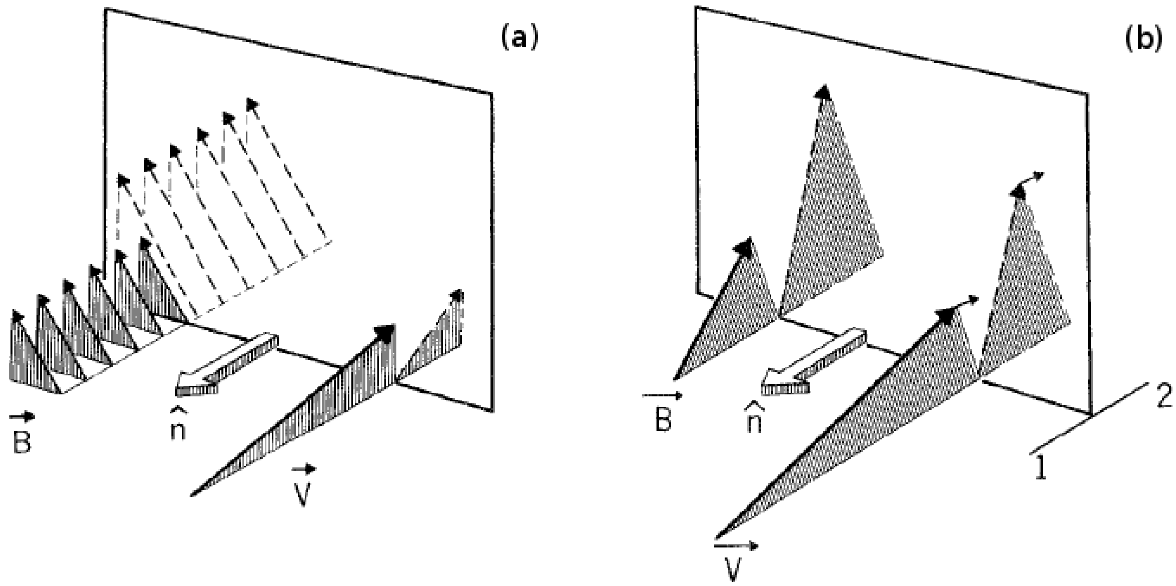

Figure 2-4: Schematic representation of fast forward shocks (FFSs) in the shock frame. Panel (a) represents a perpendicular shock in which the magnetic field lies in the plane perpendicular to the shock normal, the tangential plane. In this case, the magnitude of the magnetic field downstream increases in relation to its upstream magnitude. The opposite occurs to the velocity. Panel (b) shows an oblique shock, with the magnetic field lying in both planes. The shock speed increases in this case. The shock normal is defined pointing to the upstream region, the low entropy region. Figure extracted from *Burlaga* [1995].

and Lifshitz, 1960; *Burlaga*, 1971, 1995]. In general, perpendicular and oblique shocks are defined as follows. In the former case, the angle between the magnetic field vector and the shock normal, the obliquity θ_{B_n} , is 90^o. In the latter case, θ_{B_n} is 45^o. When this angle is 0^o, the shock is said to be parallel. Figure 2-4 shows both magnetic and velocity vectors in the shock frame of reference for an FFS case. On the left-hand-side, the magnetic field lies in the plane perpendicular to the plane containing the shock normal. The downstream magnetic field increases and the velocity decreases. The same occurs in the case of an oblique shock, represented on the right-hand-side of the same figure. Generally, the shock normal orientation is necessary to obtain θ_{B_n} , but *Chao and Hsieh* [1984] showed that it is possible to calculate the shock obliquity knowing only upstream and downstream plasma parameters.

The shock obliquity θ_{B_n} plays a significant role in energetic particle acceleration at interplanetary traveling shocks [*Lee*, 1983]. *Edmiston and Kennel* [1984] and *Kennel* [1987] introduced the concept of shock critical Mach numbers (Mc) which depend upon the obliquity θ_{B_n} and the upstream plasma β. If the shock has a Mach number greater than a determined Mc, the shock is said to be supercritical. If the shock is supercritical, electron resistivity and ion viscosity dissipation may occur at the shock. Recently, *Zhou and Smith* [2015] showed that approximately 1/3 of IP shocks driven by ICMEs are supercritical and 2/3 of IP shocks driven by CIRs are supercritical.

Now let us take the Earth's interaction with the solar wind. As discussed in Chapter 1, a stationary shock, for example, the bow shock, is formed in front of the Earth's magnetosphere due to its interaction with the solar wind. Figure 2-5, taken from *Kennel et al.* [1985] shows the bow shock is the diffuse hyperbolically shaped region standing at a distance in front of the magnetopause. The bow shock has a complicated magnetic structure, with a "foot", a "ramp", and an "overshoot". Overshoots occur in the bow shock due to the fact that jumps in magnetic field often exceed those predicted by the RH conditions [*Russell et al.*, 1982; *Leroy et al.*, 1981; *Livesey et al.*, 1982]. The inclined blue lines represent the IMF. In this figure they lie in the equatorial plane. The direction of the shock normal is indicated at two positions. Where it points perpendicularly to the IMF the character of the bow shock is perpendicular. In the vicinity of this point where the IMF is tangent to the bow shock the shock behaves quasi-perpendicularly. When the shock normal is aligned with or against the IMF the bow shock behaves as a quasi-parallel shock. Quasi-perpendicular shocks are magnetically quiet compared to quasi-parallel shocks [*Balogh and Treumann*, 2013]. This is indicated here by the gradually increasing oscillatory behavior of the magnetic field when passing along the shock from the quasi-perpendicular part into the quasi-parallel part. Correspondingly, the behavior of the plasma downstream of the shock is strongly disturbed behind the quasi-perpendicular shock. The bow shock is often found

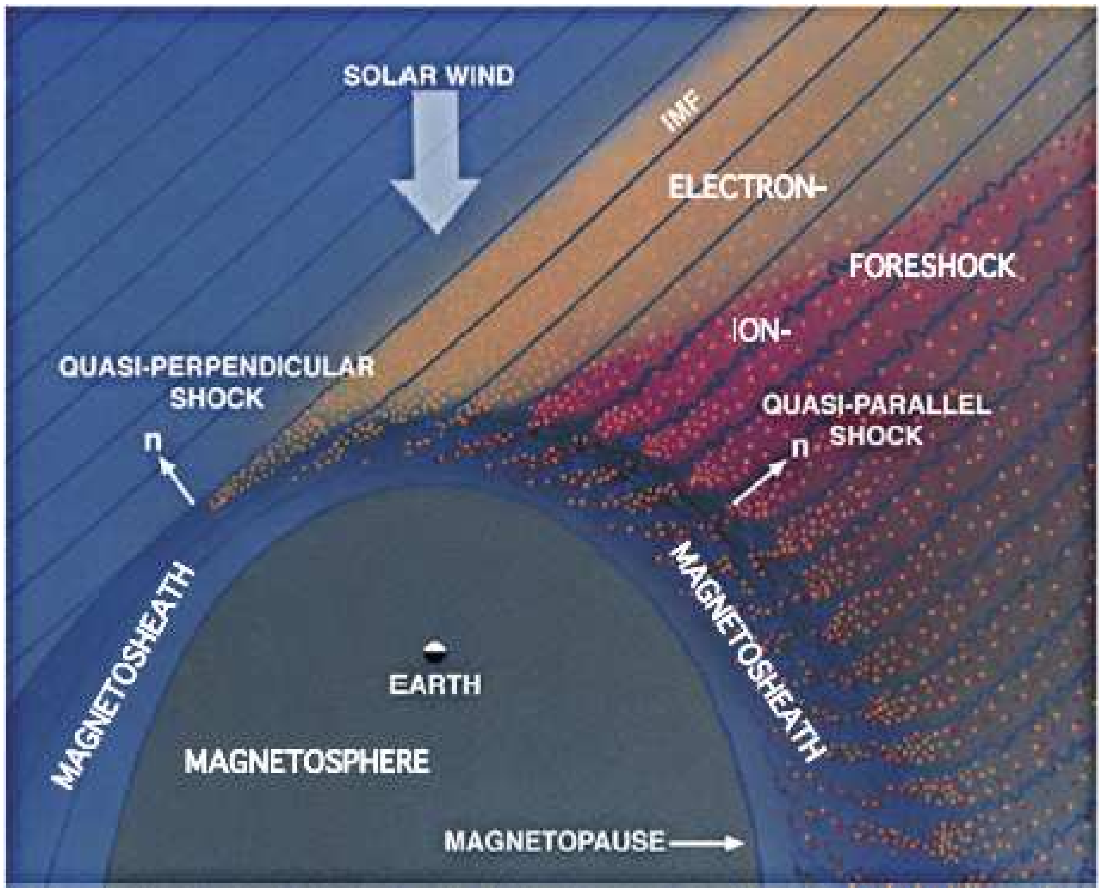

Figure 2-5: Representation of the solar wind interaction with the Earth's bow shock after [*Kennel et al.*, 1985]. Quasi-perpendicular and quasi-parallel shocks are shown. Blue lines represent the IMF. The shocked region is the magnetosheath.

to be supercritical

Finally, when the shock is supercritical, as is the case for the bow shock, electrons and ions are reflected from it. Reflection is strongest at the quasi-perpendicular shock but particles can escape upstream only along the magnetic field. Hence the upstream region is divided into an electron (yellow) and an ion foreshock accounting for the faster escape speeds of electrons than ions. More details on the shock behavior of the bow shock can be found in *Russell* [1985], and the interaction of solar wind discontinuities and interplanetary shocks are discussed by *Yan and Lee* [1996].

2.3.4 RH solutions for perpendicular and oblique shocks

In this section we solve the RH equations for the specific cases of perpendicular and oblique shocks. Our task is to find relationships between upstream and downstream shock parameters. Equations (2.57-62) are written explicitly in terms of upstream (1) and downstream (2) parameters. The shock compression ratio is defined as the ratio of the downstream plasma density to upstream plasma density, i.e., $X \equiv \rho_2/\rho_1$. From the mass conservation equation (2.57), this choice implies that $u_2/u_1 = X^{-1}$. All other conditions will depend on the compression ratio X.

In the case of perpendicular shocks, where $\theta_{B_n} = 90^o$, the magnetic field lies in the plane which contains the discontinuity and does not have a normal component (see Figure 2-4). Then, from the relation for the velocity, we get $B_2/B_1 = X$. By rewriting equation (2.58) explicitly with $u_n = u$ and $B_t = B$, we get

$$\rho_2 u_2^2 + P_2 + \frac{B_2^2}{2\mu_0} = \rho_1 u_1^2 + P_1 + \frac{B_1^2}{2\mu_0} \tag{2.66}$$

By dividing the above equation by P_1, using the sonic Mach number M_S (equation (2.45)), and equation (2.61), and the plasma beta, after some manipulations, we get

$$\frac{P_2}{P_1} = \gamma M_S^2 \left(1 - \frac{1}{X}\right) + \frac{1}{\beta}(1 - X^2) + 1 \tag{2.67}$$

Table 2.2 summarizes the results for the RH equations obtained in the case of perpendicular shocks.

The solutions for oblique shocks are more complicated because $\theta_{B_n} \neq 90^o$ and all normal and tangential components of magnetic field and velocity are not null. Here we choose the de Hoffmann-Teller reference frame, so $\mathbf{u}_1 \times \mathbf{B}_1 = \mathbf{u}_2 \times \mathbf{B}_2 = 0$. This choice yields the

Perpendicular shocks, $\theta_{B_n} = 90^o$	
compression ratio	$X = \frac{\rho_2}{\rho_1}$
velocity	$\frac{u_2}{u_1} = \frac{1}{X}$
magnetic field	$\frac{B_2}{B_1} = X$
plasma pressure	$\frac{P_2}{P_1} = \gamma M_S^2 \left(1 - \frac{1}{X}\right) + \frac{1}{\beta}(1 - X^2) + 1$

Table 2.2: RH solutions for perpendicular shocks.

following relationships

$$u_{1t} = \frac{u_{1n} B_{1t}}{B_{1n}} \quad \text{and} \quad u_{2t} = \frac{u_{2n} B_{2t}}{B_{2n}} \tag{2.68}$$

whose ratio is given by

$$\frac{u_{2t}}{u_{1t}} = \frac{1}{X} \frac{B_{2t}}{B_{1t}} \tag{2.69}$$

In order to find a relationship between the upstream and downstream velocity and magnetic field, we write equation (2.59) explicitly in terms of upstreams and downstream parameters

$$\rho_2 u_{2n} u_{2t} - \frac{B_{2n} B_{2t}}{\mu_0} = \rho_1 u_{1n} u_{1t} - \frac{B_{1n} B_{1t}}{\mu_0} \tag{2.70}$$

and, after solving for u_{2t}/u_{1t} using the compression ratio and the Alfvèn speed, we get

$$\frac{u_{2t}}{u_{1t}} = \frac{u_1^2 - v_A^2}{u_1^2 - X v_A^2} \quad \text{and} \quad \frac{B_{2t}}{B_{1t}} = \frac{X(u_1^2 - v_A^2)}{u_1^2 - X v_A^2} \tag{2.71}$$

The choice of the de Hoffmann-Teller reference frame assures that all magnetic terms in equation (2.60) vanish. As a result, solving for P_2/P_1, we get

$$\frac{P_2}{P_1} = X + \frac{1}{2}(\gamma - 1) X M_S^2 u_1^2 \left(1 - \frac{u_2^2}{u_1^2}\right) \tag{2.72}$$

Oblique shocks, $\theta_{B_n} \neq 90^o$	
compression ratio	$X = \frac{\rho_2}{\rho_1}$
normal velocity	$\frac{u_{2n}}{u_{n1}} = \frac{1}{X}$
tangential velocity	$\frac{u_{2t}}{u_{1t}} = \frac{u_1^2 - v_A^2}{u_1^2 - Xv_A^2}$
normal magnetic field	$\frac{B_{2n}}{B_{1n}} = X$
tangential magnetic field	$\frac{B_{2t}}{B_{1t}} = \frac{X(u_1^2 - v_A^2)}{u_1^2 - Xv_A^2}$
plasma pressure	$\frac{P_2}{P_1} = X + \frac{1}{2}(\gamma - 1)XM_S^2 u_1^2 \left(1 - \frac{u_2^2}{u_1^2}\right)$

Table 2.3: RH solutions for oblique shocks.

The results obtained for oblique shocks are summarized in Table 2.3.

The solutions obtained from the RH equations in this chapter were calculated for two different obliquities, i.e., for perpendicular ($\theta_{B_n} = 90^o$) and oblique ($\theta_{B_n} \neq 90^o$) MHD shocks. In the oblique shock case, the reference frame was chosen that the magnetic field and the velocity vectors are parallel, which implies that the tangential electric field along the shock is null [*de Hoffmann and Teller*, 1950]. These solutions are used in Chapter 4 to calculate downstream from upstream plasma parameters for two different interplanetary shocks, a perpendicular shock and an oblique shock in the shock frame of reference. Equations (2.63) were used to translate all plasma parameters from the shock reference frame to the Earth's (or spacecraft's) frame of reference.

2.3.5 Shock speed and normal calculation methods

Once one has the observed shock parameters, i.e., upstream and downstream IMF and plasma parameters, the shock speed can be calculated using the RH equations (2.57-62). The fluid velocity is taken in the Earth's frame of reference. Taking equation (2.57), it is possible to write the shock speed as

$$v_s = \frac{[\rho \mathbf{v}]}{[\rho]} \cdot \mathbf{n}\,, \tag{2.73}$$

where $\mathbf{v}$ is the relative speed of the shock in relation to the medium. However, the shock normal is still to be determined.

The IP shock normal is one of the most important features to be understood in a shock. Throughout the years, many single spacecraft shock normal methods have been suggested, such as the magnetic coplanarity [*Colburn and Sonett*, 1966; *Lepping and Argentiero*, 1971], velocity coplanarity and plasma/IMF data mixed methods [*Abraham-Shrauner and Yun*, 1976], and the interactive scheme by *Viñas and Scudder* [1986], later improved by *Szabo* [1994]. A summary of IP shock normal calculation methods can be found in *Schwartz* [1998].

Thus, the equations for the most important single spacecraft methods to determine shock normal orientations are the magnetic coplanarity:

$$\mathbf{n}_{MC} = \frac{\mathbf{B}_2 \times \mathbf{B_1} \times [\mathbf{B}]}{|\mathbf{B}_2 \times \mathbf{B_1} \times [\mathbf{B}]|}\,, \tag{2.74}$$

the plasma/IMF data mixed methods:

$$\mathbf{n}_{MX1} = \frac{(\mathbf{B}_1 \times [\mathbf{v}]) \times [\mathbf{B}]}{|(\mathbf{B}_1 \times [\mathbf{v}]) \times [\mathbf{B}]|} \tag{2.75}$$

$$\mathbf{n}_{MX2} = \frac{(\mathbf{B}_2 \times [\mathbf{v}]) \times [\mathbf{B}]}{|(\mathbf{B}_2 \times [\mathbf{v}]) \times [\mathbf{B}]|} \tag{2.76}$$

$$\mathbf{n}_{MX3} = \frac{([\mathbf{B}] \times [\mathbf{v}]) \times [\mathbf{B}]}{|([\mathbf{B}] \times [\mathbf{v}]) \times [\mathbf{B}]|} \tag{2.77}$$

and the velocity coplanarity:

$$\mathbf{n}_{VC} = \frac{[\mathbf{v}]}{|[\mathbf{v}]|}\,. \tag{2.78}$$

Equations (2.74-78) were used to build an IP shock data base to conduct a statistical study of IP shocks. More details about this shock study will be discussed in Chapter 6 and can be found in the papers *Oliveira and Raeder* [2015] and *Oliveira et al.* [2015].

Chapter 3

OpenGGCM Model

3.1 Introduction

In this dissertation, we use the Open Geospace General Circulation Model (OpenGGCM) to study the impact of IP shocks on the Earth's magnetosphere with simulations. The OpenGGCM is a global coupled model of Earth's magnetosphere, ionosphere, and thermosphere, which covers the whole area of interest in our study. The first versions of the OpenGGCM code came about back in the 1990's at the University of California in Los Angeles. OpenGGCM requires a particular aspect of computation methods. Since the code covers large regions of the magnetosphere with fine resolution, OpenGGCM has to run simultaneously using a large number of computers in a straightforward amount of time. To achieve its goal, the code must be parallelized using MPI (Method Parsing Interface) [*Gilson*, 2011]. More general and technical information about OpenGGCM can be found at the OpenGGCM wiki page`http://openggcm.sr.unh.edu/wiki/index.php/Main_Page`.

The OpenGGCM code is available at the Community Coordinated Modeling Center (`ccmc.nasa.gov`) as a community model for model runs on demand [*Rastätter et al.*, 2013; *Pulkkinen et al.*, 2011, 2013]. The magnetosphere part solves the MHD equations as an initial-boundary-value problem. The MHD equations are solved to within ~3 R_E of Earth. The region within 3 R_E is treated as a magnetosphere-ionosphere (MI) coupling region where

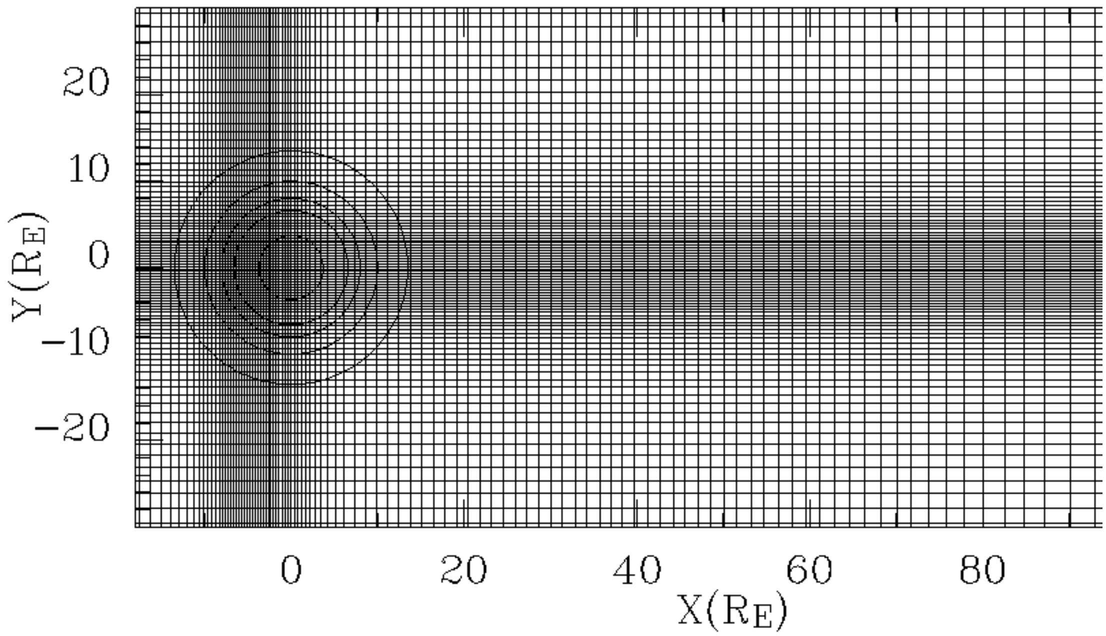

Figure 3-1: Example of an OpenGGCM stretched cartesian grid in the modified GSE XY plane used in our simulations (note that $X' = -X_{GSE}$). Here the resolution is approximately twenty times less than in our actual simulations. Regions close to the Earth and the magnetotail are of higher resolutions.

physical processes that couple the magnetosphere to the ionosphere-thermosphere system are parameterized using simple models and relationships. The ionosphere-thermosphere system is modeled using the NOAA CTIM (Coupled Thermosphere Ionosphere Model [*Fuller-Rowell et al.*, 1996; *Raeder et al.*, 2001a]). The OpenGGCM has been described with some detail in the literature [see, e.g. *Raeder et al.*, 2001b; *Raeder*, 2003; *Raeder et al.*, 2008]; we thus refer the reader to these papers for more details. The OpenGGCM has been used for numerous studies, including studies of substorms [*Raeder et al.*, 2001b; *Ge et al.*, 2011; *Gilson et al.*, 2012; *Raeder et al.*, 2013], storms [*Raeder et al.*, 2001a; *Raeder and Lu*, 2005; *Rastätter et al.*, 2013; *Pulkkinen et al.*, 2013], reconnection [*Connor et al.*, 2014], and, most relevant for this study, for the study of IP shock impacts [*Shi et al.*, 2013].

3.2 Simulation domain and grids

The OpenGGCM code uses a modified version of the cartesian GSE (Geocentric Solar Ecliptic) coordinate system. In this coordinate system, the X axis points toward the Sun, the Y axis points dusk-ward (opposite direction of the Earth's motion around the Sun), and the Z axis points perpendicularly northward to the ecliptic plane to complete the coordinate system. Therefore, during computations, OpenGGCM modifies the GSE coordinates by taking $X' = -X_{GSE}$, $Y' = -Y_{GSE}$, and $Z' = Z_{GSE}$. Simulation domains typically run from $30\mathrm{R_E}$ upstream the Earth and $300\mathrm{R_E}$ down the tail. To complete the simulation box, the geometrical domain reaches $50\mathrm{R_E}$ in the Y and Z directions in a typical run.

The grids used in the OpenGGCM simulations are called "stretched-cartesian" grids [*Raeder*, 2003]. The stretched-cartesian grids are adaptable to each particular simulation because one can define the regions where high definition is desired. Grid cells can be taken smaller in areas of desired larger resolutions. These regions are typically close to the Earth and the magnetotail.

Figure 3-1 and 3-2 represent examples of grids used in OpenGGCM simulations in the modified XY and YZ GSE planes. These grids use approximately 2 million cells. The actual grids used by the simulations in this dissertation used about 40 million cells. Both plots show regions of high resolution in the magnetotail and regions close to the Earth.

More details about the model, such as governing equations, numerics, boundary conditions and coupling of different regions are outlined by *Raeder* [2003]. OpenGGCM has also been discussed and summarized by other Ph.D. theses supervised by Professor Raeder available at his website `http://mhd.sr.unh.edu/~jraeder/tmp.homepage/?section=00theses`.

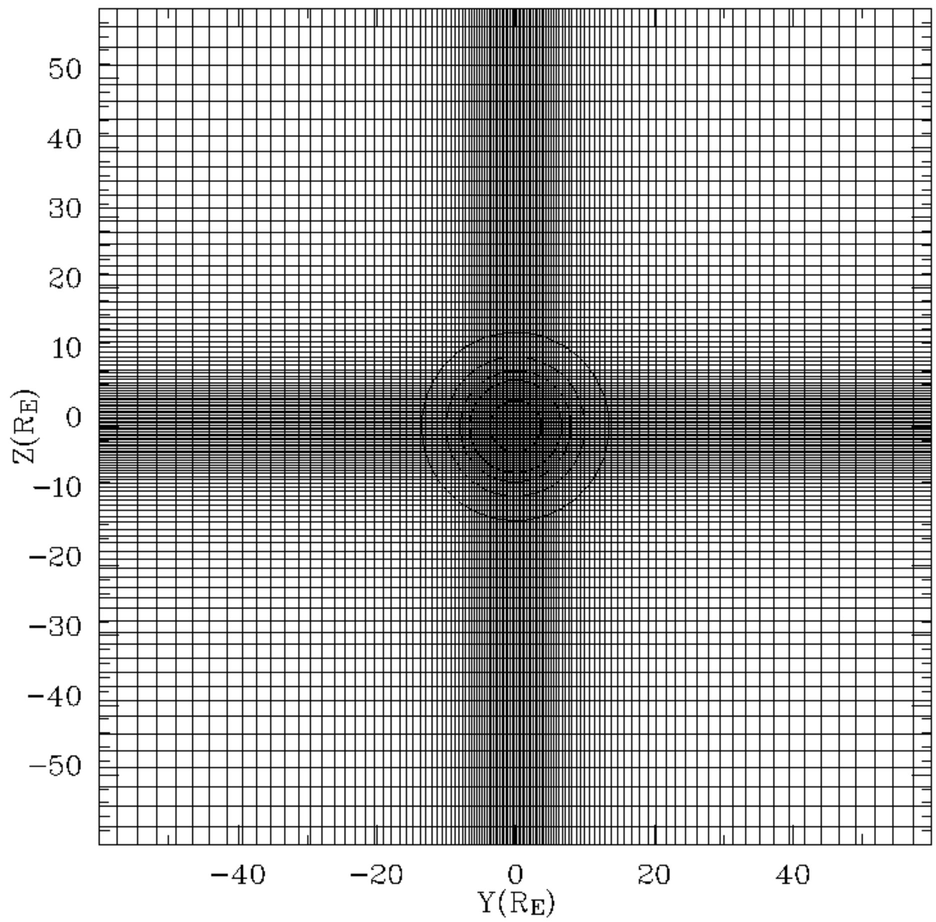

Figure 3-2: OpenGGCM stretched cartesian example grid in the GSE YZ plane used in our simulations. Note the regions of high resolution are close to the Earth. OpenGGCM uses a modified version of the GSE coordinate system in which $Y' = -Y_{GSE}$. The resolution of the actual simulations discussed in this dissertation are approximately twenty times higher.

Chapter 4

Simulation results

4.1 Introduction

This chapter is a version of a paper Professor Raeder and I published concerning our global MHD simulation results [*Oliveira and Raeder*, 2014]. We found that two interplanetary (IP) shocks with different strengths (Mach numbers) may lead to different geomagnetic activity in the nightside ionosphere (field aligned currents and diffusive auroral electron precipitation energy flux) if they impact the Earth with different shock impact angles θ_{x_n} . Thus, such results suggested us to investigate satellite and geomagnetic data seeking these evidences. The observational results obtained from this study are presented in Chapter 6.

4.2 Shock Impacts

4.2.1 Simulation setup

In our simulations we use exclusively GSE (Geocentric Solar Ecliptic) coordinates in our simulation input data. The numerical box extends from the Earth 30 R_E in the Sun-ward direction, and 300 R_E down the tail. In the directions perpendicular to the Sun-Earth line, i.e., in the Y and Z directions, the numerical box extends to ±50 R_E. The numerical grid is non-equidistant Cartesian and is divided into 610×256×256 grid cells, such that the highest resolution is closest to Earth (see Chapter 3). Specifically, the grid resolution is

0.15 R_E within a distance of 10 R_E radially from the Earth. The inner boundary, where the magnetosphere variables connect via field-line mapping to the ionosphere is located at 3 R_E.

In this paper [*Oliveira and Raeder*, 2014] we only consider IP shocks for which the shock normal lies in the GSE XZ plane. Furthermore, we assume that the IMF also has no GSE y-component. Thus, the shock geometry relative to the Earth and to the IMF depends exclusively on two angles. First, depending on the shock normal relative to the upstream (relative to the shock) magnetic field direction, a shock can be classified as perpendicular, oblique, or parallel [*Burlaga*, 1971; *Tsurutani et al.*, 2011]. As is often found in the literature [*Burlaga*, 1971; *Tsurutani et al.*, 2011], when $0^o < \theta_{B_n} \leq 30^o$, the shock is classified as almost parallel. In the cases in which $30^o \leq \theta_{B_n} \leq 60^o$, the shock is said to be oblique. Finally, when $60^o \leq \theta_{B_n} < 90^o$, the shock is classified as almost perpendicular. In particular for this paper, the shock is named perpendicular when $\theta_{B_n} = 90^o$. Second, in relation to the Earth's system of reference, the shock normal is decomposed in terms of two angles: the angle θ_{x_n} between the shock normal and the Sun-Earth line, and the angle φ_{y_n} in the YZ plane that completes the set, following the notation of *Viñas and Scudder* [1986]. For our simulations presented here, φ_{y_n} is always 90^o. Since quiet solar wind conditions are favorable to IP shock formation [*Borrini et al.*, 1982], we also assume average solar wind conditions, with a particle number density of 5 cm^{-3}, thermal plasma pressure of 20 pPa, magnetic field magnitude of 7 nT, and background speed of v_1 = (-400,0,0) km/s in all cases upstream of the IP shocks. We specify the shock strength by its compression ratio. As reported by *Echer et al.* [2003], most shocks near Earth have a compression ratio of the order of 2 during solar maximum. Here, we then choose a compression ratio value of 1.5 in order to have a mild shock. The MHD code input is set as follows. We transform the upstream initial conditions into the shock frame, calculate the downstream parameters, and subsequently transform them back to the Earth's system of reference. We ran simulations of different FFSs with different shock normal orientations, obliquities, shock speeds, Mach numbers, and IMF B_Z pointing either northward or southward. For brevity, we select three FFSs with different shock normal orientations and Mach numbers to discuss in detail. In the first case, the IP shock has its normal inclined with an angle θ_{x_n} of 30^o with the GSE x-axis toward the south, θ_{B_n} $=51^o$, shock speed v_s = 380 km/s, and Mach number of 3.7, i.e., an inclined oblique shock, hereafter IOS-1. The second case corresponds to an FFS, also inclined and oblique here called IOS-2, with $\theta_{x_n} = 30^o$, $\theta_{B_n} = 45^o$, $v_s = 650$ km/s, and Mach number of 7.4. In the last case the shock normal has $\theta_{x_n} = 0^o$ and was perpendicular to the IMF, i.e., a frontal perpendicular shock (FPS), with $v_s = 650$ km/s, and Mach number of 3.7. These shock speeds are consistent with the observations reported by *Berdichevsky et al.* [2000], where most FFSs have speeds in the range 50-200 km/s in the shock frame of reference. Tables 4.1, 4.2, and 4.3 show the upstream (1) and downstream (2) and other important parameters for the three FFSs. The first and second shocks impact the magnetosphere (first contact with the magnetopause) at t = 16.45 minutes, and the FPS reaches the subsolar magnetopause at t=18.28 minutes. We also simulated shocks with northward IMF and otherwise identical solar wind conditions. We found that the results were similar to the southward cases, but with weaker magnetosphere response, with the exception that transient northward B_z (NBZ) currents occurred within a few seconds after the shock impact when it was frontal. This effect was already reported by *Samsonov et al.* [2010]. We will thus focus on the case of southward IMF.

4.2.2 Results

As the IP shock impacts the magnetopause, it launches waves into the magnetosphere. The phase speed of these waves (both Alfvén and magnetosonic waves) is generally much

IOS-1, v_s = 380 km/s, M = 3.7 $\theta_{B_n} = 51^o$, $\theta_{x_n} = 30^o$						
	B_x	B_z	v_x	v_z	P	n
upstream	-1.83	-6.83	-400.00	0.00	20.0	5.0
downstream	-0.52	-9.09	-434.15	-17.65	67.45	7.5

Table 4.1: Upstream and downstream plasma parameters (B in nT, v in km/s, P in pPa, and n in particles/cm^3.) for the inclined oblique case IOS-1 with shock speed of 380 km/s and impact angle $\theta_{x_n} = 30^o$. Upstream Mach number and obliquity are also shown. Table from *Oliveira and Raeder* [2014].

IOS-2, v_s = 650 km/s, M = 7.4 $\theta_{B_n} = 45^o$, $\theta_{x_n} = 30^o$						
	B_x	B_z	v_x	v_z	P	n
upstream	-1.83	-6.83	-400.00	0.00	20.0	5.0
downstream	-0.52	-9.09	-461.53	-28.61	109.74	7.5

Table 4.2: Same plasma parameters for the inclined oblique case IOS-2 with shock speed of 650 km/s and the same impact angle as IOS-1. Table from *Oliveira and Raeder* [2014].

FPS, v_s = 650 km/s, M = 3.7 $\theta_{B_n} = 90^o$, $\theta_{x_n} = 0^o$						
	B_x	B_z	v_x	v_z	P	n
upstream	0.00	-7.07	-400.00	0.00	20.0	5.0
downstream	0.00	-10.61	-483.33	0.00	191.37	7.5

Table 4.3: Same plasma parameters for the frontal perpendicular case FPS with shock speed of 650 km/s and impact angle $\theta_{x_n} = 0^o$. Table from *Oliveira and Raeder* [2014].

larger in the magnetosphere than in the solar wind and the magnetosheath. Therefore, the amplitude of the waves diminishes in the magnetosphere, because the waves are partially reflected and also because of the higher phase speed the wave energy spreads out more quickly. In order to visualize such waves, we therefore subtract consecutive time instances from each other to remove the background as much as possible. This essentially amounts to taking the time derivative. Thus, in the plots shown below, for any quantity X, we show the difference $\Delta X = X(t) - X(t - \Delta t)$, where Δt is chosen to be 30 seconds. Figure 4-1 shows the time evolution of the total magnetic field changes (ΔB), in nT, in the noon-midnight meridian plane. The left column shows the IOS-1 case, the middle column shows the IOS-2 case, and the right column shows the FPS case. Each row shows different time, and the time difference between rows is three minutes. The red color in the color bar shows an increasing magnetic field B, and the blue color indicates where B decreases. The color bar range is ± 2 nT. In all columns, the first plots show the instant right after the FFSs crosses the bow shock.

In Figure 4-1 the shock fronts appear much broader than they really are. First, by taking differences 30 seconds apart, the shock propagates 2-3 R_E across the grid during that time, thus the shock will appear at least that wide. Second, because of numerical diffusion, the shocks have a foot or ramp on either side of the shock front. Normally, this would be hardly visible in a color-coded plot. However, because we take the differences and clamp the color bar at low values, these numerical artifacts become emphasized and make the shock appear much wider than it really is. In the simulation, the shocks are resolved to within 2-3 cells, i.e., to less than 0.5 R_E within 10 R_E from the Sun-Earth line.

As soon as the shock impacts the magnetopause, it launches Alfvén waves and magnetosonic waves into the magnetosphere. Because the wave speeds are much higher in the magnetosphere, these waves race ahead of the IP shock in the magnetosheath. The second

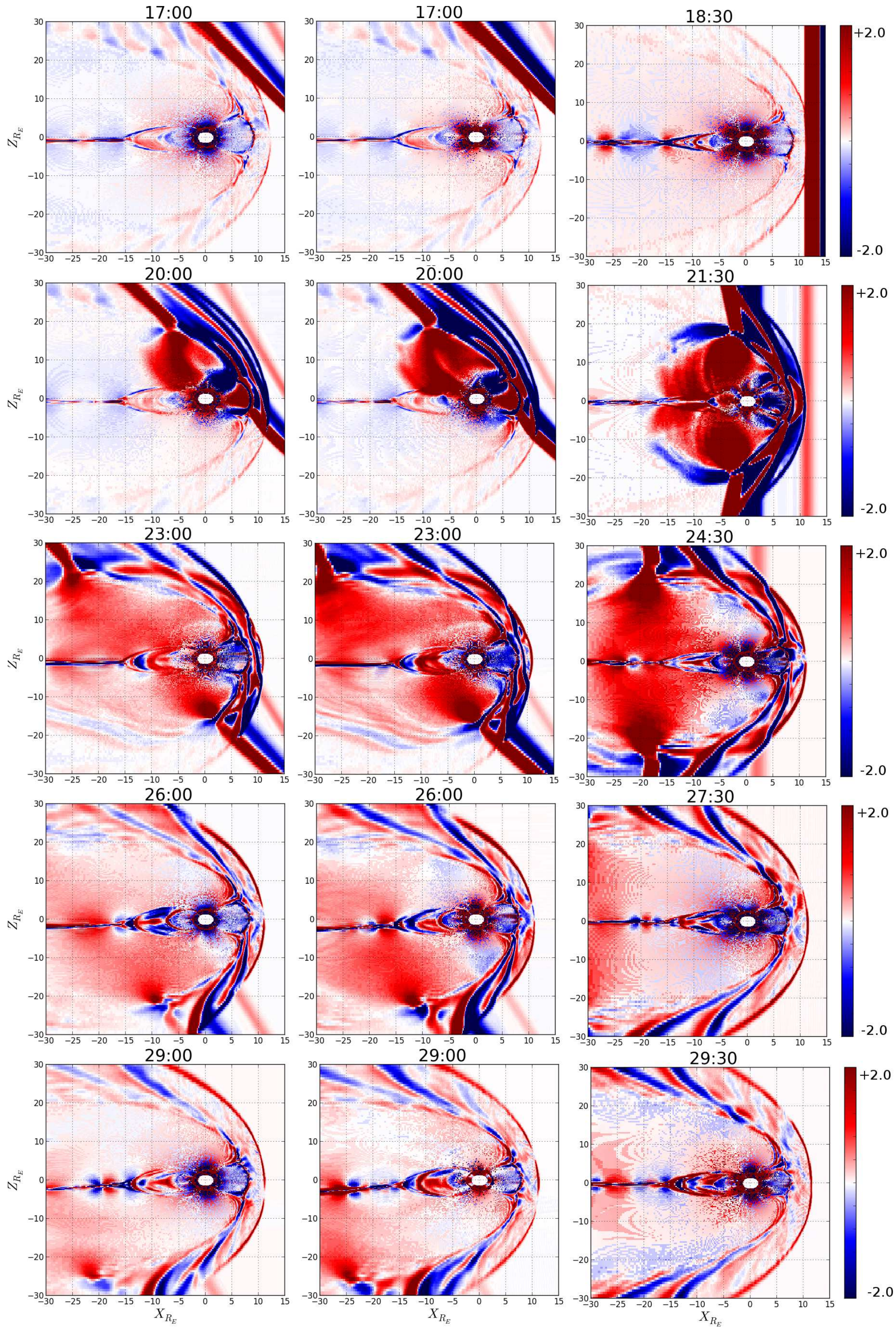

Figure 4-1: 5 consecutive frames representing the result of numerical simulations of ΔB(nT) plotted in the meridian plane with Δt = 3 minutes, in a time range of 12 minutes. From left, first column shows the IOS-1 case, central column represents the IOS-2 case, and the last column shows the FPS case. See text for details. Figure from *Oliveira and Raeder* [2014].

row shows for both cases the time just after the IP shock has impacted the magnetopause. In the IOS-1 and IOS-2 cases, the first contact between the shock and the magnetopause occurs just past the northern cusp. The induced wave propagates through the northern lobe and reaches the plasma sheet in the nightside from the north. At this time, the IP shock has not yet impacted the southern hemisphere, and consequently there is no corresponding wave in the southern hemisphere yet.

The FPS case (second row, right panel) is distinctively different. The impacts on the northern and southern lobes occur simultaneously, and symmetric waves are launched from both the northern and southern magnetopause into the magnetosphere. These waves converge on the tail plasma sheet and cause a more significant compression of the plasma sheet.

As time progresses, these waves propagate further tail-ward. In the asymmetric cases, the waves from the southern hemisphere reach the near-Earth plasma sheet approximately 3 minutes after the waves from the northern hemisphere. As a result of such asymmetric impact, there is much less compression of the plasma sheet. Instead, the entire plasma sheet is bent southward. This is best visible at the later times (fourth and fifth row), where the deflection at x=-30 R_E is as much as 3 R_E in the IOS-1 case and 4 R_E in the IOS-2 case. By contrast, in the symmetric case there is no such deflection, but instead a transient compression of the plasma sheet.

After the IP shock has passed (bottom row), the magnetosphere state seems to be very similar for the three cases. However, the particular display only shows differences to highlight transients and thus provides little information abut the state.

In order to examine the effects of the IP shocks on geomagnetic activity, we examine relevant ionospheric quantities. Figure 4-2 shows the time differences of the field-aligned current density (FAC, in $\mu A/m^2$) in the northern hemisphere polar cap, displayed in the

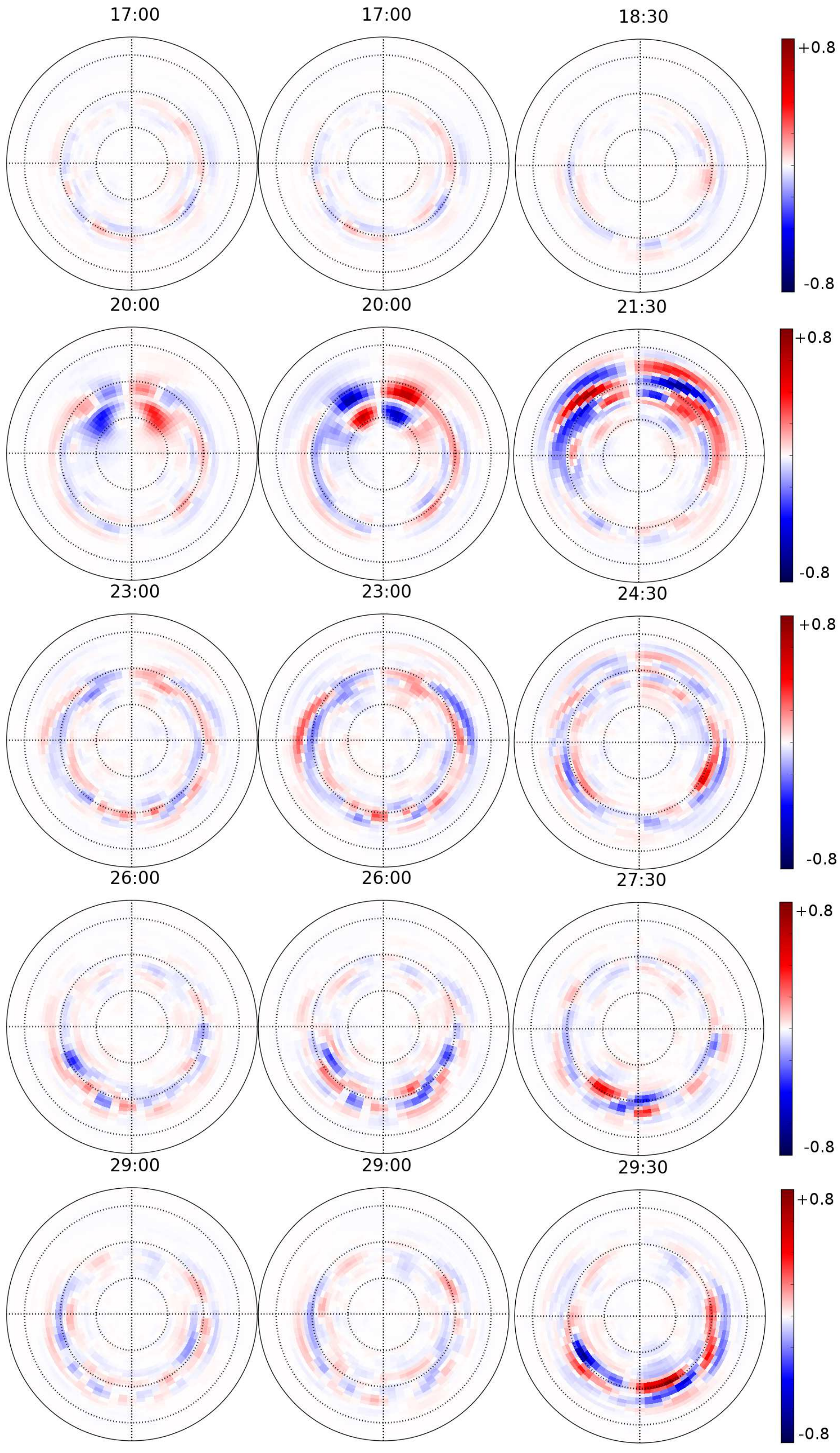

Figure 4-2: Difference of field-aligned currents, $\Delta\text{FAC}(\mu\text{A/m}^2)$, for the northern hemisphere ionosphere in the same sequence as represented in Figure 4-1. The center of each plot is the magnetic pole. The right side of each plot is dawn while the top is noon (or towards the Sun), and the bottom is the midnight. See text for details. Figure from *Oliveira and Raeder* [2014].

same way as the magnetic field evolution of Figure 4-1. The times in Figure 4-2 correspond to the times shown in Figure 4-1, i.e., a time range of 12 minutes, plotted in three minute increments. The range in the color bar is ± 0.8 μA/m^2, and regions in red indicate a positive change in FAC, while regions in blue indicate a negative change in FACs. The dashed circles represent the magnetic latitude λ_m in 10 degree increments from 55^o to the pole. Left, middle, and right columns represent the results for the IOS-1, IOS-2, and FPS cases, respectively. In all cases, in the first plot, the ionosphere is steady because the FFSs have not yet impacted the magnetopause. Also, in the three situations, the first FAC changes are seen about three minutes after the shock impact, as can be seen at t = 20:00 minutes for the inclined cases and t = 21:30 minutes for the FPS case. In the two IOS cases, the FAC changes are mostly in the vicinity of the cusp, whereas the FFS causes a broader signature that encompasses the entire dayside auroral region. The changes in the IOS-1 and IOS-2 cases are very similar geometrically, with the only difference that the IOS-2 response is slightly stronger than the IOS-1 response.

As time evolves, with the exception of the first minutes after the shock impact, the FAC signature diminishes in all cases, as can be seen in the middle row. Subsequently, activity in the nightside develops for the three cases. However, in the FPS case, the ionosphere response is much stronger. At t = 24:30 minutes, the enhancement of FACs is most evident on the nightside of the ionosphere between $\lambda_m = 70^o$ and $\lambda_m = 65^o$, and between 0300 MLT and 0600 MLT. At t = 27:30 minutes and t = 29:30 minutes, FACs are enhanced close to midnight local time, which is a typical substorm signature [*Akasofu*, 1964; *McPherron*, 1991]. The last row of Figure 4-2 shows the strongest nightside FAC variations occurring for the FPS case at t = 29:30 minutes, covering almost all the nightside ionosphere for λ_m between 70^o and 65^o. We attribute this activity due to substorm activity that was triggered by the converging waves in the plasma sheet.

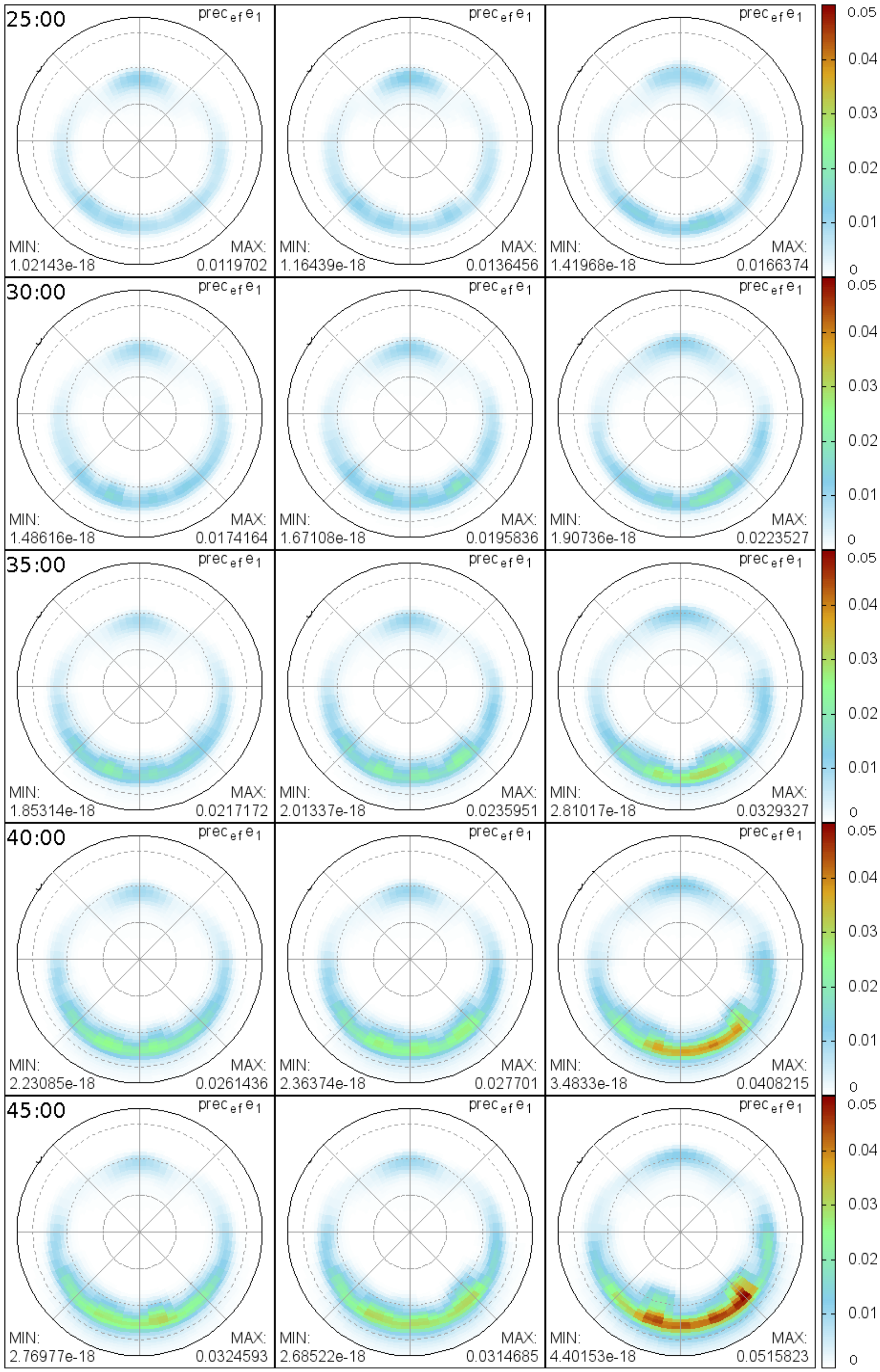

Figure 4-3: DAPEF(mW/m^2) plotted in a time range of 20 minutes with time interval of 5 minutes. The first column represents the IOS-1 case, second the IOS-2 case, and third the FPS case. Note that only the FPS case shows the occurrence of a substorm onset. See text for more details. Figure from *Oliveira and Raeder* [2014].

Figure 4-3 shows the diffusive auroral e^- precipitation energy flux (DAPEF) in the time steps of 5 minutes from t = 25:00 minutes. In the IOS-1 and IOS-2 cases the DAPEF remained almost unaffected by the shock impact. In all cases, auroral precipitation is enhanced in the night side ionosphere approximately 12 minutes after shock impact. In the IOS cases, the shocks hit the magnetosphere behind the cusp, leading to a mild auroral precipitation at t = 35:00. However, at the same instant, the FPS enhances more auroral activity in the ionosphere nightside because the FPS impacts the magnetosphere behind the cusp, and thus the cusp is neither displaced nor compressed. In the FPS case, the shock hits the magnetosphere first at the nose, leading to a compression of the magnetosphere and the cusp, and to a pole-ward displacement of the cusp.

Later precipitation changes all occur in the nightside. As already shown by the FACs, these changes are mostly related to substorm activity. In the FPS case, auroral substorm onset is formed in the ionosphere nightside at $70^o < \lambda_m < 65^o$ between 0300 MLT and 0600 MLT. Such auroral activity is not found in any IOS case.

In order to perform a quantitative comparison we integrate the ionosphere quantities over the northern hemisphere polar cap. To separate the directly driven response, which occurs mostly in the dayside, from the induced substorm response, which affects mostly the nightside, we integrate the FACs separately for the dayside and the nightside.

Figure 4-4 shows the time series of the integrated FACs, in MA, over the northern hemisphere ionosphere on both dayside (a) and nightside (b), for the three cases. In both panels, the blue lines indicate the IOS-1 case, the green lines indicate the IOS-2 case, and the red lines indicate the FPS case. The first vertical dashed line indicates the instance at which the IP shock hits the bow shock in the IOS-1 and IOS-2 cases, and the second vertical dashed line indicates that instance for the FPS case. The plotted quantity is the magnitude of the FAC, which is primarily the Region I current. As expected, the IP impact enhances the FACs on the dayside. Before the shock impact, the FACs on the dayside have nearly the same magnitude, 0.29 MA, and were in a quasi-steady state. In all cases, the dayside FAC magnitude begins to rise approximately 6 minutes after the shock impact. The FACs increase nearly linearly over a period of approximately 4 minutes, which corresponds roughly to the time it takes for the shock to pass over the dayside magnetosphere. This initial rise is nearly identical for all cases. Later, in the two IOS cases, the FAC remains by and large steady at around 0.5 MA for the IOS case, but continues to rise for another 20 minutes in the FPS case.

Figure 4-2 shows that the initial rise is in all cases due to enhanced FACs in the vicinity of the cusp. However, in the IOS-1 and IOS-2 cases the enhancement is mostly in the nightside of the cusp, whereas in the FPS case FACs both on the dayside and the nightside of the cusp are enhanced. It seems that the more thorough compression of the dayside magnetosphere leads to the stronger and more long lasting FAC enhancement in the FPS case, although that is not directly apparent in Figure 4-2.

The nightside current enhancements (Figure 4-4(b)) begin about 2 minutes after the dayside enhancements, in the three cases. For all shocks, the enhancements are qualitatively different from those on the dayside. In all cases, strong ULF waves are excited, with a period of 4-5 minutes. In the two IOS cases, the average FAC is enhanced from ∼2 MA to ∼3 MA due to the shock impact, with superimposed waves with an amplitude of the order of ∼0.2-0.3 MA. In the IOS-2 case, 17-18 minutes after the shock impact, the ULF wave amplitude rises to ∼0.75 MA. In the FPS case, the increase of the average FAC is similar, but the wave amplitude is much larger, i.e., of the order of ∼1-2 MA. These large oscillations persist for at least 60 minutes. While much of the response is similar to what *Guo et al.* [2005] found in their simulations, the oscillations are new. It is at present not clear what these oscillations correspond to in the magnetosphere, but they are likely cavity modes [*Samson*

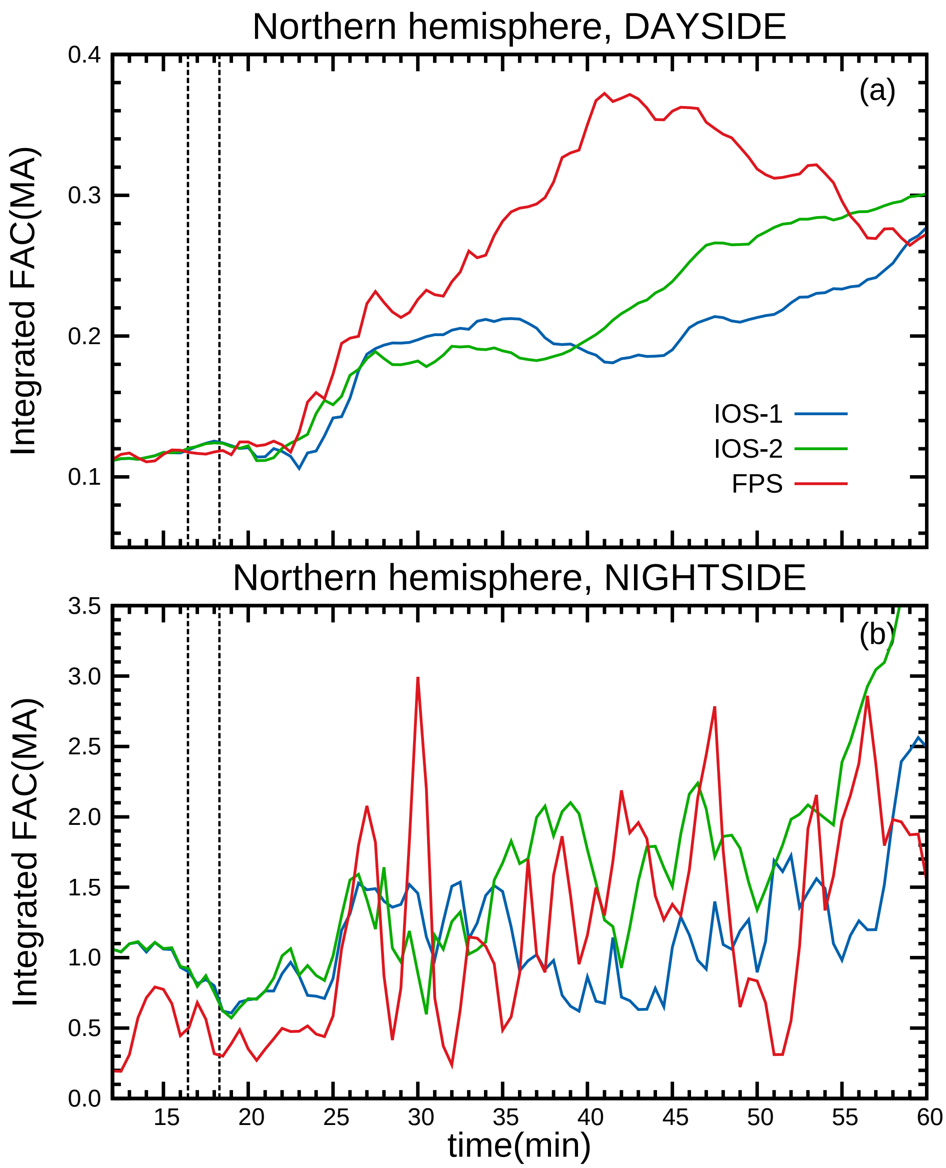

Figure 4-4: Total field-aligned currents (FACs, in MA) integrated in the northern hemisphere ionosphere. The top panel (a) shows the time evolution of the integrated FACs in the dayside ionosphere. The bottom panel (b) represents the integrated FACs in the nightside ionosphere. In both plots, the first dashed vertical line at t=16:45 min indicates the instant of impact of the IOS-1 and IOS-2. The second dashed vertical line, at t=18:28 min, indicates the instant of impact of the FPS. Figure from *Oliveira and Raeder* [2014].

et al., 1992].

Figure 4-5 shows the cross polar cap potential (CPCP) and the integrated precipitation energy DAPEF in panels (a) and (b), respectively. DAPEF is calculated as the thermal energy flux of plasma sheet electrons assuming perfect pitch angle scattering, and a full loss cone [see *Raeder et al.*, 1998; *Raeder*, 2003, for details]. The blue line represents the IOS-1 case, the green line represents the IOS-2 case, and the red line represents the FPS case. Vertical, dashed lines, as described above, indicate the shock impact times for all cases. Before the shock impact, the system oscillated noticeably in an amplitude less than 5 kV in both cases. After the impact, the IOS-1 and IOS-2 induced a very similar potential jump from roughly 35 kV to a peak of approximately 55-60 kV. The CPCP oscillated with a period of nearly 5 minutes until it reached the near steady state value of 25 kV after 42 minutes.

The FPS case is more dynamic. The system oscillated around 30 kV before the shock impact. Right two minutes after the FPS hit the bow shock, the potential difference dropped to 23 kV. This effect was also seen by *Guo et al.* [2005] and interpreted as the redistribution of the FACs after the shock penetrates the magnetosphere. The potential drop then reached two smaller peaks, 50 kV at t=22:00 minutes, and 62 kV at t=24:00 minutes until it reached the maximum of 82 kV at t=27:00 minutes. The potential still reached two peaks of 53 kV at t=30:00 minutes and t=33:00 minutes. Then, the potential difference decreased in a period of nearly 7 minutes. After close to t=33:00 minutes, both systems evolved to nearly the same final quasi-steady state. This similarity has been shown by *Guo et al.* [2005] but not with this oscillatory behavior.

The bottom panel (b) of Figure 4-5 shows the time series for the integrated DAPEF, in units of GW. Again, the blue line represents the IOS-1 case, the green line represents the IOS-2 case, and the red line represents the FPS case. Before the shock impact the

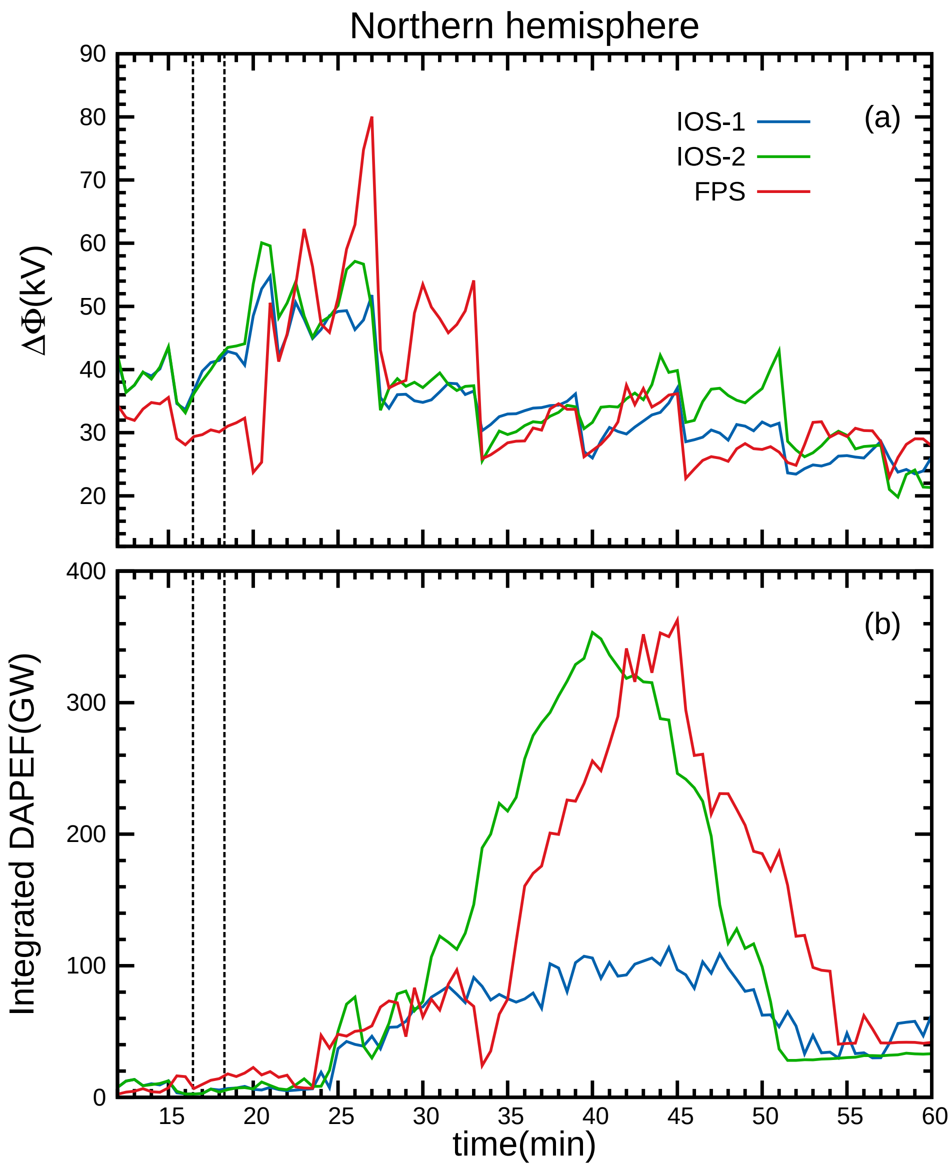

Figure 4-5: (a) Cross polar cap potential (CPCP, in kV) in the northern hemisphere ionosphere. (b) Integrated auroral electron precipitation energy flux (DAPEF, in GW) in the same hemisphere. The dashed vertical lines are the same as in Figure refintegratedFAC. Figure from *Oliveira and Raeder* [2014].

ionosphere is in a quiet state with low auroral activity. After the shock hit the bow shock, between t=24:00 minutes and t=33:00 minutes, the three systems evolved quite similarly, while the auroral energy flux suffered a small drop in the FPS case at t=34:00 minutes. In the IOS cases, the DAPEF attains a maximum value of barely 100-120 GW near t=44:00 minutes, and then evolves to a final state of ~20-50 GW. On the other hand, the FPS enhanced the DAPEF much more, and briefly reaches a maximum of ~350 GW at t=45:00 minutes.

By comparing the two shocks with the same Mach number, namely IOS-1 and FPS, we observe that both shocks lead to very different geomagnetic responses. Also, the IOS-2 geomagnetic response is smaller in comparison to the FPS geomagnetic response, even though the inclined shock was twice stronger than the head-on shock. We attribute these results to the different shock normal orientations. Comparison with Figure 4-3 shows that this enhanced precipitation flux must be from the nightside due to substorm activity. Such precipitation enhancements have been reported earlier by *Zhou and Tsurutani* [2001], *Tsurutani and Zhou* [2003], and *Yue et al.* [2010], who find that the auroral precipitation and field-aligned currents in the nightside can be intensified after a FFS impact, because it triggers the release of stored magnetospheric/magnetotail energy in the form of particularly large substorms, or even supersubstorms [See *Tsurutani and Lakhina*, 2014, for more references therein]. Such substorm triggering might be a result of the decreasing in the nightside B_Z, as simulated and observed at geosynchronous orbit by *Sun et al.* [2011, 2012, 2014]. In that case, the decrease in the nightside B_Z is suggested as a result of Earth-ward transportation of magnetic flux by temporarily enhanced plasma flows at the nightside geosynchronous orbit after the impingement of an IP shock. In our case, the symmetric plasma transport leads to a more intense geomagnetic activity. Although our simulations do not represent a storm and although the simulation results may be qualitatively in error, they match qualitatively the observed shock impact behavior.

4.3 Summary and Conclusions

It has been known for a long time that IP shocks can have a profound impact on the magnetosphere; however, it is much less known which factors determine the geoeffectiveness of IP shocks. There have been a few studies in the past addressing the effect of shock geometry [*Takeuchi et al.*, 2002; *Jurac et al.*, 2002; *Guo et al.*, 2005; *Wang et al.*, 2005, 2006; *Grib and Pushkar*, 2006; *Samsonov*, 2011], but none have considered the particular geometry that we investigated here. Specifically, here we use global simulations to contrast two different scenarios. In one scenario, the IP shock normal lies along the Sun-Earth line, such that there is a frontal impact on the magnetosphere. In the other scenario, the IP shock is inclined with respect to the Sun-Earth line. In either case, the shock normal lies in the GSE XZ plane, and the IMF is southward, such that there is no y-dependence of any solar wind parameter. The two scenarios lead to very different responses of the magnetosphere:

1. In the frontal case, the shock launches waves symmetrically into the magnetosphere, which converge on the tail plasma sheet and compress it. By contrast, in the inclined cases, the waves reach the plasma sheet at different times, causing much less compression, but a north-south displacement of the plasma sheet. This result holds even for shocks with larger Mach numbers.

2. In the frontal case, the compression triggers a substorm, whereas in the inclined cases there is no excess geomagnetic activity beyond what would be expected for southward IMF.

3. In all cases the shock impact enhances FACs in the dayside with a similar quantitative response. However, in the inclined cases the FAC enhancement occurs mainly behind

the cusp, whereas in the frontal case the cusp is displaced while the FACs increase over a wider MLT range. In the frontal case, the dayside FAC response also persists longer and is more intense, i.e., a ∼200% enhancement versus a ∼100% enhancement in the inclined case.

4. The nightside FAC response is qualitatively similar in the three cases and shows the development of ULF waves. However, in the frontal case the ULF wave amplitude is much stronger. The detailed excitation mechanism remains to be investigated.

5. The response of the cross polar cap potential is relatively benign and limited to the first 15 minutes after the impact, in all cases. The three cases relax to the pre-impact state in less than 20 minutes.

6. In all cases diffuse auroral electron precipitation increases in similar fashion in direct response to the shock impact. In the frontal case, this is followed by a delayed response ∼10 minutes later, which peaks ∼20 minutes after the impact, and which comes from the nightside. The latter is interpreted as a consequence of the substorm triggered by the shock impact.

Our results show that the shock impact angle has a major effect on the geoeffectiveness of the shock, even more than the Mach number or some other measure of the shock strength. Although we only covered a relatively small parameter space in terms of impact angles, shock strength, and IMF orientation, the qualitative and quantitative differences we found are significant. With respect to substorm triggering [*Kokubun et al.*, 1977; *Lyons*, 1995, 1996; *Lui et al.*, 1990], the differences we found in the inclined and frontal cases are of particular importance. Apparently, the same type of IP shock can either trigger a substorm or not, depending on the shock normal direction, which has not been considered in previous studies. We also find large amplitude waves in the FACs that are apparently caused by the shock impacts. Given their period, these waves are likely cavity modes [*Samson et al.*, 1992; *Hughes*, 1994]. We find that the modes have significantly larger amplitude for the frontal case. This is likely due to the fact that the waves that converge on the tail and compress the plasma sheet from there launch a wave back towards the nightside magnetosphere, which in turn excites the cavity mode. In the inclined cases, this earthward wave is likely much weaker, and thus excites a weaker cavity mode. We will study the wave excitation in more detail in a forthcoming paper. Other future work is also clearly laid out, namely finding the correlation between geomagnetic activity and IP shock normal orientation in data, and a better parameter space coverage with simulations.

Chapter 5

The SuperMAG collaboration

5.1 The official IAGA geomagnetic indices

The understanding of determined geomagnetic activities depends on the choice of the most convenient geomagnetic index [*Rostoker*, 1972]. For example, the logarithmic index Kp introduced by *Bartels* [1949] (and its linear counterpart Ap) is a good indicator of geomagnetic activity in regions of middle geomagnetic latitudes whose contributions come from the auroral electrojets and the ring current. If one is interested in measuring disturbances in the ring current, the Dst index, introduced by *Sugiura* [1964], is the right choice. The Dst index was accepted after the International Geophysical Year in 1964. However, straightforward indices to quantify auroral zone activity coming from auroral electrojects were only later suggested by *Davis and Sugiura* [1966]. Details about time resolution, geomagnetic stations and the historical development of most geomagnetic indices were reviewed elsewhere [*Rostoker*, 1972; *Mayaud*, 1980; *Ahn et al.*, 2000].

It is well established by the community that substorm activity may be triggered by IP shock impacts [*Burch*, 1972; *Kokubun et al.*, 1977; *Akasofu and Chao*, 1980; *Lui et al.*, 1990; *Zhou and Tsurutani*, 2001; *Tsurutani and Zhou*, 2003; *Yue et al.*, 2010; *Echer et al.*, 2011; *Tsurutani et al.*, 2014; *Oliveira and Raeder*, 2014], and that AL appears to be the best index to quantify the strength of auroral activity. The AE index, the auroral electroject index, was first suggested by *Davis and Sugiura* [1966] and has been heavily used by magnetospheric physicists since then. The initial number of geomagnetic stations was 7, and in the following years this number was increased to 12 [see, e.g., *Rostoker*, 1972, for more details]. The current 12 official IAGA (International Association of Geomagnetism and Aeronomy) stations are represented in Figure 5-1 from *Newell and Gjerloev* [2011a]. However, as pointed out by *Davis and Sugiura* [1966] themselves and reviewed by *Rostoker* [1972], the indices AU, AL, and AE = AU - AL, available at the World Data Center (WDC) in Kyoto, Japan, website (`http://wdc.kugi.kyoto-u.ac.jp/aeasy/index.html`), are limited because of the relatively low number of ground stations used to compute these indices. Years later, *Kamide et al.* [1982] used 70 magnetometer stations to derive the AE index. However, they did not report quantitative results of their analyses. More surprisingly, *Kamide* [2005] even suggested the community to stop deriving and using the AE index because of its non-sense physical meaning for auroral electroject descriptions.

5.2 The enhanced SuperMAG indices

Since the beginning of the study of magnetospheric events it is clear that sometimes strong auroral events are underestimated because there are no ground stations under the auroral bulge contributing to the construction of these indices during some strong auroral substorm events [*Gjerloev et al.*, 2004]. As an alternative to alleviate this deficiency, SuperMAG, a large worldwide collaboration involving more than 300 ground-based magnetometers, was formed [*Gjerloev*, 2009]. The locations of this large number of geomagnetic stations spread all over the world is shown in Figure 5-3, published by *Gjerloev* [2012]. Table 5.1 shows the current chain of magnetometers with their PI's/organizations contributing to the SuperMAG initiative (`http://supermag.jhuapl.edu/info/?page=acknowledgement`). Nevertheless, because the AU, AL, and AE indices are recognized as official indices by IAGA,

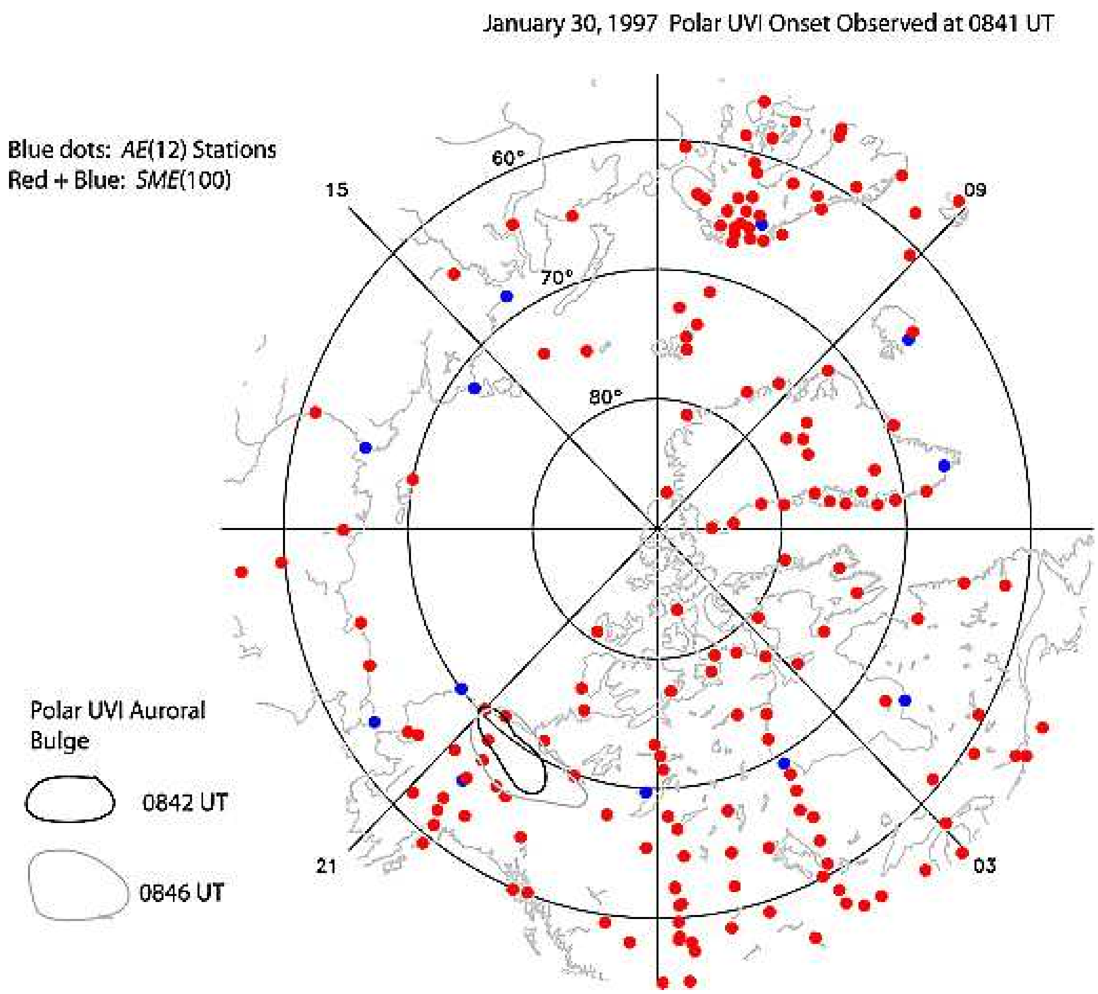

Figure 5-1: The northern hemispheric AE (blue dots) and SME (red dots) station distribution in the northern hemisphere. As discussed by *Newell and Gjerloev* [2011a], a sharp increase in the AL index was measured by the SME stations, but was not detected by the AE stations. There were no AE stations under the auroral bulge for that event. This figure was taken from *Newell and Gjerloev* [2011a].

SuperMAG defines SMU as the SuperMAG measurement of the maximum eastward auroral electrojet strength (upper envelope of N-component measured by stations between 40^o and 80^o magnetic north), SML as the SuperMAG measurement of the minimum westward auroral electrojet strength (lower envelope of N-component measured by stations between 40^o and 80^o magnetic north), and SME = SMU - SML as the SuperMAG measurement of the auroral electroject index defined as the distance between the last two indices [*Newell and Gjerloev*, 2011a,b].

An example of an auroral substorm event observed by different numbers of IAGA and SuperMAG stations is represented by Figure 5-1 extracted from *Newell and Gjerloev* [2011a]. In their event, it is shown by Polar UVI imagery that the expansion of the auroral bulge traveled over no AE ground stations, but instead passed over almost ten of the SME ground stations. This auroral substorm was underestimated by the AE stations, as shown by Figure 5-2 from *Newell and Gjerloev* [2011a]. Polar UVI images identified an auroral onset on 30 January 1997 at 0841 UT. The AL stations did not detect this substorm event; however, the SML stations recorded a substorm onset 37 seconds after the onset registered by Polar UVI observations. Therefore it is important to mention that AE and SME, besides the other SuperMAG indices, are primarily of the same nature, but with the SuperMAG indices being enhanced by the higher number of ground based stations used to build the SuperMAG indices. More details about the SuperMAG initiative can be found in *Gjerloev* [2009]; *Newell and Gjerloev* [2011a,b], and an explanation about data techniques and assimilation is reported by *Gjerloev* [2012]. Finally, the data are available from the SuperMAG websites `http://supermag.jhuapl.edu/` and `http://supermag.uib.no/`.

A schematic representation of the SuperMAG data flow is represented by Figure 5-4, taken from *Gjerloev* [2012]. The initial step in this process is accomplished, as quoting Jesper Gjerloev, by "ingesting" the data coming from the SuperMAG collaborators cor-

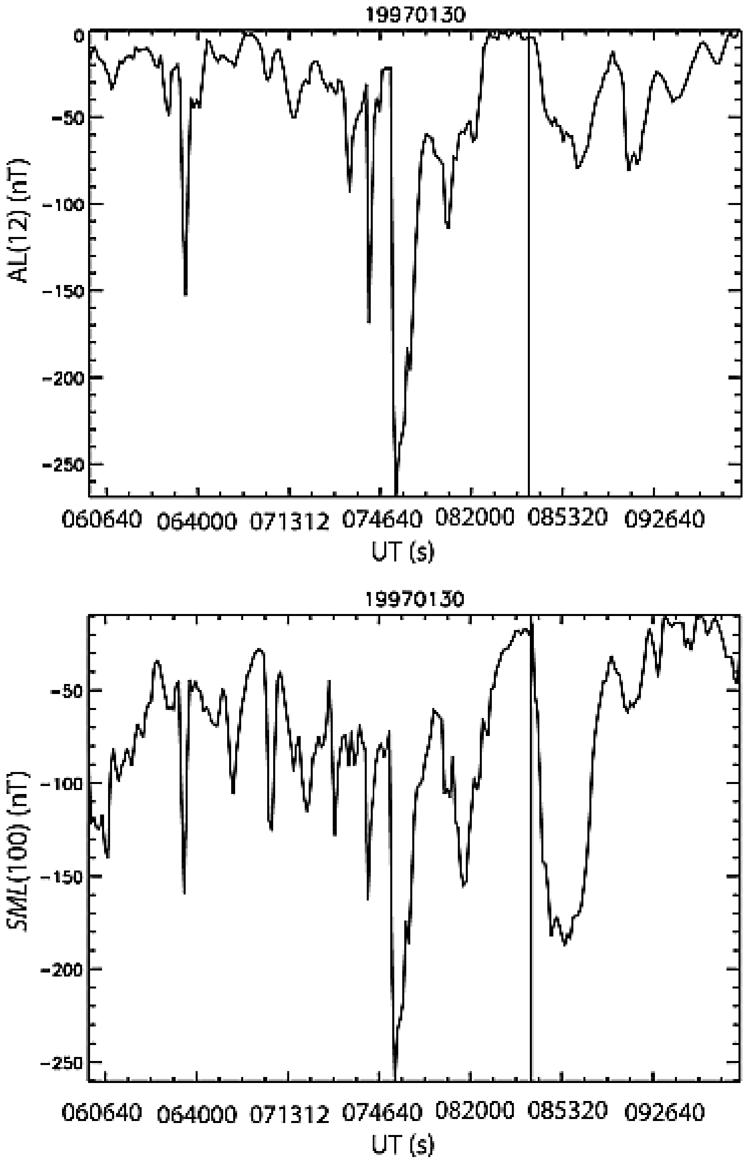

Figure 5-2: Auroral substorm event observed by IAGA and SuperMAG stations on 30 January 1997. Polar UVI images identified an auroral substorm onset at 0841 UT. AL did not detect this onset, but SML did 37 seconds after the onset determined by Polar UVI images. Figure from *Newell and Gjerloev* [2011a].

Table 5.1: The SuperMAG project collaborators as seen at the SuperMAG website `http://supermag.jhuapl.edu`.

Magnetometer chain	PI/SuperMAG collaborator[a]
Intermagnet	USGS, Jeffrey J. Love
CARISMA	Ian Mann
CANMOS	D. Boteler
The S-RAMP Database	K. Yumoto and Dr. K. Shiokawa
The SPIDR database	NOAA/NGDC
AARI	Oleg Troshichev
The MACCS program	M. Engebretson, GUGSC[b]
GIMA MEASURE	UCLA IGPP and Florida Institute of Technology
SAMBA	Eftyhia Zesta
210 Chain	K. Yumoto
SAMNET	Farideh Honary
IMAGE magnetometer array maintenance	Eija Tanskanen
PENGUIN/AUTUMN	Martin Conners
DTU Space	Dr. Jürgen Matzka
South Pole and McMurdo Magnetometer	L. J. Lanzarotti and A. T. Weatherwax
ICESTAR/RAPIDMAG/PENGUIn	British Artarctic Survey
McMac	Dr. Peter Chi
BGS	Dr. Susan Macmillan
IZMIRAN/GFZ	Dr. Jrgen Matzka
MFGI	B. Heilig
IGFPAS	J. Reda
University of LAquila	M. Vellante
SuperMAG	Jesper W. Gjerloev

[a] This list of collaborators may change as new magnetometer chains join the SuperMAG team.
[b] Geomagnetism Unit of the Geological Survey of Canada.

responding to more than 15,000 years of data [*Gjerloev*, 2012]. In this step, the system accepts data with all sorts of time resolution, formats, coordinate systems, and baselines. The second step defines a baseline and sets the data to a time resolution of 1 minute. The data format starts to be uniform. After some cleaning up and error clarifications, the data is rotated to a new local magnetic coordinate system, defined as NEZ by *Gjerloev* [2012]: N is the component pointing to the magnetic north, E is the component pointing to the magnetic east, and Z is the perpendicular component pointing down. Finally, in the final step, the data are now defined in the NEZ coordinate system and do not have any baselines. The data are ready to become available to the public at the SuperMAG website.

The SuperMAG data technique is well detailed by *Gjerloev* [2012]. This paper is a key to understanding all issues related to the SuperMAG data (J. W. Gjerloev, private communication, 2015). For more details, we refer Gjerloev's paper.

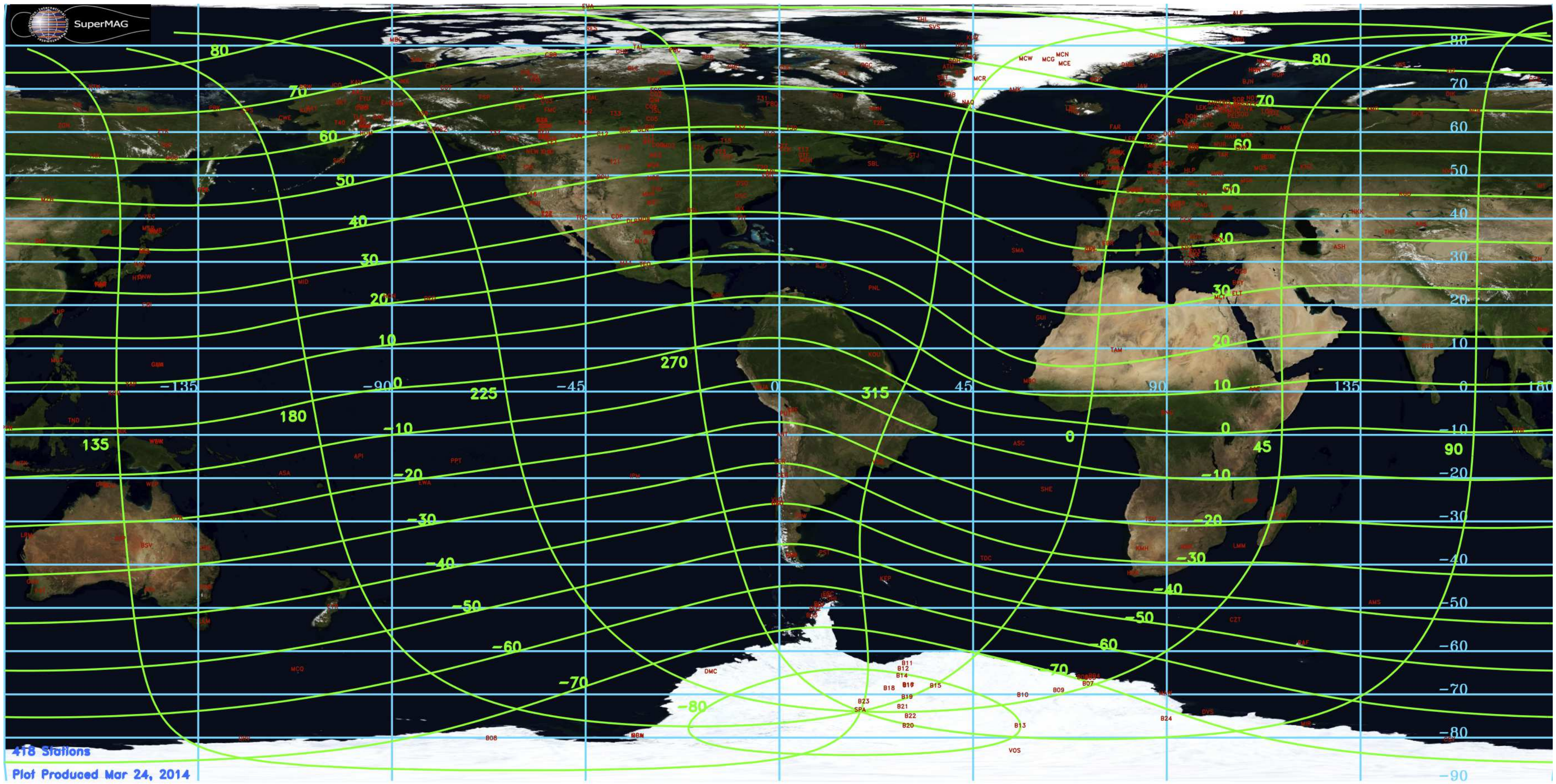

Figure 5-3: Locations of SuperMAG ground stations (red dots) in geomagnetic coordinates (blue) and geographic coordinates (green) after *Gjerloev* [2012].

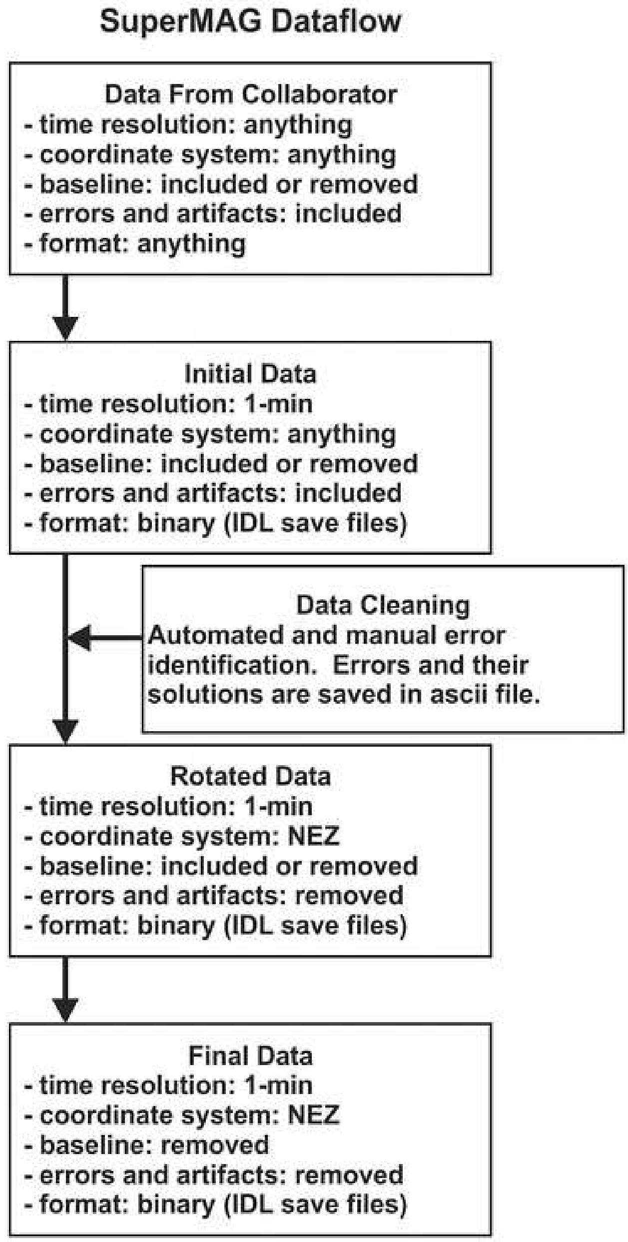

Figure 5-4: Representation of the SuperMAG data flow and assimilation into the SuperMAG system [*Gjerloev*, 2012].

Chapter 6

Statistics of interplanetary shock impact angles and their geoeffectiveness

6.1 Introduction

This chapter is a version of two papers submitted to the *Journal of Geophysical Research* [*Oliveira and Raeder*, 2015] and *Journal of Atmospheric and Solar-Terrestrial Physics* [*Oliveira et al.*, 2015] by Professor Raeder and I corresponding to the results obtained in my doctoral research. We used solar wind and IMF data in a time period of about 20 years, covering approximately one solar cycle and a half, to build a list with 461 fast forward interplanetary (IP) shocks. We find that the yearly number of IP shocks is well correlated with the monthly sunspot number. Our data base shows that the interplanetary space is dominated by weak IP shocks at 1 AU. We study correlations of IP shock strength (here indicated by shock speed) with shock impact angle θ_{x_n} with SML strength and AP (auroral power) intensity. The former indicates the strength of substorms, and the latter was obtained from the SuperMAG SME index. In general, we find that fast (high speed) almost frontal shocks are more geoeffective than slow (low speed) inclined shocks.

6.2 Data and methodology

6.2.1 Data

In our study, we investigate solar wind properties at 1 AU to find fast forward IP shock events. In order to do so, we use two different spacecraft close to the equatorial plane: WIND, with data from 1995 up to 2013, and ACE (Advanced Composition Explorer), with data from 1998 also up to 2013. The WIND data were obtained from the Solar Wind Experiment (SWE) instrument [*Ogilvie et al.*, 1995], and the Magnetic Field Investigation (MFI) instrument [*Lepping et al.*, 1995], both in 93-second time resolution. The ACE data were obtained from the Solar Wind Electron Proton Alpha Monitor (SWEPAM) instrument [*McComas et al.*, 1998] and the ACE Magnetic Field Experiment (MAG) instrument [*Smith et al.*, 1998], both with 64-second time resolution. All data were downloaded from the CDAWeb interface located at `http://cdaweb.gsfc.nasa.gov`. All these data were used to compile an extensive list of 461 IP shock events that can be found in Table A1 in the Appendix.

The monthly averaged sunspot number (SSN) data were compiled by the Solar Influence Data Analysis Center (SIDC). This list can be downloaded from `http://sidc.oma.be/silso/datafiles`.

The geomagnetic activity is inferred from the enhanced SuperMAG geomagnetic data. Particularly, we used the SME and SML indices, enhanced versions of the traditional AE and AL indices. More details about the SuperMAG collaboration and data can be found in Chapter 5 of this dissertation or in *Gjerloev* [2009]; *Newell and Gjerloev* [2011a,b]; *Gjerloev* [2012].

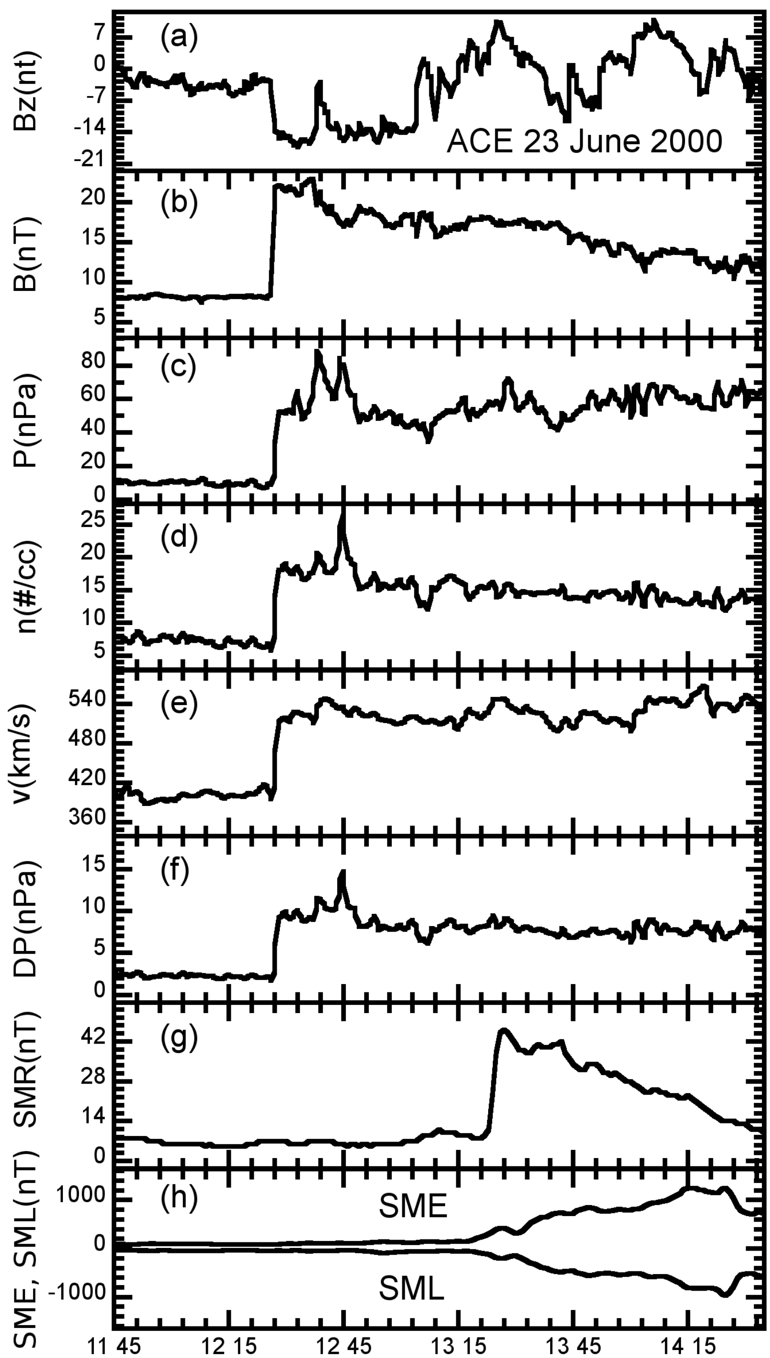

Figure 6-1: An example of the methodology used for shock normal calculation and geomagnetic activity analysis, as seen by ACE on 23 June 2000. Plots (a)-(f) show jumps in B_z and total magnetic field, in nT; thermal plasma pressure, in pPa; particle number density, in cm^{-3}; shock speed, in km/s; and dynamic pressure DP (ρv^2). Plots (g) and (h) show SuperMAG data for the symmetric ring current SMR, similar to SYM-H, SME, and SML. The maximum geomagnetic activity was recorded for both SME and SML approximately 2 hours after the shock impact. The time interval used to identify geomagnetic activity for all IP shocks was from ∼30 minutes to 2 hours after shock impacts. Figure from *Oliveira and Raeder* [2015].

6.2.2 Determination of shock parameters and event analyses

IP shocks during the period investigated here have been cataloged by several sources, such as the Havard-Smithsonian Center for Astrophysics (CfA) IP shock list compiled by Dr. J. C. Kasper located at `http://www.cfa.harvard.edu/shocks/wi_data/` for WIND data, and `http://www.cfa.harvard.edu/shocks/ac_master_data/` for ACE data. We also used a shock list compiled by the ACE team available at `http://www-ssg.sr.unh.edu/mag/ace/ACElists/obs_list.html#shocks`. Another source used was the shock list with only ACE data from February 1998 to August 2008 published by *Wang et al.* [2010]. All these lists were merged to compile the shock list used here. We also used an automated search program to detect IP shock candidates in the raw data. After the shock was visually inspected, and if it satisfied the Rankine-Hugoniot conditions, the event was included in our list. Other sources were also consulted for comparison among several events in terms of solar wind conditions and IP shock parameters, such as calculated IP shock normal angles and speeds, when available [*Berdichevsky et al.*, 2000; *Russell et al.*, 2000; *Zhou and Tsurutani*, 2001; *Přech et al.*, 2008; *Wang et al.*, 2009; *Richardson and Cane*, 2010; *Koval and Szabo*, 2010; *Zhang et al.*, 2012; *Grygorov et al.*, 2014].

Once a shock was identified, solar wind data from WIND and ACE were inspected to provide the basis for IP shock parameter calculations. It is well known that IP shock normal calculations are very sensitive to upstream and downstream plasma parameters. Then, the highest quality available spacecraft data were chosen for shock parameter determinations as described below. In our IP shock list, from a total of 461 identified fast forward IP shocks, 272 were observed by ACE (59%), and 189 were observed by WIND (41%).

There have been a variety of shock normal determination methods suggested since late 1960s. Some of the most known methods using single spacecraft data are the magnetic and velocity coplanarity [*Colburn and Sonett*, 1966], and the mixed IMF and plasma data

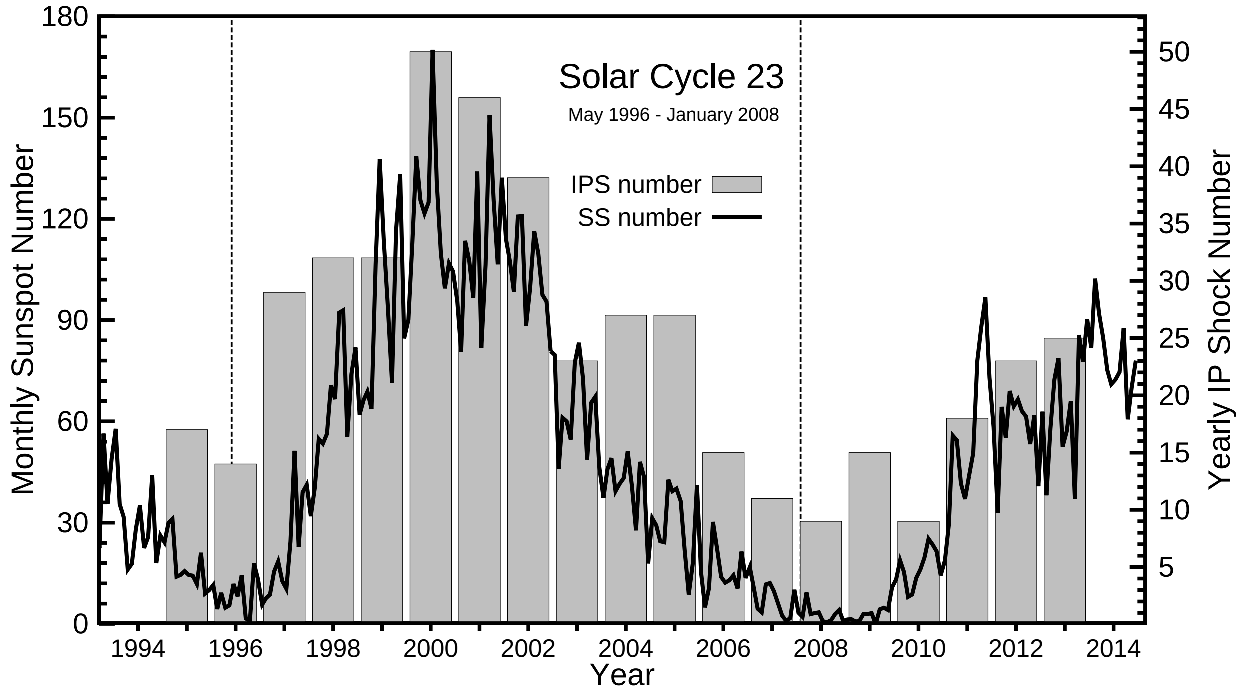

Figure 6-2: Yearly IP shock number (gray bars) plotted against the SIDC monthly sunspot number (solid lines). WIND and ACE data were used to identify all IP shock events. A strong correlation can be seen. The maximum yearly IP shock number occurred in the year 2000 (50 events), in the solar maximum of the solar cycle 23. Due to the unusual low sunspot number in the maximum of the current solar cycle, only 25 events were observed in 2013, and not many more are expected to be identified in the 2014 WIND and ACE data and even for the 2015 data [*Smith et al.*, 2014]. Figure from *Oliveira and Raeder* [2015].

methods [*Abraham-Shrauner*, 1972; *Abraham-Shrauner and Yun*, 1976]. Although situations with more than one spacecraft data availability give more reliable results [*Burlaga et al.*, 1980; *Russell et al.*, 1983a,b; *Russell and Alexander*, 1984; *Thomsen*, 1988; *Russell et al.*, 2000; *Szabo*, 2005; *Koval and Szabo*, 2010], we use the methods based only on one spacecraft. Multiple spacecraft data usage would not be possible in a large statistical study as this study, because availability of more than one spacecraft data for shock normal determination is rare. The IP shock normals are then calculated using the methods of magnetic coplanarity (MC), velocity coplanarity (VC), and three mixed data methods (MX1,MX2,MX3) found in *Schwartz* [1998]. Then, the average of the at least three closest results is calculated and registered as the chosen IP shock normal for each event.

An example of an event analysis is shown in Figure 6-1. This shock event was seen by

ACE on 23 June 2000. At 1227 UT and (234, 36.6,-0.7)R_E GSE upstream of the Earth, ACE observed sharp jumps in magnetic field B_z component, total magnetic field, plasma thermal pressure, particle number density, plasma velocity, and dynamic pressure ρv^2 (Figure 6-1 (a)-(f)). Approximately 55 minutes later, the shock impacted the magnetopause, the magnetosphere was compressed by the shock and an SSC was detected by SuperMAG geomagnetic stations, as can be seen in Figure 6-1 (g) for the SuperMAG symmetric ring current index SMR [*Newell and Gjerloev*, 2012], the SuperMAG index similar to the well known SYM-H index. Increases in the SuperMAG indices SME and SML followed the IP shock approximately 1 hour after shock impact, reaching a maximum of about 1500 nT for SME and a minimum of about -1000 nT for SML. The maximum geomagnetic activity was recorded in a time lag of approximately 2 hours after shock impacts for all events. Although we observed geomagnetic activity three hours after shock impacts, we believe the time window of 2 hours is enough and increasing it would not change our results significantly. This choice is consistent with time lag results reported by *Bargatze et al.* [1985], who observed that geomagnetic activity response amplitudes occurred in a time lag of 20 minutes due to solar wind-magnetosphere coupling and in a time lag of 60 minutes due to the energy release in the magnetotail. In our cases, the energy release in the magnetotail was caused by the IP shock impacts and the peaks occurred almost always more than ∼30 minutes after the shock impact. The calculated shock normal of this event is (-0.785,0.153,-0.600), with θ_{x_n} ∼140^o, shock speed of 553.2 km/s, and fast magnetosonic Mach number 2.60. Using these results, and assuming the estimated position of the magnetopause previous to the shock impact as 10 R_E as suggested by *Zhou and Tsurutani* [1999], the calculated time travel is ∼55 minutes, in agreement with observations, which validates our method. To complete the shock property analysis, the compression ratio (the ratio of downstream to upstream plasma density) was 2.62, and the fast magnetosonic Mach number was 2.60.

6.3 Statistical results

6.3.1 Solar wind and shock parameters

Figure 6-2 shows the yearly IP shock number (gray bars) and the monthly sunspot number (SSN, solid lines) plotted in the time range from 1995 to 2013. This time period includes the whole solar cycle 23, which ranged from May 1996 to January 2008. Correlations between the number of SSCs and the SSN in different solar cycles have been reported by earlier works [*Chao and Lepping*, 1974; *Hundhaunsen*, 1979; *Smith*, 1983; *Smith et al.*, 1986; *Rastogi*, 1999]. Since most SSCs are associated with IP shocks [*Smith et al.*, 1986; *Wang et al.*, 2006], these arguments are considered to be very similar. In our analysis, a correlation between both numbers is clear. During the ascending phase of the solar cycle 23, the number of IP shocks increases with the SSN. Then, during the declining phase of the solar cycle 23, the number of IP shocks decreases with the SSN. *Jian et al.* [2006a] observed a higher number of CMEs in solar maximum in comparison to solar minimum (5 cases in 1996 and 35 cases in 2000). The CME rate was strongly correlated with solar activity. In the case of CIRs, *Jian et al.* [2006b] reported the occurrence of 17 events in 1996 and 18 events in 2000. They observed a small variation rate of CIR events with solar activity. Then, according to these results, the numbers of CIRs plus CMEs in 1996 and 2000 are respectively 22 and 53, which is consistent with the number of IP shocks registered in our list, 19 in 1996 and 50 in 2000. Such results indicate that IP shocks in solar minimum are more likely to be driven by CIRs, while IP shocks in solar maximum are more likely to be driven by CMEs. Due to the unusual low SSN of the current solar cycle maximum, barely more than 25 shocks are expected to be found in the WIND and ACE data for 2014 and even 2015 [*Smith et al.*, 2014].

A statistical analysis of solar wind and IP shock parameters is shown in Figure 6-3(a-f). Figure 6-3 (a) shows θ_{x_n}, the angle between the shock normal vector and the Sun-Earth line.

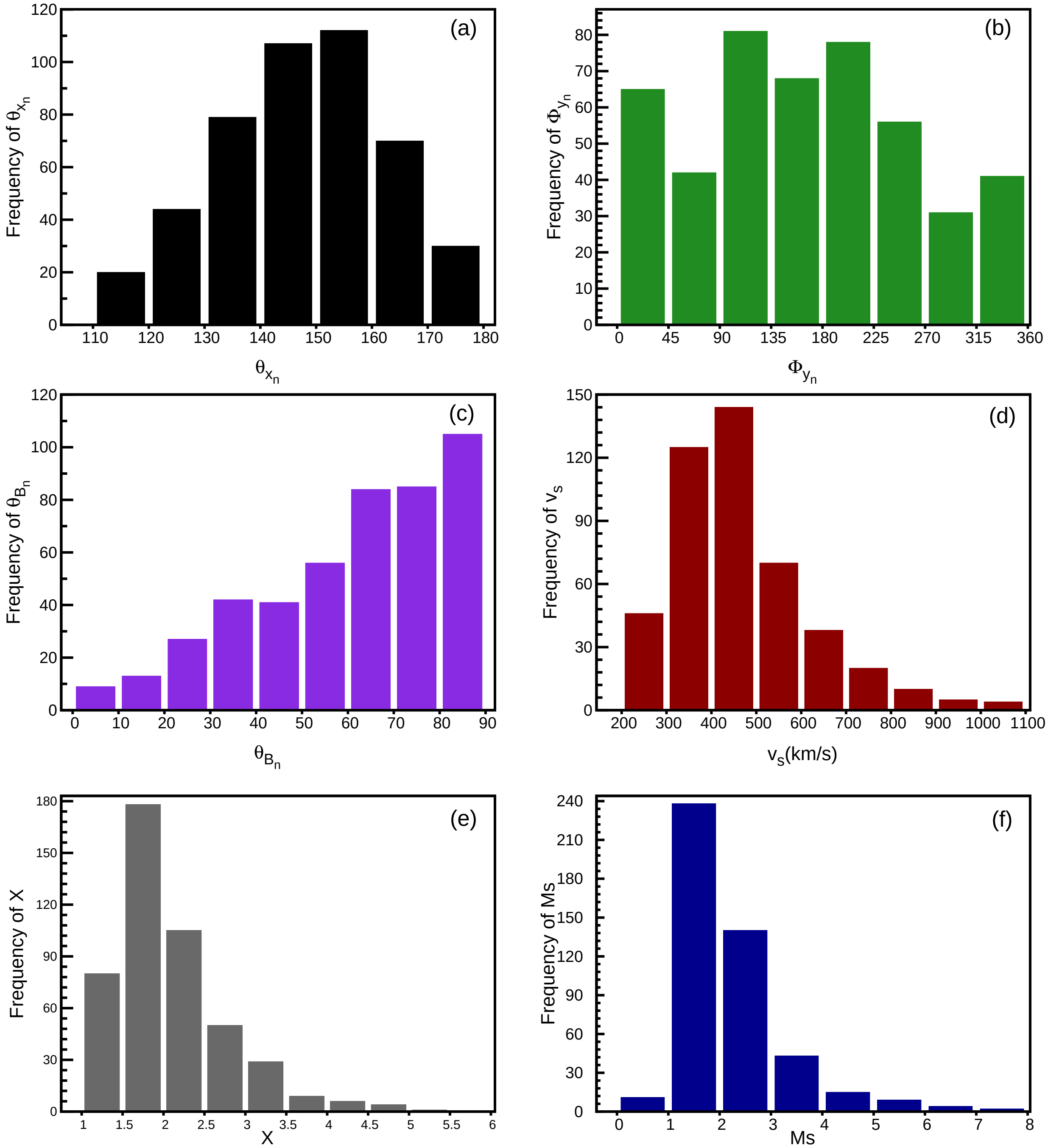

Figure 6-3: Statistical results of the full list with 461 IP shocks. Figure 3(a) shows the impact angle between the shock normal and the Sun-Earth line. Angles close to 180^o represent almost frontal shocks. The clock angles φ_{y_n} on the GSE YZ plane are shown in Figure 3(b). Angles close to 0^o and 180^o indicate that the shock normal lied close to the equatorial plane. Figure 3(c) shows the angle between the upstream magnetic field vector and the shock normal. v_s, represented in Figure 3(d), is the shock speed, in km/s, in relation to the spacecraft frame of reference. Figure 3(e) shows the compression ratio, the ratio of the downstream to upstream plasma densities. Finally, the fast magnetosonic Mach number Ms is shown by Figure 3(f). Figure from *Oliveira and Raeder* [2015].

Angles close to 180^o indicate IP shocks were almost frontal shocks, i.e., the shock normals lay in the Sun-Earth line pointing in the direction of the Sun. IP shocks with angles close to 90^o represent inclined shocks. In our list, 363 (78.57%) cases had shocks with $\theta_{x_n} \geq 135^o$. The distribution of the clock angle φ_{y_n} is shown in Figure 6-3(b). Shock normals with $0^o \leq \varphi_{y_n} \leq 45^o$, $135^o \leq \varphi_{y_n} \leq 225^o$, and $315^o \leq \varphi_{y_n} \leq 360^o$ indicate that the shock normal was close to the equatorial plane. These conditions were satisfied by 276 events, or 59.74%. Figure 6-3(c) shows the obliquity θ_{B_n}, the angle between the shock normal and the upstream magnetic field vector. In our data set, 354 cases showed θ_{B_n} larger than 45^o, and most of the shocks in this category might have been driven by ICMEs [*Richardson and Cane*, 2010]. The shock speed distribution is shown in Figure 6-3(d). The average shock speed is 467 km/s, and it tends to be higher in solar maximum, and lower in solar minimum, as already reported by *Berdichevsky et al.* [2000] and *Echer et al.* [2003] with data partially in the same time period. The percentage of shocks above the average speed is 40.13%, or 185 events. The compression ratio, the ratio of the downstream to upstream plasma densities, can be seen in Figure 6-3(e). As reported before [*Berdichevsky et al.*, 2000], most shocks have their compression ratios between 1.2 and 2.0, which happened to 251 of our cases (54.44%). Our compression ratio average is 2.07. Although the theoretical limit for the compression ratio is 4 [*Richter et al.*, 1985], which is derived for perpendicular shocks, this value was exceeded in 11 cases (2.38%), and most of them took place slightly before and after the solar maximum (year 2000). *Echer et al.* [2003] argued that such cases can happen for some shocks in a data set in which shock obliquities range from almost parallel to almost perpendicular shocks. Finally, the fast magnetosonic Mach number distribution is shown in Figure 6-3(f). The average of Ms is 2.15, and it is clear that most shocks have Ms between 1.0 and 3.0 [*Tsurutani and Lin*, 1985]. The number of shocks with Ms above the average is 166 (36.00%). However, some shocks have Ms less than one, which can be an indication that such events were not shocks because the shock waves could not steepen, even though they could show some shock-like behavior [*Kennel et al.*, 1985]. These events were not included in our statistical analysis. Therefore, as a consequence of this analysis, it is possible to conclude that the interplanetary space is dominated by weak IP shocks. The agreement of our results with other works validates our statistical analysis, in particular the shock normal determination methods used in this work.

6.3.2 Substorm strength

In this section we investigate the geoeffectiveness of IP shocks by correlating the shock parameters with the SuperMAG SML index as a geomagnetic activity indicator. Changes in this index, ΔSML, in nT, are recorded for each event from ~30 minutes to two hours after shock impact. If the IP shock is followed by any other solar wind structure, only the first peak in the data is considered. We chose this time frame because some inclined shocks take a long time to sweep over the magnetosphere when they are inclined in relation to the Sun-Earth line [*Takeuchi et al.*, 2002; *Guo et al.*, 2005; *Wang et al.*, 2005, 2006; *Samsonov*, 2011; *Oliveira and Raeder*, 2014]. We used SuperMAG data up to 2013 because the 2014 SuperMAG data were not yet available.

Figure 6-4 shows jumps in SML, in nT, measured by SuperMAG ground stations plotted against the shock speed, in km/s. Since we consider two parameters, shock speed and impact angle, all the data were binned in three different groups in terms of the shock normal impact angle θ_{x_n}. Here, the impact angle is held and the shock speed varies. Figure 6-4(a) shows highly inclined shocks: $120^o \leq \theta_{x_n} \leq 140^o$; Figure 6-4(b) represents moderately inclined shocks, $140^o < \theta_{x_n} \leq 160^o$; and almost frontal shocks, $160^o < \theta_{x_n} \leq 180^o$, can be found in Figure 6-4(c). In Figure 6-4(a), most shocks produce little geomagnetic activity (ΔSML $<$ 500 nT), and in such cases most shocks had $v_s < 450$ km/s. This is expected for weak and

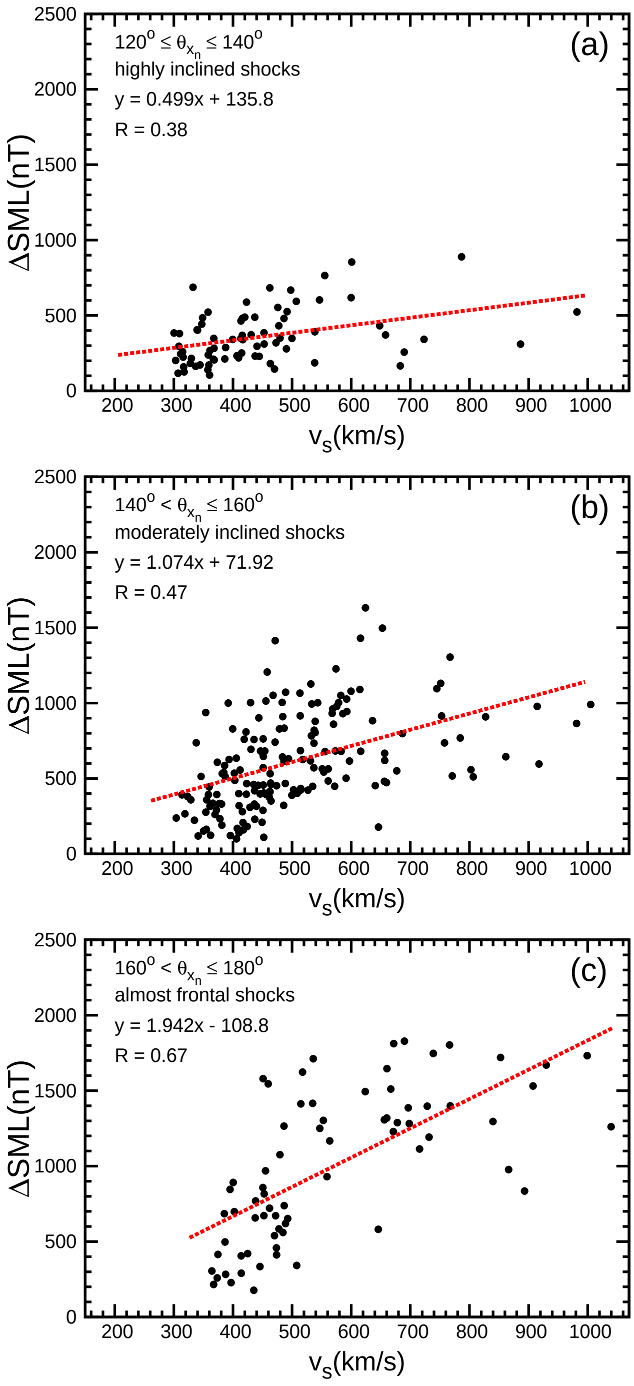

Figure 6-4: Jumps in SML triggered by IP shock impacts plotted as a function of the shock speed v_s. The events were binned in three different groups in terms of the shock orientation in relation to the X-line: Figure 4(a), $120^o \leq \theta_{x_n} \leq 140^o$ (highly inclined shocks), Figure 4(b), $140^o \leq \theta_{x_n} \leq 160^o$ (inclined shocks), and Figure 4(c) $160^o \leq \theta_{x_n} \leq 180^o$ (almost frontal shocks). The shocks are more geoeffective for strong (high speed) and almost frontal shocks. Figure from *Oliveira and Raeder* [2015].

highly inclined shocks. For some stronger, but highly inclined shocks, the resulting activity is slightly larger, but just a few such shocks in this case were identified in the data. The linear regression analysis gives a correlation coefficient of R = 0.38. In the intermediate case, i.e., the case of shocks with moderate inclination, most shocks produced ΔSML > 500 nT. In this case, there is a stronger correlation. We attribute the correlation coefficient of R = 0.47 to the fact that most shocks with v_s < 450 km/s triggered small jumps in SML (ΔSML < 500 nT). For the cases in which v_s > 450 km/s, ΔSML showed better correlations, but just a few with ΔSML > 1000 nT. In the more extreme case, namely the case in which the IP shocks were almost frontal, the correlation coefficient is R = 0.67. In this case, approximately half of the shocks with v_s < 450 km/s did not show large jumps in SML. Most shocks triggered ΔSML > 500 nT, and almost all cases in which ΔSML > 1000 nT had v_s larger than 450 km/s. Therefore, by inspecting all plots, it is clear that the IP shock geoeffectiveness increases with both shock strength and shock impact angle. Table 6.1 summarizes the results obtained in all categories in this case.

The opposite analysis is shown in Figure 6-5, i.e., the shock speed is held and the impact angle varies. There, ΔSML is plotted against θ_{x_n}, and the data are binned in three different categories related to the shock strength (or shock speed). Figure 5(a) shows the weak shocks, $300 \leq v_s \leq 450$ km/s; 6-5(b) moderate shocks, $450 < v_s \leq 550$ km/s; and 6-5(c) strong shocks, $v_s > 550$ km/s. Figure 6-5 (a) shows the largest number of small ΔSML (ΔSML < 500 nT), even for shocks with shock normals almost parallel to the Sun-Earth line. The correlation coefficient in this case is R = 0.37. A clearer ΔSML-θ_{x_n} correlation is evident in the intermediate case, where R = 0.48, and most shock events have ΔSML > 500 nT and $\theta_{x_n} > 135^o$. All shocks with ΔSML > 1000 nT had impact angles larger than 140^o. In the category of strong shocks, only a few shocks triggered geomagnetic activity with ΔSML < 500 nT, most of them being highly inclined shocks in which $\theta_{x_n} < 150^o$. Shocks with high

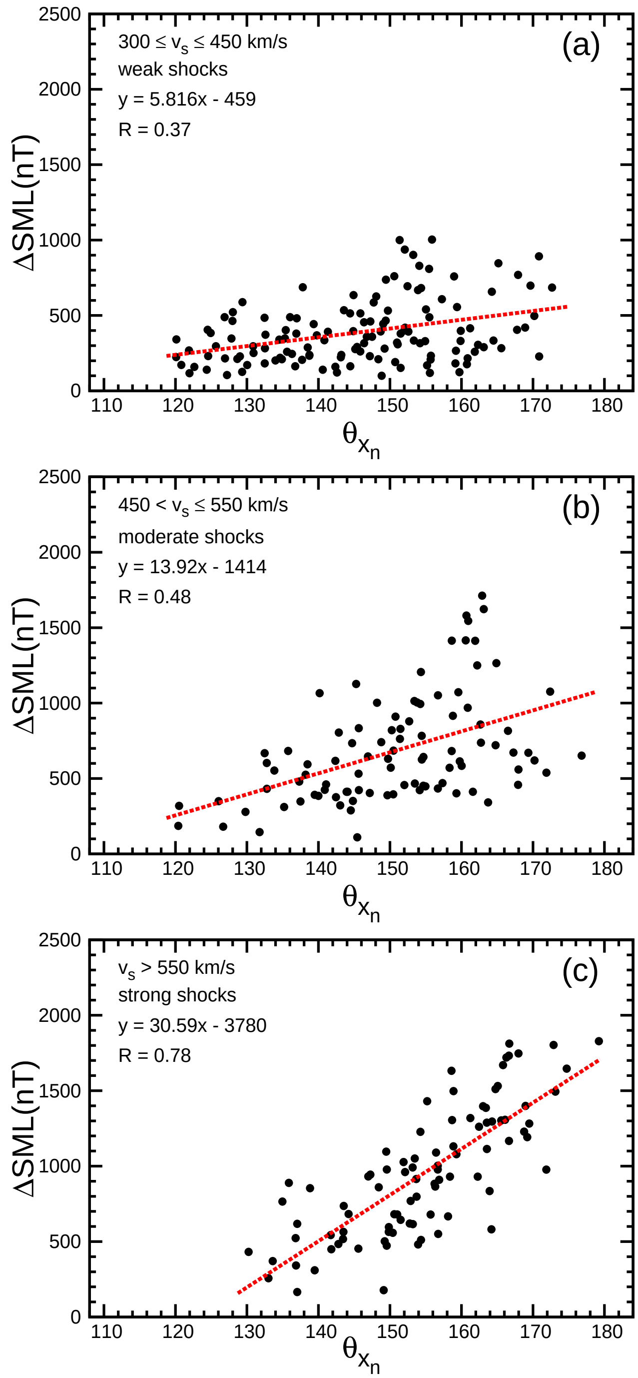

Figure 6-5: Jumps in SML triggered by IP shock impacts plotted as a function of the shock impact angle θ_{x_n}. The events were binned in three different groups in terms of the shock speed: Figure 5(a), $350 \leq v_s \leq 450$ km/s (weak shocks), Figure 5(b), $450 \leq v_s \leq 550$ km/s (moderate shocks), and Figure 5(c) $v_s \geq 550$ km/s (strong shocks). The shocks are more geoeffective for almost frontal and strong (high speed) shocks. Figure from *Oliveira and Raeder* [2015].

Fixed impact angle θ_{x_n}, changed shock speed v_s			
category	highly inclined	moderately inclined	almost frontal
R	0.38	0.47	0.67
Fixed shock speed v_s, changed impact angle θ_{x_n}			
category	weak	moderate	strong
R	0.37	0.48	0.78

Table 6.1: Summary of the results obtained for the shock speed, shock impact angle, and ΔSML correlation analyses. Table from *Oliveira and Raeder* [2015].

geoeffectiveness, or ΔSML > 1000 nT, were almost frontal shocks with $\theta_{x_n} > 150^o$ (only one event had θ_{x_n} slightly less than 150^o in this case). The highest correlation coefficient, R = 0.78, occurs for IP shocks in this category. Table 1 summarizes the results obtained in all cases in this correlation analysis.

Thus, strong shocks are generally much more geoeffective than weak shocks, and the geoeffectiveness increases if the IP shock impacts more frontally the Earth's magnetosphere. These results have already been shown by *Wang et al.* [2006] for the SSC rise-time and *Oliveira and Raeder* [2014] in global MHD simulations.

6.3.3 Auroral power intensity

We use the SuperMAG geomagnetic station data to identify auroral power associated with shock impingement. SuperMAG [*Gjerloev*, 2009] is an international collaboration with a chain of more than 300 ground stations used to compute the SME, SMU, and SML indices [*Newell and Gjerloev*, 2011a,b], the enhanced versions of AE, AU, and AL, respectively. The SuperMAG data were obtained from the websites `http://supermag.jhuapl.edu/` and `http://supermag.uib.no/`.

We used the SME index as a proxy for aurora power (AP) determinations. This choice was based on a relation found by *Newell and Gjerloev* [2011b]. *Newell and Gjerloev* [2011b] calibrated the SME index with both Polar UVI instantaneous images and DMSP instantaneous maps to obtain possible correlations between SME and AP. Due to time resolutions issues, the most relevant correlation found by them was between SME and AP as determined by Polar UVI. The linear relationship found by *Newell and Gjerloev* [2011b] and used here is:

$$AP = 0.048 \times SME + 0.241 \times (SME)^{1/2}\,, \tag{6.1}$$

where AP is represented in GW, and the square root portion comes from the monoenergetic auroral contribution. Here AP was integrated over the northern hemisphere polar cap between 1800-0600 magnetic local time and 60^o and 80^o magnetic latitude. More specifically, expression (6.1) indicates the nightside AP intensity as calculated from the SuperMAG SME index. Later, the SME index was confirmed to be the best choice to predict AP intensity instead of SMU and SML [*Newell and Gjerloev*, 2014].

In our statistical analysis we focus on sharp increases in the AP intensity resulting from the IP shock impacts with the Earth's magnetopause. The peak in the SME index is taken as a maximum in a sliding time ranging from approximately one half to two hours after shock impacts [see *Oliveira and Raeder*, 2015, for more details]. If there are more than one SME peak in the time interval, the first one is chosen as the maximum associated with the IP shock.

Correlations of variations in auroral power, ΔAP, in GW, with the shock speed v_s, in km/s, is shown in Figure 6-6. For this parameter selection, the impact angle θ_{x_n} is held constant while the shock speed is allowed to vary. The data are binned in three different categories: Figure 6-6(a), $120^o \leq \theta_{x_n} \leq 140^o$, highly inclined shocks; Figure 6-6 (b), $140^o < \theta_{x_n} \leq 160^o$, moderately inclined shocks; and Figure 6-6 (c), $160^o < \theta_{x_n} \leq 180^o$, almost frontal shocks. Here we consider events with low auroral activity when $\Delta\text{AP} < 20$ GW, and events with high auroral activity when $\Delta\text{AP} > 80$ GW. Events with moderate auroral activity are between these two limits. Figure 6-6 (a) shows that most events with low auroral

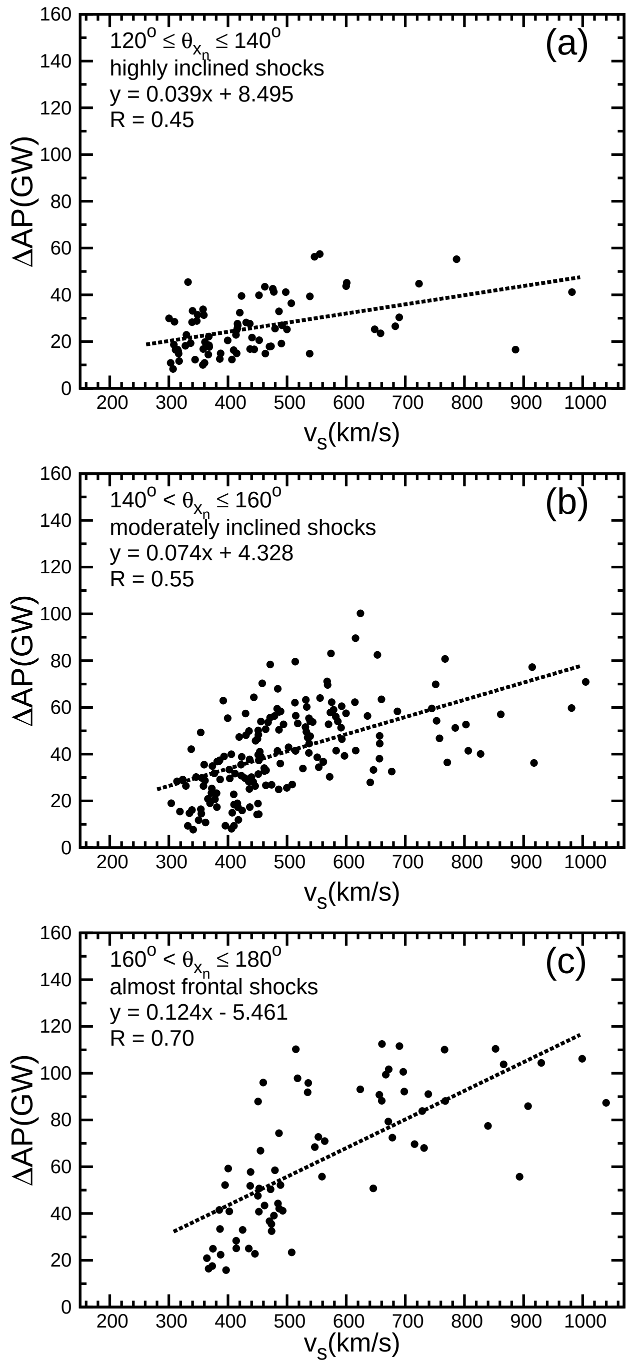

Figure 6-6: Jumps in ΔAP triggered by IP shock impacts plotted as a function of the shock impact angle θ_{x_n}. The events were binned in three different groups in terms of the shock speed: Figure 5(a), $350 \leq v_s \leq 450$ km/s (weak shocks), Figure 5(b), $450 \leq v_s \leq 550$ km/s (moderate shocks), and Figure 5(c) $v_s \geq 550$ km/s (strong shocks). The shocks are more geoeffective for almost frontal and strong (high speed) shocks. Figure from *Oliveira et al.* [2015].

activity are associated with weak, low speed ($v_s < 450$ km/s) shocks. Strong, high speed ($v_s > 550$ km/s) shocks are related to events with moderate auroral activity, with only one event that has low auroral activity being caused by a strong shock. Events with moderate auroral activity are associated with all shock strength categories with approximately the same likelihood. There are no events with high auroral activity triggered by highly inclined shocks in our database. The correlation coefficient in this case is R = 0.45.

The intermediate category of shock strength has the largest number of events, as seen in Figure 6-6(b). In this case, all events with low auroral activity are triggered by weak or low speed shocks. Most events with moderate activity are associated with weak or moderate shocks. All events with high auroral activity are triggered by high speed shocks. The correlation coefficient is R = 0.55. Figure 6-6(c) shows that all weak auroral activity events (only three cases) are related to weak shocks. Events with moderate auroral activity are mostly associated with weak or moderate shocks, but some are related to strong shocks. All events with intense auroral activity are triggered by either moderate or strong shocks. The correlation coefficient R = 0.70 is the highest in this category. These results are summarized in Table 6.2.

The opposite analysis is made in Figure 6-7, i.e., where the shock impact angles are allowed to vary keeping the shock speed constant. The three categories are: Figure 6-7 (a), $350 \leq v_s \leq 450$ km/s, weak shocks; $450 < v_s$ $550 \leq$ km/s, moderate shocks; and $v_s > 550$ km/s, strong shocks. Figure 6-7 (a) shows that weak shocks are associated with events with either weak or moderate auroral activity, and are not related to events with intense auroral activity. There are only a few strong highly inclined shocks, and most of them cause events with moderate auroral activity. Only a few strong highly inclined shocks cause events with low auroral activity. The correlation coefficient for highly inclined shocks, R = 0.39, is the lowest in this case. In the category of moderate shocks, the correlation is stronger,

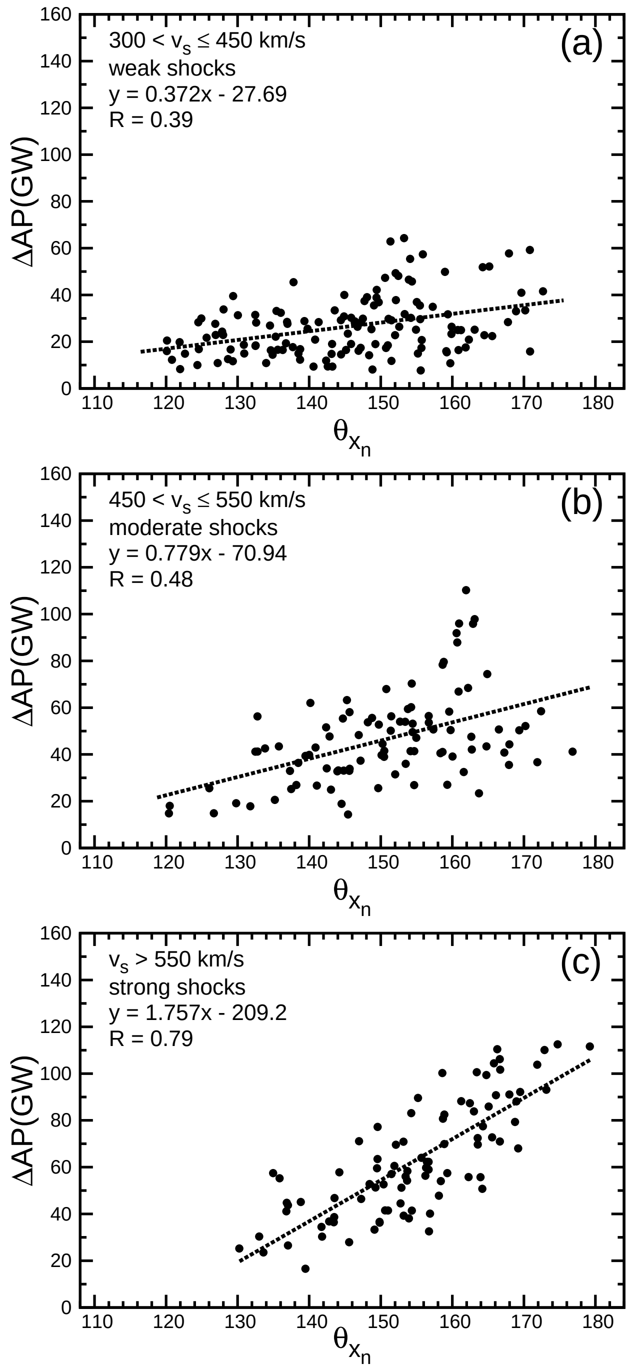

Figure 6-7: Jumps in ΔAP triggered by IP shock impacts plotted as a function of the shock impact angle θ_{x_n}. The events were binned in three different groups in terms of the shock speed: Figure 5(a), $350 \leq v_s \leq 450$ km/s (weak shocks), Figure 5(b), $450 \leq v_s \leq 550$ km/s (moderate shocks), and Figure 5(c) $v_s \geq 550$ km/s (strong shocks). The shocks are more geoeffective for almost frontal and strong (high speed) shocks. Figure from *Oliveira et al.* [2015].

Fixed impact angle θ_{x_n}, changed shock speed v_s			
category	highly inclined	moderately inclined	almost frontal
R	0.45	0.55	0.70
Fixed shock speed v_s, changed impact angle θ_{x_n}			
category	weak	moderate	strong
R	0.39	0.48	0.79

Table 6.2: Summary of the results obtained for the shock speed, shock impact angle, and ΔAP correlation analyses. Table from *Oliveira et al.* [2015].

with R = 0.48. There are only a few events with low auroral activity, and most of them are triggered by highly inclined shocks and just a few by inclined shocks. Moderate almost frontal shocks were not found to trigger weak auroral activity events. Typically, events with moderate auroral activity are triggered by moderate, strong, and weak shocks, respectively. There are only a few events with high auroral activity, and all of them are triggered by moderate almost frontal shocks. Finally, correlations for strong shocks are represented by Figure 6-7 (c). Generally, strong shocks do not cause events with low auroral activity, with an exception of only one event caused by a highly inclined shock. Events with moderate AP activity are typically caused by inclined shocks, but they can also be triggered by highly inclined or almost frontal shocks. Events with intense auroral activity are caused mostly by almost frontal shocks, but a few events are caused by inclined shocks. The correlation coefficient for strong shocks is the highest, R = 0.79. Table 6.2 summarizes the results obtained for correlations with shocks in all categories.

Thus, strong, high speed shocks are generally much more geoeffective than weak slow speed shocks, and their geoeffectiveness increases if the IP shock impacts more frontally the Earth's magnetosphere. These general results were predicted by *Oliveira and Raeder* [2014] in global MHD simulations.

We have studied 461 fast forward interplanetary (IP) shocks using WIND and ACE satellite data from January 1995 to December 2013. The primary result obtained was that high speed shocks with shock normal aligned along the Sun-Earth line (head-on shocks) cause the greatest auroral power release. The correlation coefficient for the cross correlation analysis was 0.79, the highest of any performed in this study. To explain the above result, it should be first noted that shock compression of the magnetosphere is most effective when the inclination angle is frontal. Both the magnetosphere and magnetotail will be compressed the most for this orientation. Greater tail lobe fields will require stronger cross tail currents to maintain them. Magnetosphere/magnetotail compression will lead to more flattened tail closed field lines. Shock-triggering- substorm mechanisms were previously discussed by *Zhou and Tsurutani* [2001] and *Tsurutani and Zhou* [2003]. Both current disruption [*Papadopoulos*, 1979; *Lui et al.*, 1988, 1990] and magnetic reconnection [*Kokubun et al.*, 1977; *Lui et al.*, 1990; *Lyons*, 1995, 1996; *Lakhina et al.*, 2001] are viable under these above conditions. The present results indicate the role of shock speed and inclination angle in geoeffectiveness of magnetospheric energy release (auroral power). Thus this is another factor besides magnetospheric priming that must be taken into account in assessing auroral power release.

6.4 Summary and Conclusions

We investigated WIND and ACE solar wind data at 1 AU to look for fast forward interplanetary (IP) shocks in a time period from January 1995 to December 2013. We studied the geoeffectiveness triggered by IP shock impacts, in particular the jumps in the SuperMAG SML index, to quantify substorm strength, and jumps in auroral power (AP), inferred from the SuperMAG SME index, related to the shock speed (strength) and the shock inclination angles. Our main results are summarized below:

1. We provide the community with the largest IP shock list up to date with events from January 1995 to December 2013, covering the whole solar cycle 23 and half of the

current solar cycle.

2. The number of yearly IP shocks correlates well with the monthly sunspot number. The maximum number of fast forward IP shocks was found in the year 2000, the solar maximum of the solar cycle 23. As expected, the number of IP shocks is smaller in the maximum of the current solar cycle due to the unusual low number of sunspots occurring in this period.

3. The majority of the events (76%) are almost perpendicular shocks, with $\theta_{B_n} \geq 45^o$. Most shocks (78%) have their shock normals close to the Sun-Earth line, or $\theta_{x_n} \geq 135^o$. Also, less than half of the shocks (40%) have their speeds below the average of about 450 km/s, and shocks with the supermagnetosonic Mach number greater than the average 2.1 was 36%. These results indicate that the heliosphere at 1 AU is dominated by weak shocks.

4. Strong (high speed) shocks are more geoeffective than weak shocks. The correlation is improved when shocks are grouped in categories related to their strength and then investigated in terms of their shock impact angles. Our highest result (correlation coefficient of R = 0.78) was found when we fixed the IP shock speed interval and changed the IP shock impact angles. Therefore, high speed and almost frontal shocks showed to be more geoeffective. This result was predicted by *Oliveira and Raeder* [2014].

5. Using a linear relation between the SuperMAG SME index and the auroral power, we studied correlations between the shock impact angles and shock speed (strength) with the auroral power intensity. We found that weak shocks triggered usually small geomagnetic activity, even for almost frontal shocks. We also found that strong highly inclined shocks did not trigger high auroral activity. The highest correlation (R =

0.79) was found in the case in which stronger shocks were almost frontal, i.e., shocks with high impact angles. This result suggests that the magnetosphere is compressed symmetrically on all sides by the shock waves, which leads to favorable conditions of occurrence of auroral events observed in the nightside of the ionosphere. Similar results were observed by *Oliveira and Raeder* [2015], and predicted by global MHD simulations [*Oliveira and Raeder*, 2014].

Chapter 7

Summary and conclusion

7.1 Dissertation results

Interplanetary (IP) shocks are well known to sometimes trigger substorms [*Schieldge and Siscoe*, 1970; *Kawasaki et al.*, 1971; *Burch*, 1972; *Kokubun et al.*, 1977; *Akasofu and Chao*, 1980]. In the early days before shock detection in interplanetary space, SSCs/SI$^+$s (sudden magnetospheric/magnetotail compression events) were used to imply the impingement of an interplanetary shock or tangential discontinuity (TD) onto the magnetosphere. For example, *Kokubun et al.* [1977] examined SSC events and concluded that intense auroral activity always occurred when SSC amplitudes were greater than 40 nT. *Smith et al.* [1986] later showed that most of SSCs/SI$^+$s were caused by interplanetary shocks rather than TDs. Recently precursor IMF B_z events $\sim$ 1.5 hr prior to shock arrival have been used to identify when shocks would be geoeffective and when they would not be [*Craven et al.*, 1986; *Zhou and Tsurutani*, 1999, 2001; *Zhou et al.*, 2003; *Tsurutani and Zhou*, 2003; *Yue et al.*, 2010; *Echer et al.*, 2011].

Studies of geoeffectiveness triggered by IP shocks addressing the IP shock geometry have been done in recent years. The IP shock geoeffectiveness associated with IP shock obliquity was studied by *Jurac et al.* [2002]. The effects of shock normal inclinations in the equatorial plane on SSC rise times were reported by observation [*Takeuchi et al.*, 2002], simulations

[*Guo et al.*, 2005; *Wang et al.*, 2005], and statistical investigations [*Wang et al.*, 2006]. As a result, the literature shows that quasi perpendicular shocks and almost frontal shocks were often associated with higher geomagnetic activity in comparison to quasi-parallel and inclined shocks.

In this dissertation, we were primarily concerned with the geoeffectiveness of IP shocks associated with the IP shock normal inclinations. The IP shock normal inclination was addressed by the angle between the GSE Sun-Earth line and the shock normal vector. The geomagnetic activity investigation was concentrated on the intensity of field-aligned currents and diffusive auroral electron energy precipitation flux (simulations), and substorm strength and auroral power intensity (observations).

Our study was divided into two parts: simulations, first part, and observations, second part. In Chapter 4, we presented our study of geoeffectiveness of IP shocks controlled by IP shock impact angles using global MHD simulations. Using the OpenGGCM (Open Global Geospace Circulation Model) MHD code, we showed that similar IP shocks with different IP shock impact angles may lead to different IP shock geoeffectiveness. We simulated three different IP shocks, where two had shock normals inclined in relation to the Sun-Earth line in the meridian plane. The Mach number of the second shock was twice the Mach number of the first shock. Both shocks were oblique, i.e., their shock normals were at angles close to 45^o with the upstream magnetic field in the shock frame of reference. Finally, in our simulations, a third perpendicular shock impacted the Earth's magnetosphere frontally, with the same Mach number of the first shock. We found that the third shock was much more geoeffective than the other two because the shock was frontal, and the magnetosphere was compressed symmetrically on both north and south sides. This compression led then to the triggering of a strong auroral substorm not seen in the other cases. Our results suggested that the shock normal inclination effects on the IP shock geoeffectiveness would be observed in real IP shock events. The results of these simulations were published in *Journal of Geophysical Research*.

In the second part of our research, which corresponds to Chapter 6 of this dissertation, I developed, implemented, and executed a methodology for finding fast forward interplanetary shocks that took place in the vicinity of the Earth's orbit at 1 AU. We studied approximately 20 years of interplanetary plasma and IMF data to find shock wave events in the near-Earth space environment. My strategies were the following: i) search the literature and other sources to identify events that had already been studied; ii) consult satellite websites that supply data users with a list with a myriad of events identified by the spacecraft team, and some of them are interplanetary shocks; iii) use an automated computer search program to find shock wave events in the raw data; iv) once a shock is identified, different methods to calculate shock normal angles available in the literature were used. By merging all these sources I was able to find 461 events which were used in my study. Codes based on Python language facilitated the process of data analyses. The geomagnetic response was inferred from a chain of more than 300 magnetometers, called SuperMAG, spread all over the world. The data are available at `http://supermag.jhuapl.edu`. The SuperMAG data consist of geomagnetic indices which quantify the strength of auroral events and geomagnetic storms measured on the Earth's surface. This IP shock data base is not yet completed, since even more data for IP shock calculations will become available as more shock wave events happen in the interplanetary space and the SuperMAG team is able to make the geomagnetic data available at their website.

Once my data base was completed (with data up to 2013), the next step was to execute the statistical calculations. Correlations between the shock wave inclination angles with different geomagnetic indices were calculated. The highest correlations found in my statistical analyses occurred when fast shock waves impacted the Earth almost frontally.

My research showed that not only the shock speed is important in determining the shock geoeffectiveness, but also the shock inclination plays an important role in the geomagnetic response triggered by the shock waves. The main results of my research are the validation of my previous results suggested by my numerical simulations, i.e., fast (high speed) shocks may be much more geoeffective if they hit the Earth's magnetopause almost head-on. This study has improved our understanding of the physics of interplanetary shock triggering of geomagnetic activity. As a result, two more papers have been submitted to *Journal of Geophysical Research* and *Journal of Atmospheric and Solar-Terrestrial Physics*, and both are currently under review.

In addition, my statistical study has provided the scientific community with the largest data set based on interplanetary shock waves up to date. My interplanetary shock list will then be used by researchers in other shock wave-related studies.

7.2 Future plans

In the immediate future my plans include:

- Expand our interplanetary shock database to the years 2014 and 2015. The inclusion of 40 or more IP shock events, an increase of approximately 10%, will improve my statistical results because more fast shocks will occur in the current solar phase.

- In our research, I have not paid attention to the shock wave drivers; the most important are: CMEs (coronal mass ejections), and CIRs (corotating interaction regions). In most cases, the former propagate radially away from the sun, and the latter are generated in regions of high solar latitudes. Associating the shock wave with its driver is a good way to understand how these disturbances propagate in the interplanetary space.

- Once the shock driver is identified, i.e., CME or CIR, it will be more convenient to predict how geoeffective the interplanetary shocks driven by them can be. The technique of determining the shock wave front inclination will help space weather forecasters in determining how dangerous these structures may be to the electronic devices located in the near Earth space or on the ground.

My longer-term goals are focused on carrying out more global numerical simulations addressing other space parameters related to the shock geometry. My initial numerical simulations showed that fast and almost head-on shocks trigger ULF waves, or waves with ultra low frequencies with periods of 4-5 minutes. The mechanisms of these wave mode excitations are not currently understood. In the future, with the robustness provided by even more powerful supercomputers, numerical simulations will indicate where and how to search the data to understand the mechanism of cavity mode excitations.

Appendices

Appendix A

IP shock list obtained from WIND and ACE data

This Appendix contains a list with all interplanetary (IP) shock events used in the statistical study of this dissertation. The data used cover almost 20 years of WIND and ACE solar wind and IMF observations from January 1995 to December 2013. This time period contains one and a half solar cycle, including the solar cycle 23. See details in this dissertation (Chapters 2 and 6) and *Oliveira and Raeder* [2015]. This shock list was published by *Oliveira and Raeder* [2015], and can be downloaded from there as a Supporting Information file.

Table A.1: IP shock list from Jan 1995 to Dec 2013[1].

Y	M	D	UT	shock normal	θ_{x_n}	φ_{y_n}	θ_{B_n}	v_s	X	B_z	Ms	SAT
1994	Dec	05	2101	(-0.760, -0.600, 0.249)	139.50	157.48	67.13	378.82	1.55	3.84	1.47	W
1995	Jan	01	1936	(-0.820, -0.461, 0.322)	145.12	235.07	68.08	332.62	2.07	1.19	2.18	W
1995	Feb	26	0255	(-0.803, -0.577, 0.147)	143.45	165.70	32.16	287.50	1.45	-3.17	1.46	W
1995	Mar	04	0036	(-0.683, 0.338, 0.648)	133.06	27.55	80.13	350.72	1.95	-0.35	1.87	W
1995	Mar	23	0937	(-0.950, 0.152, -0.271)	161.87	209.30	77.89	373.36	1.90	-1.84	2.18	W
1995	Apr	17	2333	(-0.865, 0.072, 0.496)	149.92	8.26	81.68	361.93	1.62	2.74	1.30	W
1995	Jul	22	0535	(-0.641, 0.261, -0.722)	129.88	289.86	38.40	272.85	2.15	-0.54	1.27	W
1995	Jul	24	0223	(-0.813, -0.582, 0.032)	144.34	176.81	50.76	351.70	3.01	0.92	3.50	W
1995	Aug	17	0245	(-0.856, 0.447, -0.261)	148.84	329.69	54.89	406.08	2.42	0.16	1.58	W
1995	Aug	22	1256	(-0.809, 0.399, 0.432)	144.02	42.73	51.86	335.28	2.58	0.24	2.17	W
1995	Aug	24	2211	(-0.874, -0.129, -0.469)	150.88	15.33	74.46	348.23	1.58	-0.09	1.68	W
1995	Sep	14	2124	(-0.747, 0.276, 0.604)	138.36	24.58	77.59	395.06	1.43	-1.98	1.46	W
1995	Oct	17	1303	(-0.532, -0.601, -0.596)	122.12	225.24	62.33	252.13	1.26	-2.93	2.00	W
1995	Oct	18	1040	(-0.718, -0.146, -0.681)	135.87	192.10	78.57	323.59	3.44	0.81	3.53	W
1995	Oct	22	2120	(-0.693, 0.468, 0.548)	133.90	40.49	60.19	345.24	1.98	-0.14	1.31	W
1995	Nov	27	0822	(-0.869, -0.254, -0.424)	150.35	210.96	55.62	350.41	1.46	-1.05	1.79	W
1995	Dec	15	0437	(-0.885, 0.393, 0.251)	152.23	57.41	33.62	317.91	2.00	0.54	1.40	W
1995	Dec	24	0557	(-0.862, -0.352, -0.366)	149.52	43.89	64.22	419.00	2.44	-0.06	2.53	W
1996	Feb	06	1914	(-0.838, -0.192, 0.511)	146.89	200.61	62.87	343.32	1.72	1.17	1.35	W
1996	Feb	21	2214	(-0.779, -0.125, 0.615)	141.15	101.53	36.12	349.17	1.80	-0.72	1.01	W
1996	Mar	02	2031	(-0.393, -0.034, 0.919)	113.17	92.12	59.64	200.31	1.40	-0.45	1.16	W
1996	Apr	02	1007	(-0.513, 0.503, 0.696)	120.84	35.84	66.10	228.94	1.48	0.15	1.89	W
1996	Apr	03	0947	(-0.878, -0.421, 0.229)	151.38	151.48	88.29	346.95	1.50	1.03	1.44	W
1996	Apr	08	0241	(-0.465, -0.310, 0.829)	117.72	200.52	72.29	201.73	1.75	1.63	1.62	W
1996	Apr	08	1308	(-0.741, -0.314, 0.593)	137.84	117.93	79.07	314.74	1.43	0.66	2.14	W
1996	Jun	18	2235	(-0.763, -0.378, 0.524)	139.74	125.80	64.95	374.87	1.37	-2.45	0.97	W
1996	Jul	28	1214	(-0.731, 0.682, 0.015)	136.97	88.73	11.44	257.80	1.62	0.74	2.38	W
1996	Aug	12	2211	(-0.498, 0.067, -0.855)	119.88	184.46	34.83	227.51	1.62	-1.78	2.17	W

Y	M	D	UT	shock normal	θ_{x_n}	φ_{y_n}	θ_{B_n}	v_s	X	B_z	Ms	SAT
1996	Aug	16	0745	(-0.643, -0.196, -0.740)	130.05	14.87	59.55	318.34	1.68	0.70	1.38	W
1996	Nov	11	1512	(-0.971, 0.120, -0.207)	166.14	300.10	49.02	370.52	1.86	1.33	1.59	W
1996	Dec	02	1000	(-0.877, 0.399, 0.268)	151.28	56.12	38.71	304.92	1.63	3.03	2.62	W
1996	Dec	09	1850	(-0.739, -0.502, -0.450)	137.63	228.15	48.62	316.64	1.40	0.69	2.06	W
1997	Jan	05	0320	(-0.453, 0.106, 0.885)	116.95	6.81	82.03	242.81	1.64	0.94	1.70	W
1997	Jan	10	0052	(-0.872, -0.274, -0.406)	150.71	213.99	48.82	391.74	2.52	0.10	2.03	W
1997	Feb	09	1250	(-0.814, 0.574, -0.087)	144.52	351.35	59.67	565.82	2.02	-0.68	1.86	W
1997	Feb	27	1729	(-0.780, -0.411, -0.471)	141.30	221.15	60.05	491.75	1.49	0.96	1.81	W
1997	Mar	05	1254	(-0.938, -0.254, 0.235)	159.73	137.21	48.71	374.77	2.15	1.90	1.67	W
1997	Mar	15	2230	(-0.676, -0.520, 0.523)	132.49	134.84	72.58	327.97	1.33	-0.91	1.38	W
1997	Mar	20	1942	(-0.570, -0.078, 0.818)	124.74	95.44	87.06	228.73	1.73	1.07	2.13	W
1997	Mar	23	0821	(-0.473, -0.531, -0.703)	118.26	217.07	43.69	150.61	1.73	-1.21	1.01	W
1997	Apr	10	1258	(-0.623, 0.280, 0.731)	128.51	20.96	86.12	278.09	1.55	3.26	1.27	W
1997	Apr	16	1221	(-0.873, -0.395, 0.287)	150.78	144.05	83.03	373.64	1.51	-3.22	1.37	W
1997	Apr	30	1805	(-0.565, -0.229, 0.793)	124.41	106.09	63.15	261.45	1.84	-1.94	1.99	W
1997	May	01	1202	(-0.678, -0.331, 0.656)	132.70	116.75	28.66	291.70	2.03	-1.20	2.23	W
1997	May	15	0155	(-0.895, -0.407, -0.182)	153.53	65.91	86.14	438.08	2.28	-2.43	2.74	W
1997	May	20	0510	(-0.801, -0.468, -0.374)	143.20	231.35	12.96	304.04	2.51	-2.03	2.74	W
1997	May	25	1349	(-0.938, -0.088, -0.336)	159.65	194.63	84.50	351.51	1.50	1.89	1.46	W
1997	May	26	0909	(-0.593, 0.641, -0.487)	126.40	322.77	23.95	201.33	1.80	0.69	1.40	W
1997	Aug	05	0459	(-0.842, -0.431, 0.323)	147.40	143.13	71.13	367.94	1.48	1.96	1.51	W
1997	Sep	02	2237	(-0.808, -0.486, -0.334)	143.87	235.45	79.12	339.79	1.89	2.62	2.13	W
1997	Sep	03	0838	(-0.982, 0.155, -0.112)	168.97	324.18	69.60	483.60	1.43	0.85	1.13	W
1997	Oct	10	1557	(-0.919, -0.072, 0.389)	156.72	100.44	87.34	467.84	1.54	3.65	1.39	W
1997	Oct	24	1118	(-0.937, -0.326, 0.125)	159.57	158.96	66.92	489.08	2.31	-4.18	1.60	W
1997	Nov	01	0614	(-0.772, -0.366, -0.517)	140.57	35.30	74.48	320.37	1.50	1.84	1.66	W
1997	Nov	09	1003	(-0.474, 0.546, -0.691)	118.31	218.30	67.04	255.48	2.18	0.91	2.05	W
1997	Nov	09	2222	(-0.854, 0.035, 0.518)	148.70	3.84	34.62	372.64	2.00	-4.23	1.43	W
1997	Nov	22	0912	(-0.965, -0.149, 0.214)	164.89	124.92	81.41	486.21	2.72	1.20	2.50	W
1997	Nov	30	0715	(-0.758, -0.453, 0.469)	139.31	134.04	63.50	310.42	1.73	-1.23	2.03	W
1997	Dec	10	0433	(-0.863, 0.008, -0.505)	149.70	270.88	83.57	384.03	2.34	1.70	2.18	W
1997	Dec	23	0109	(-0.551, 0.447, 0.705)	123.41	32.39	59.88	211.21	1.41	0.15	2.34	W
1997	Dec	30	0113	(-0.775, -0.622, -0.107)	140.83	260.24	57.48	366.07	1.97	-1.54	1.99	W
1998	Jan	06	1330	(-0.878, 0.364, 0.312)	151.36	49.41	64.35	392.03	2.66	0.62	1.99	W
1998	Jan	24	0437	(-0.730, -0.056, 0.681)	136.88	94.66	70.00	344.32	2.23	-0.94	2.40	W
1998	Jan	28	1600	(-0.601, -0.145, -0.786)	126.96	190.46	79.14	373.58	1.26	0.50	3.14	W
1998	Jan	31	1553	(-0.791, -0.142, 0.595)	142.32	103.40	74.17	411.66	1.65	-0.83	1.28	W
1998	Feb	18	0750	(-0.886, -0.388, 0.255)	152.35	146.72	78.36	438.12	1.46	-0.31	1.00	W
1998	Mar	04	1100	(-0.938, 0.162, -0.307)	159.70	297.82	64.12	465.99	1.49	-1.63	2.90	W
1998	Apr	07	1653	(-0.882, -0.077, -0.465)	151.87	189.40	41.85	364.99	2.06	-1.55	1.74	W
1998	Apr	23	1730	(-0.943, -0.103, -0.318)	160.50	197.97	47.48	378.59	2.39	-1.15	1.71	W
1998	Apr	30	0844	(-0.658, -0.649, 0.382)	131.13	149.55	50.16	323.00	3.02	0.41	6.84	W
1998	May	01	2120	(-0.844, -0.450, -0.292)	147.58	236.98	66.47	623.92	2.26	2.54	2.86	W
1998	May	03	1658	(-0.820, 0.516, -0.248)	145.07	334.34	43.30	458.52	2.18	-1.22	2.32	W
1998	May	08	0920	(-0.757, 0.413, 0.506)	139.22	39.24	29.09	604.98	1.76	1.24	2.13	A
1998	May	15	1356	(-0.909, -0.414, 0.049)	155.37	263.29	81.70	352.51	3.56	-0.68	2.02	A
1998	May	29	1503	(-0.947, 0.084, -0.310)	161.25	285.13	61.72	660.08	1.85	-3.33	1.32	A
1998	Jun	13	1857	(-0.656, 0.734, -0.176)	131.03	346.51	38.48	299.49	4.01	0.78	1.90	A
1998	Jun	25	1542	(-0.706, -0.708, 0.023)	134.89	178.13	67.74	366.75	1.65	9.87	1.00	A
1998	Jul	05	0314	(-0.893, -0.256, 0.371)	153.20	124.59	89.74	597.06	1.65	0.26	2.37	A
1998	Jul	31	0914	(-0.632, -0.147, -0.761)	129.18	190.94	86.64	374.60	1.56	-4.79	1.21	A
1998	Aug	06	0642	(-0.955, 0.249, 0.162)	162.74	56.95	83.27	436.05	2.10	-5.61	1.00	A
1998	Aug	10	0006	(-0.454, -0.183, 0.872)	116.97	191.87	54.98	324.19	2.02	0.83	2.27	A
1998	Aug	19	1840	(-0.794, -0.607, -0.033)	142.54	266.90	65.43	306.76	2.30	-3.17	2.31	W
1998	Aug	26	0640	(-0.724, 0.060, -0.687)	136.39	275.02	80.00	750.34	2.37	1.82	4.86	W
1998	Sep	24	2321	(-0.933, -0.202, -0.297)	158.97	214.21	76.51	768.07	2.64	0.56	2.77	W
1998	Oct	02	0654	(-0.865, 0.428, -0.263)	149.84	328.45	38.34	917.59	1.65	-2.01	6.06	A
1998	Oct	18	1900	(-0.718, -0.025, -0.696)	135.86	182.04	52.29	315.85	2.48	0.82	2.42	A
1998	Oct	23	1233	(-0.768, 0.344, -0.541)	140.16	302.43	76.38	513.21	2.73	-1.14	1.60	A
1998	Nov	07	0736	(-0.749, -0.464, -0.473)	138.50	224.40	77.19	431.93	1.67	0.87	1.57	A
1998	Nov	08	0420	(-0.978, 0.132, -0.161)	167.97	309.32	78.09	738.90	2.04	-9.41	1.53	A
1998	Nov	30	0417	(-0.891, -0.448, -0.068)	153.02	261.32	66.60	431.32	2.38	-3.15	2.17	A
1998	Dec	01	0254	(-0.605, -0.753, -0.259)	127.21	251.05	76.79	360.46	1.66	2.20	1.42	A
1998	Dec	26	0932	(-0.735, 0.624, -0.266)	137.31	336.88	89.42	486.35	1.58	5.27	1.05	A
1998	Dec	28	1732	(-0.823, -0.341, -0.455)	145.35	216.81	64.62	413.69	1.74	-3.89	1.63	A
1999	Jan	13	0958	(-0.868, -0.353, 0.348)	150.26	135.44	83.37	405.87	1.83	-3.20	2.20	A
1999	Jan	22	1945	(-0.825, 0.425, -0.373)	145.58	318.74	10.95	640.74	1.56	-3.94	1.16	A
1999	Feb	11	0747	(-0.967, -0.237, 0.091)	165.32	158.93	57.43	419.48	1.92	-1.77	1.47	A
1999	Feb	17	0621	(-0.968, -0.122, -0.217)	165.56	209.31	79.48	552.81	1.52	-2.42	1.43	A
1999	Feb	18	0207	(-0.997, -0.062, -0.040)	175.77	236.81	55.21	697.75	2.86	1.14	2.81	A

Y	M	D	UT	shock normal	θ_{x_n}	φ_{y_n}	θ_{B_n}	v_s	X	B_z	Ms	SAT
1999	Feb	28	2033	(-0.909, -0.058, -0.412)	155.41	187.95	86.47	421.95	1.35	-7.28	1.08	A
1999	Mar	10	0040	(-0.904, 0.053, 0.424)	154.68	7.19	74.36	483.69	1.59	-3.34	2.37	A
1999	Apr	16	1034	(-0.859, 0.378, 0.346)	149.22	47.54	36.02	455.56	1.91	0.81	1.72	A
1999	May	05	1458	(-0.763, -0.517, 0.386)	139.77	233.30	80.98	410.76	2.87	1.17	2.08	A
1999	May	18	0002	(-0.956, 0.203, -0.212)	162.94	313.70	9.47	413.02	3.24	-0.26	1.92	A
1999	Jun	26	0231	(-0.939, -0.344, 0.015)	159.87	177.51	84.42	380.68	1.76	1.60	2.04	W
1999	Jun	26	1923	(-0.823, 0.554, 0.123)	145.40	77.49	44.88	371.96	2.26	9.18	1.39	A
1999	Jul	02	0022	(-0.666, 0.497, -0.556)	131.77	311.83	21.61	470.13	2.16	-0.24	1.99	A
1999	Jul	06	1415	(-0.851, -0.165, 0.499)	148.32	108.32	65.35	454.91	1.80	2.92	1.97	A
1999	Aug	04	0114	(-0.894, -0.310, -0.325)	153.34	223.65	63.60	377.02	3.65	-0.71	1.10	A
1999	Aug	08	1744	(-0.818, -0.041, -0.574)	144.88	184.05	25.16	361.07	1.71	-3.49	0.54	A
1999	Aug	15	0937	(-0.932, -0.263, 0.250)	158.72	136.46	72.08	366.83	2.58	-3.04	1.33	A
1999	Aug	22	2248	(-0.854, -0.441, 0.275)	148.68	148.06	73.32	409.88	1.66	-7.41	1.01	A
1999	Aug	23	1129	(-0.907, -0.071, 0.414)	155.14	99.68	76.41	446.67	1.56	-4.72	1.11	A
1999	Sep	12	0320	(-0.863, -0.376, 0.337)	149.69	228.16	70.59	535.70	2.30	-1.23	2.89	A
1999	Sep	15	0717	(-0.923, 0.122, 0.365)	157.40	18.44	64.08	665.59	1.71	0.72	1.63	A
1999	Sep	15	1940	(-0.851, -0.223, 0.476)	148.30	115.07	63.64	541.93	2.26	2.90	1.62	A
1999	Sep	22	1144	(-0.878, 0.142, 0.457)	151.40	17.25	65.98	451.02	3.19	1.04	1.56	A
1999	Sep	26	1426	(-0.904, -0.404, -0.142)	154.65	250.58	86.15	435.68	1.50	-1.41	1.02	A
1999	Oct	21	0137	(-0.895, 0.087, 0.438)	153.47	11.22	48.84	444.82	3.00	3.35	1.66	A
1999	Oct	28	1125	(-0.918, -0.364, 0.155)	156.70	156.98	50.80	444.15	1.72	3.55	1.45	A
1999	Nov	05	2003	(-0.752, -0.054, -0.657)	138.78	184.67	83.32	362.57	1.51	-1.19	1.50	W
1999	Nov	13	1213	(-0.921, 0.347, 0.177)	157.07	62.93	87.60	464.98	2.07	-5.43	1.14	A
1999	Nov	19	2357	(-0.614, 0.040, 0.788)	127.89	2.89	46.37	365.40	1.35	-4.70	1.35	A
1999	Dec	11	1200	(-0.593, -0.015, -0.805)	126.40	181.05	41.76	444.03	1.39	-2.00	3.09	A
1999	Dec	12	1513	(-0.840, -0.161, -0.518)	147.11	197.30	51.64	549.37	2.05	-1.33	1.93	A
1999	Dec	26	2126	(-0.918, -0.225, 0.326)	156.68	124.65	34.75	418.09	1.86	-0.21	0.64	A
2000	Jan	11	1338	(-0.748, -0.491, -0.446)	138.44	227.73	89.99	479.59	1.49	-1.10	1.30	A
2000	Jan	22	0021	(-0.425, 0.008, -0.905)	115.14	180.52	39.48	245.14	1.91	-2.08	1.72	A
2000	Jan	27	1355	(-0.872, -0.188, 0.451)	150.73	112.67	59.37	381.20	2.11	6.69	1.22	A
2000	Jan	30	1844	(-0.930, 0.321, 0.179)	158.43	60.77	39.20	773.58	1.32	-2.45	2.57	A
2000	Feb	05	1448	(-0.971, 0.050, -0.235)	166.08	282.08	57.25	404.20	1.94	-0.36	0.76	A
2000	Feb	11	0211	(-0.894, -0.299, -0.022)	153.42	85.77	31.47	509.62	2.48	-0.10	1.79	A
2000	Feb	11	2318	(-0.851, -0.370, 0.373)	148.33	134.79	84.96	606.57	3.70	-0.75	2.89	A
2000	Feb	14	0700	(-0.996, -0.057, 0.075)	174.62	127.36	75.39	676.95	1.71	-0.11	1.01	A
2000	Feb	20	2044	(-0.571, -0.012, -0.821)	124.85	180.85	83.85	279.70	5.04	-2.25	1.02	A
2000	Apr	06	1632	(-0.972, -0.076, -0.224)	166.34	198.73	69.91	843.84	1.68	1.50	7.52	W
2000	Apr	24	0850	(-0.816, 0.456, -0.355)	144.71	322.08	88.95	536.97	1.57	-0.34	1.29	A
2000	May	17	2140	(-0.358, -0.551, 0.754)	110.95	126.15	62.19	375.08	1.29	1.18	1.64	A
2000	May	23	2342	(-0.999, 0.032, 0.044)	176.90	36.03	84.46	685.04	1.69	1.50	1.03	W
2000	Jun	03	0804	(-0.906, -0.379, 0.190)	154.93	153.37	81.43	436.31	1.40	-1.74	1.39	A
2000	Jun	04	1422	(-0.982, 0.148, -0.118)	169.08	321.60	49.75	672.29	1.71	3.80	3.14	A
2000	Jun	08	0840	(-0.985, 0.000, -0.173)	170.06	270.04	54.10	867.05	3.44	3.40	3.53	A
2000	Jun	11	0716	(-0.963, 0.061, 0.261)	164.44	13.12	39.46	597.02	1.43	-1.17	1.88	A
2000	Jun	23	1226	(-0.785, 0.153, -0.600)	140.11	1.48	75.02	563.79	2.62	-1.59	2.60	A
2000	Jul	10	0556	(-0.848, 0.526, -0.067)	147.97	262.71	67.55	488.56	2.01	-3.08	1.51	A
2000	Jul	11	1121	(-0.725, -0.014, 0.689)	136.46	91.16	67.05	382.58	1.66	0.72	1.52	A
2000	Jul	13	0916	(-0.713, -0.418, -0.563)	135.45	216.59	69.06	570.25	1.85	2.84	1.47	A
2000	Jul	19	1447	(-0.616, 0.644, 0.454)	128.03	54.82	11.42	371.08	2.99	-1.18	1.54	A
2000	Jul	26	1754	(-0.514, 0.837, 0.189)	120.93	77.24	46.83	223.58	1.91	-3.99	1.01	A
2000	Jul	28	0543	(-0.983, 0.181, -0.037)	169.36	348.38	76.02	472.11	3.84	-6.09	1.34	A
2000	Jul	28	0909	(-0.766, -0.302, 0.568)	139.99	118.03	66.73	452.45	1.74	9.07	1.29	A
2000	Aug	10	0407	(-0.942, -0.286, -0.177)	160.34	238.21	57.13	416.84	2.93	-0.98	0.81	A
2000	Aug	11	1809	(-0.736, 0.098, -0.670)	137.36	278.33	60.90	572.77	2.14	-2.08	1.48	A
2000	Aug	14	2136	(-0.613, 0.572, -0.544)	127.84	316.41	44.83	413.38	2.37	-2.17	2.24	A
2000	Sep	04	1110	(-0.539, 0.659, -0.524)	122.65	321.49	36.93	316.52	2.10	0.81	1.60	A
2000	Sep	06	1612	(-0.643, -0.343, 0.685)	130.03	116.62	59.93	359.19	2.83	5.78	1.37	A
2000	Sep	15	0358	(-0.742, 0.348, 0.573)	137.90	31.27	73.15	446.73	1.05	-1.09	5.67	A
2000	Sep	17	1657	(-0.729, 0.663, 0.171)	136.81	75.52	39.24	981.96	1.45	4.02	3.45	A
2000	Sep	30	1037	(-0.942, 0.246, 0.229)	160.39	47.09	87.89	440.00	1.47	-6.69	1.01	A
2000	Oct	03	0007	(-0.831, -0.506, -0.232)	146.19	245.39	64.65	415.73	2.18	-1.64	1.41	A
2000	Oct	04	1336	(-0.991, 0.109, 0.074)	172.40	55.89	82.98	479.41	1.45	-8.32	1.16	A
2000	Oct	05	0239	(-0.956, -0.143, 0.257)	162.89	119.03	77.29	535.72	2.24	-7.30	2.52	A
2000	Oct	12	2233	(-0.957, -0.130, 0.260)	163.12	116.67	72.13	517.61	2.48	3.23	2.55	W
2000	Oct	28	0648	(-0.913, 0.398, 0.095)	155.86	76.53	30.52	577.71	1.10	0.20	5.13	W
2000	Oct	28	0907	(-0.913, 0.243, 0.328)	155.88	36.50	49.37	429.77	3.64	1.11	1.45	A
2000	Oct	31	1630	(-0.833, -0.267, 0.485)	146.37	118.87	43.16	442.77	3.19	-0.92	2.47	A
2000	Nov	04	0133	(-0.703, -0.272, 0.658)	134.65	112.45	89.72	354.16	3.60	3.87	1.26	A
2000	Nov	06	0945	(-0.981, 0.059, -0.186)	168.76	287.66	61.42	671.25	2.53	-1.27	2.23	A
2000	Nov	10	0619	(-0.961, -0.030, 0.275)	163.94	96.22	73.54	893.20	3.34	3.13	2.05	A

Y M D	UT	shock normal	θ_{x_n}	φ_{y_n}	θ_{B_n}	v_s	X	B_z	Ms	SAT
2000 Nov 11	0400	(-0.874, -0.015, 0.487)	150.87	91.82	40.38	843.57	2.29	1.14	1.51	A
2000 Nov 26	0500	(-0.831, -0.078, 0.551)	146.17	98.03	53.41	411.02	1.83	-1.63	1.69	A
2000 Nov 26	1123	(-0.906, -0.423, 0.003)	154.95	179.60	75.87	597.89	2.60	4.81	2.43	A
2000 Nov 28	0455	(-0.852, 0.180, -0.492)	148.43	290.13	70.97	570.05	1.73	-2.91	1.91	A
2000 Nov 29	0305	(-0.822, 0.564, -0.078)	145.28	352.13	87.94	531.77	1.73	-7.73	1.06	A
2000 Dec 03	0318	(-0.957, 0.154, -0.248)	163.04	301.80	65.81	495.10	1.40	3.63	1.24	A
2000 Dec 22	1939	(-0.791, 0.512, -0.335)	142.29	326.82	86.79	280.08	1.59	0.45	2.10	W
2001 Jan 04	0114	(-0.941, 0.017, -0.338)	160.23	272.89	65.97	487.60	1.34	-2.21	2.63	W
2001 Jan 10	1519	(-0.873, -0.478, 0.093)	150.84	168.96	63.07	357.73	2.67	-2.97	1.01	A
2001 Jan 13	0140	(-0.442, -0.257, 0.859)	116.26	106.63	40.96	287.06	4.97	4.35	1.02	A
2001 Jan 17	1530	(-0.875, -0.282, -0.395)	150.99	215.53	43.48	410.24	1.98	1.09	2.49	A
2001 Jan 23	1004	(-0.811, -0.573, 0.120)	144.18	168.16	43.97	469.75	4.42	0.97	2.38	A
2001 Jan 31	0722	(-0.724, 0.661, 0.200)	136.35	73.18	49.03	393.24	3.62	-1.66	1.55	A
2001 Feb 12	2045	(-0.830, -0.312, -0.462)	146.09	214.06	57.11	442.80	1.57	-4.52	1.61	A
2001 Mar 03	1040	(-0.953, 0.304, 0.021)	162.28	86.11	60.81	558.94	1.80	-2.14	1.98	A
2001 Mar 19	1133	(-0.933, -0.300, 0.198)	158.97	146.57	73.67	435.54	1.66	1.81	2.08	W
2001 Mar 27	0108	(-0.654, -0.071, -0.753)	130.86	185.38	37.05	354.67	4.35	-1.69	3.35	A
2001 Mar 27	1714	(-0.727, -0.584, -0.361)	136.62	238.29	82.11	509.77	2.03	-0.74	1.76	A
2001 Mar 31	0022	(-0.908, -0.274, -0.318)	155.20	220.78	59.66	615.70	2.95	-3.54	5.46	A
2001 Apr 04	1423	(-0.865, 0.319, 0.388)	149.88	39.39	6.88	797.15	1.89	1.67	6.67	A
2001 Apr 07	1658	(-0.942, -0.324, -0.084)	160.43	255.55	11.06	640.69	2.20	0.24	4.16	A
2001 Apr 08	1030	(-0.936, -0.347, -0.064)	159.36	259.55	73.91	752.66	2.71	-3.20	3.79	A
2001 Apr 11	1409	(-0.897, -0.336, 0.288)	153.73	139.36	7.07	686.63	2.28	-1.38	3.11	W
2001 Apr 11	1527	(-0.921, -0.188, 0.341)	159.76	191.26	37.07	754.04	1.82	-4.05	2.47	A
2001 Apr 13	0703	(-0.918, 0.205, 0.339)	156.64	31.20	8.02	797.91	1.55	-0.94	2.25	A
2001 Apr 18	0005	(-0.943, -0.113, 0.312)	160.59	109.93	86.22	534.76	3.46	-1.34	2.60	A
2001 Apr 21	1504	(-0.883, 0.468, 0.044)	151.99	84.61	31.47	372.48	2.23	1.19	2.27	A
2001 Apr 28	0500	(-0.686, 0.615, 0.389)	133.33	57.70	31.86	691.82	1.86	2.41	4.20	W
2001 May 08	0930	(-0.613, -0.656, 0.441)	127.78	146.06	83.88	307.50	1.79	-3.31	0.84	A
2001 May 12	0922	(-0.675, -0.348, -0.650)	132.48	208.16	83.21	497.63	1.29	-7.37	1.00	A
2001 May 27	1416	(-0.960, -0.150, 0.236)	163.78	122.43	80.91	624.44	2.20	-0.55	2.15	A
2001 Jun 07	0851	(-0.773, -0.589, -0.237)	140.60	248.04	72.78	425.86	1.73	-1.45	1.18	A
2001 Aug 03	0624	(-0.977, 0.127, 0.170)	167.77	36.79	39.61	462.99	3.65	-4.21	2.09	A
2001 Aug 05	1155	(-0.850, -0.210, 0.484)	148.20	113.43	88.22	563.95	1.26	-3.69	1.63	A
2001 Aug 12	1048	(-0.579, 0.088, 0.810)	125.41	6.17	10.00	286.19	4.81	2.55	2.03	A
2001 Aug 17	1014	(-0.991, 0.105, -0.084)	172.24	321.30	81.61	492.28	4.57	2.60	2.28	A
2001 Aug 27	1918	(-0.745, -0.211, 0.632)	138.20	108.49	70.72	536.43	2.72	-2.72	2.67	A
2001 Aug 30	1329	(-0.902, -0.177, 0.393)	154.47	114.32	51.74	537.33	1.60	-3.66	1.85	A
2001 Sep 14	0116	(-0.794, -0.523, 0.309)	142.59	149.44	89.90	395.59	2.75	3.60	1.53	A
2001 Sep 29	0905	(-0.912, 0.314, 0.263)	155.82	49.98	23.90	696.55	2.25	-1.12	2.70	A
2001 Sep 30	1845	(-0.969, -0.239, 0.069)	165.59	163.88	80.74	780.87	1.38	-3.37	4.98	A
2001 Oct 11	1619	(-0.997, -0.079, -0.015)	175.39	259.20	62.02	562.77	3.32	0.55	2.21	A
2001 Oct 14	1707	(-0.746, -0.653, -0.129)	138.29	258.86	63.87	362.46	1.64	-3.61	0.68	A
2001 Oct 21	1612	(-0.993, 0.120, 0.005)	173.13	87.77	78.94	623.69	2.87	-4.82	2.83	A
2001 Oct 25	0802	(-0.844, -0.285, 0.454)	147.58	122.16	47.52	458.80	3.46	0.20	4.91	A
2001 Oct 28	0242	(-0.961, 0.179, 0.209)	164.01	40.61	61.57	551.73	3.05	-3.53	1.89	A
2001 Oct 31	1252	(-0.763, -0.426, -0.486)	139.77	221.24	50.55	415.74	2.40	-0.83	2.49	A
2001 Nov 19	1735	(-0.946, -0.172, -0.276)	161.01	211.97	66.55	627.39	2.13	0.38	2.11	A
2001 Nov 30	1726	(-0.854, 0.241, 0.461)	148.66	27.64	62.40	333.59	1.75	0.06	0.95	A
2001 Dec 21	1410	(-0.930, -0.077, 0.360)	158.39	102.06	59.23	585.75	1.27	3.20	2.03	W
2001 Dec 23	2218	(-0.918, -0.047, 0.394)	156.64	96.84	75.59	352.59	3.30	-0.37	1.61	A
2001 Dec 29	0445	(-0.979, -0.009, 0.202)	168.35	182.69	55.31	479.25	3.43	4.62	2.86	A
2001 Dec 30	1930	(-0.992, -0.067, 0.104)	172.89	122.83	76.13	649.61	2.53	6.91	1.75	A
2002 Jan 10	1544	(-0.998, 0.048, -0.029)	176.80	329.30	71.05	695.18	1.96	-2.65	1.72	A
2002 Jan 31	2037	(-0.812, -0.035, 0.069)	144.29	207.11	86.31	590.60	1.19	-0.15	5.90	A
2002 Feb 17	0208	(-0.558, -0.355, 0.750)	123.95	115.35	60.57	270.06	3.48	1.84	1.56	A
2002 Mar 18	1236	(-0.818, -0.208, -0.536)	144.87	201.23	58.15	422.60	3.45	0.94	3.07	A
2002 Mar 20	1304	(-0.851, 0.197, 0.487)	148.72	22.03	50.44	466.32	1.84	-0.43	1.50	A
2002 Mar 22	0321	(-0.567, 0.823, 0.003)	124.57	89.82	32.58	437.45	1.21	2.50	2.83	A
2002 Mar 23	1052	(-0.840, 0.234, 0.489)	147.16	25.51	48.04	451.99	3.38	1.54	1.88	A
2002 Mar 25	0057	(-0.839, 0.433, 0.327)	147.08	52.92	57.18	495.93	2.04	8.55	0.41	A
2002 Apr 17	1028	(-0.901, 0.091, 0.423)	154.33	12.19	81.88	457.86	4.27	-6.87	2.04	A
2002 Apr 19	0801	(-0.956, -0.291, -0.024)	163.02	265.28	78.68	728.63	2.26	2.28	1.33	A
2002 Apr 23	0414	(-0.957, 0.275, -0.089)	163.18	342.11	51.02	695.79	2.67	-1.23	3.57	A
2002 May 10	1029	(-0.883, -0.311, 0.351)	152.04	221.51	67.70	409.89	2.45	0.39	1.60	A
2002 May 11	0924	(-0.936, -0.039, 0.349)	159.46	96.36	23.96	446.63	2.32	-3.58	1.82	A
2002 May 18	1918	(-0.886, -0.411, 0.215)	152.37	152.34	83.68	515.29	2.92	0.13	3.85	A
2002 May 20	0300	(-0.811, -0.577, -0.093)	144.22	260.83	74.19	592.35	1.27	4.61	2.14	A
2002 May 21	2100	(-0.834, -0.550, -0.054)	146.48	264.36	84.00	445.37	1.30	2.83	4.75	A
2002 May 23	1014	(-0.847, -0.062, -0.528)	147.87	186.69	81.30	970.90	1.40	4.29	4.99	A

Y	M	D	UT	shock normal	θ_{x_n}	φ_{y_n}	θ_{B_n}	v_s	X	B_z	Ms	SAT
2002	May	30	0131	(-0.591, 0.387, -0.707)	126.21	208.72	64.66	458.44	1.72	1.71	2.07	A
2002	Jul	17	1524	(-0.583, -0.799, -0.150)	125.66	259.37	35.42	405.44	2.90	1.12	3.04	A
2002	Jul	19	0931	(-0.583, -0.437, -0.685)	125.66	212.54	55.51	440.62	2.78	-1.05	2.05	A
2002	Jul	19	1441	(-0.381, -0.666, -0.641)	112.43	226.13	84.95	503.46	1.62	1.83	2.07	A
2002	Jul	22	0450	(-0.792, -0.157, 0.590)	142.37	104.87	60.63	531.02	1.48	0.58	2.29	A
2002	Jul	25	1250	(-0.744, -0.659, 0.112)	138.05	170.33	88.19	545.12	1.07	0.39	1.66	A
2002	Jul	29	1239	(-0.826, -0.289, 0.484)	145.66	120.84	63.30	526.72	2.00	0.80	3.54	A
2002	Aug	01	0422	(-0.849, 0.449, 0.279)	148.07	58.16	25.11	446.25	2.83	-1.20	1.06	A
2002	Aug	01	2217	(-0.923, 0.230, -0.309)	157.35	306.76	85.39	463.65	1.77	5.86	1.07	A
2002	Aug	18	1809	(-0.902, 0.421, -0.101)	154.37	346.56	43.85	564.13	4.18	0.06	3.73	A
2002	Aug	26	1113	(-0.911, 0.412, -0.011)	155.69	358.50	25.81	604.76	1.07	-1.97	3.80	A
2002	Sep	07	1608	(-0.931, -0.363, -0.039)	158.61	263.80	85.93	624.12	2.92	-7.83	2.40	A
2002	Oct	02	2212	(-0.936, -0.245, -0.251)	159.46	224.28	84.09	519.61	2.23	-1.23	1.85	A
2002	Nov	09	1754	(-0.965, 0.145, -0.216)	164.89	303.87	73.63	441.45	1.75	4.12	1.90	A
2002	Nov	11	1154	(-0.505, -0.729, -0.462)	120.33	237.68	79.36	391.09	1.24	3.32	1.28	A
2002	Nov	16	2305	(-0.857, 0.514, -0.029)	149.00	356.79	22.63	492.52	1.45	-2.17	2.06	A
2002	Nov	20	1018	(-0.762, 0.413, 0.498)	139.68	39.62	7.18	385.08	1.70	-3.54	1.61	A
2002	Nov	26	2108	(-0.917, -0.360, 0.173)	156.45	154.27	70.43	614.74	2.47	1.31	2.39	A
2002	Dec	22	1213	(-0.966, -0.141, -0.215)	165.08	213.29	62.76	583.12	1.23	6.76	1.01	A
2002	Dec	24	1313	(-0.954, -0.281, 0.110)	162.46	158.64	34.93	574.25	1.57	-0.65	1.44	A
2003	Jan	01	2059	(-0.739, 0.673, -0.029)	137.66	357.55	57.47	494.94	1.20	-3.29	2.85	A
2003	Feb	17	2300	(-0.568, 0.344, 0.748)	124.63	24.70	47.96	521.92	1.37	-0.45	2.22	A
2002	Mar	20	0419	(-0.828, 0.537, 0.161)	145.90	73.36	61.55	795.35	1.59	3.73	1.24	A
2002	Mar	26	1650	(-0.601, -0.565, -0.566)	126.94	224.94	62.07	329.70	1.59	3.44	1.61	A
2003	Apr	08	0014	(-0.874, 0.193, 0.446)	150.90	23.38	47.17	362.79	2.59	2.08	2.73	A
2003	Apr	28	1833	(-0.961, -0.273, -0.047)	163.90	260.26	50.19	517.21	1.64	3.33	0.76	A
2003	May	09	0454	(-0.848, 0.491, 0.198)	148.04	67.98	59.53	818.51	2.83	0.69	1.34	A
2003	May	29	1150	(-0.973, -0.113, 0.201)	166.64	119.36	52.92	724.94	1.82	-1.50	2.71	A
2003	May	29	1829	(-0.970, 0.045, 0.241)	165.82	10.67	84.95	929.94	1.70	-11.47	1.89	A
2003	May	30	1550	(-0.901, -0.307, 0.307)	154.25	135.02	86.47	805.76	1.82	9.88	1.53	A
2003	Jun	18	0427	(-0.918, -0.376, 0.122)	156.69	162.01	77.02	575.40	1.55	-5.58	1.17	A
2003	Jun	20	0754	(-0.795, -0.030, 0.606)	142.66	92.84	26.84	572.28	2.23	0.09	2.37	A
2003	Jul	06	1222	(-0.556, 0.505, -0.660)	123.79	307.40	73.09	467.57	1.70	2.19	1.58	A
2003	Aug	17	1339	(-0.985, -0.089, 0.150)	169.97	120.79	63.98	722.01	1.31	5.38	4.21	A
2003	Oct	24	1447	(-0.996, 0.061, 0.069)	174.71	41.82	51.14	660.47	3.34	-6.51	2.51	A
2003	Oct	26	0818	(-0.701, -0.671, 0.240)	134.49	160.31	13.35	350.67	1.62	-0.84	2.20	A
2003	Oct	26	1830	(-0.928, -0.273, -0.253)	158.12	227.19	79.57	656.47	1.51	-2.08	1.30	A
2003	Oct	28	0130	(-0.682, -0.726, 0.089)	133.01	172.99	65.47	689.68	1.33	-0.59	1.80	A
2003	Nov	04	0600	(-0.963, 0.270, 0.002)	164.36	89.55	25.80	858.00	2.92	0.26	3.92	A
2003	Nov	06	1919	(-0.664, 0.746, -0.048)	131.64	356.33	51.23	520.59	3.20	-3.43	2.88	A
2003	Nov	15	0518	(-0.859, -0.340, 0.384)	149.15	131.46	73.45	742.64	2.26	1.35	2.11	A
2003	Nov	20	0727	(-0.973, 0.121, -0.196)	166.69	301.65	50.96	671.93	3.31	-2.81	2.87	A
2003	Nov	22	1000	(-0.640, 0.199, 0.742)	129.80	15.05	72.73	490.43	1.70	2.27	1.11	A
2003	Nov	30	0245	(-0.884, -0.050, 0.464)	152.18	96.11	67.90	505.41	1.35	-0.57	1.75	A
2003	Dec	07	1341	(-0.634, -0.426, 0.645)	129.37	123.40	69.82	422.98	2.37	-1.30	1.55	A
2004	Jan	06	1925	(-0.794, -0.543, 0.274)	142.56	153.27	86.04	616.44	1.87	1.32	1.00	A
2004	Jan	22	0103	(-0.982, 0.045, 0.182)	169.20	13.99	79.62	731.63	3.18	-1.45	3.36	A
2004	Jan	23	1420	(-0.806, -0.493, -0.327)	143.71	236.42	72.03	533.27	2.13	-2.87	1.06	A
2004	Apr	03	0854	(-0.712, -0.634, 0.301)	135.42	154.64	47.46	340.13	1.89	-0.85	1.06	A
2004	Apr	09	0148	(-0.877, -0.338, -0.342)	151.24	224.64	87.60	508.39	2.04	-4.33	1.48	A
2004	Apr	10	1924	(-0.855, 0.012, 0.518)	148.76	1.37	84.79	547.13	2.02	-1.26	4.32	A
2004	Apr	12	0424	(-0.838, -0.087, 0.539)	146.93	99.14	80.06	451.36	2.01	-1.31	1.41	A
2004	Apr	12	1734	(-0.677, 0.004, 0.736)	132.59	0.35	34.98	430.83	2.55	0.19	2.73	A
2004	Apr	24	0807	(-0.885, -0.203, -0.419)	152.25	205.81	73.26	526.06	1.51	2.00	1.95	A
2004	Apr	26	1516	(-0.987, -0.050, -0.152)	170.77	198.21	9.60	557.00	1.93	-0.93	1.61	A
2004	May	10	2157	(-0.803, 0.207, 0.559)	143.41	20.32	48.09	360.17	1.72	-0.60	1.01	A
2004	Jul	16	2105	(-0.996, -0.075, -0.042)	175.07	240.99	84.48	471.14	2.07	-3.77	1.20	A
2004	Jul	22	0953	(-0.752, -0.617, -0.231)	138.79	249.45	32.96	433.59	3.39	-1.31	2.30	A
2004	Jul	24	0532	(-0.812, -0.334, -0.478)	144.34	214.93	23.58	545.23	2.27	-0.65	3.70	W
2004	Jul	26	2226	(-0.953, -0.184, 0.239)	162.46	127.58	55.50	1039.60	2.66	0.65	5.30	A
2004	Jul	30	2030	(-0.824, 0.413, -0.388)	145.48	316.78	47.69	532.13	2.33	-1.05	2.11	A
2004	Aug	01	0146	(-0.850, 0.032, -0.525)	148.26	273.53	20.68	482.84	1.82	-1.10	1.72	A
2004	Aug	29	0916	(-0.986, 0.120, -0.116)	170.42	316.05	41.23	472.31	2.03	2.05	1.57	A
2004	Sep	22	0552	(-0.703, 0.511, 0.496)	134.64	45.85	25.80	409.58	2.29	3.01	1.31	A
2004	Oct	27	1117	(-0.995, 0.093, -0.023)	174.53	346.22	44.82	441.27	1.55	2.14	1.35	A
2004	Nov	07	0959	(-0.625, -0.756, -0.196)	128.65	255.48	62.21	386.22	2.83	2.21	3.50	A
2004	Nov	07	1752	(-0.840, -0.542, 0.017)	147.15	178.16	80.85	649.06	1.93	18.55	1.62	A
2004	Nov	09	0913	(-0.716, 0.414, -0.562)	135.76	306.41	24.59	803.59	3.20	-0.85	4.11	A
2004	Nov	09	1820	(-0.990, 0.061, -0.126)	171.93	295.85	8.33	855.60	2.30	-1.95	3.67	A
2004	Nov	11	1643	(-0.653, -0.085, -0.753)	130.73	186.46	67.80	501.37	2.29	1.37	2.18	A

Y	M	D	UT	shock normal	θ_{x_n}	φ_{y_n}	θ_{B_n}	v_s	X	B_z	Ms	SAT
2004	Dec	11	1255	(-0.850, 0.515, -0.111)	148.20	347.85	38.11	543.38	2.21	-0.88	3.85	A
2004	Dec	29	1234	(-0.862, -0.440, 0.253)	149.53	150.09	32.20	412.42	1.71	-1.79	1.01	A
2005	Jan	01	1006	(-0.778, -0.390, 0.493)	141.07	128.38	63.62	464.04	1.50	0.87	1.63	A
2005	Jan	07	0840	(-0.655, -0.052, 0.754)	130.92	93.93	21.14	414.78	1.47	2.31	1.41	A
2005	Jan	17	0715	(-0.889, 0.288, 0.356)	152.76	38.93	31.43	656.70	2.10	1.16	3.18	A
2005	Jan	17	1042	(-0.646, -0.239, 0.725)	130.24	108.27	83.41	648.15	1.52	-5.74	1.01	A
2005	Jan	21	1649	(-0.992, -0.091, -0.090)	172.63	225.34	89.01	1099.99	2.14	-0.81	4.40	A
2005	Feb	17	2204	(-0.947, 0.320, 0.042)	161.17	82.50	84.72	425.31	1.70	4.39	1.01	A
2005	Apr	29	1503	(-0.616, -0.626, 0.478)	128.04	142.67	86.30	357.76	1.21	-2.70	3.11	A
2005	May	06	1204	(-0.951, -0.280, -0.134)	161.90	244.50	50.28	402.54	2.14	1.90	1.36	A
2005	May	07	1819	(-0.944, -0.301, 0.134)	160.76	155.93	61.11	435.20	1.74	-5.59	1.01	A
2005	May	20	0315	(-0.865, 0.495, -0.086)	149.83	350.11	69.17	488.33	1.27	-0.92	3.22	A
2005	May	29	0903	(-0.416, -0.710, -0.568)	114.57	231.37	54.79	271.64	1.53	9.56	1.12	A
2005	Jun	12	0652	(-0.697, -0.188, -0.692)	134.19	195.24	71.99	303.90	2.69	-1.78	1.80	A
2005	Jun	14	1754	(-0.804, -0.093, 0.588)	143.50	98.95	48.12	550.92	1.85	-0.06	3.34	A
2005	Jun	16	0810	(-0.892, -0.203, 0.403)	153.18	116.76	79.75	1005.18	1.13	6.68	4.31	A
2005	Jul	10	0248	(-0.948, 0.170, 0.268)	161.48	32.45	85.73	490.27	1.73	-6.03	1.49	A
2005	Jul	16	0151	(-0.799, -0.600, -0.036)	143.05	266.57	84.44	485.74	1.09	-3.25	3.01	A
2005	Jul	16	1616	(-0.894, -0.232, 0.383)	153.42	121.18	11.17	401.73	1.53	-0.28	1.03	A
2005	Jul	17	0053	(-0.499, 0.799, -0.335)	119.94	337.26	72.07	413.74	1.41	3.78	2.55	A
2005	Aug	01	0606	(-0.693, -0.023, -0.721)	133.83	181.79	87.43	475.84	1.92	1.27	1.01	A
2005	Aug	23	1938	(-0.860, 0.464, 0.214)	149.27	65.28	65.20	645.94	1.23	2.78	3.40	A
2005	Aug	24	0538	(-0.901, 0.150, 0.408)	154.26	20.18	65.36	574.18	2.33	6.17	1.75	A
2005	Aug	25	1308	(-0.732, 0.438, 0.522)	137.03	40.02	7.52	599.85	2.29	-1.97	1.84	A
2005	Sep	02	1340	(-0.961, -0.247, 0.125)	163.96	153.17	84.64	611.29	1.92	2.78	2.10	A
2005	Sep	09	1317	(-0.894, -0.090, 0.438)	153.41	101.59	47.70	455.69	4.84	-2.16	3.46	A
2005	Sep	12	0604	(-0.986, -0.117, -0.118)	170.44	224.93	24.08	1095.13	1.69	-2.66	1.72	A
2005	Sep	15	0830	(-0.832, -0.456, 0.316)	146.35	145.28	30.23	771.69	1.61	-1.18	6.79	A
2005	Dec	30	2346	(-0.852, 0.448, -0.272)	148.38	328.77	87.60	543.33	1.70	-1.25	1.06	A
2006	Jan	01	1331	(-0.648, 0.140, 0.749)	130.36	10.61	79.31	439.05	1.72	6.76	1.10	A
2006	Apr	08	2316	(-0.741, -0.669, 0.059)	137.81	174.96	74.58	332.40	1.42	-5.94	1.03	A
2006	Apr	13	1113	(-0.955, -0.297, 0.018)	162.72	176.44	56.05	486.59	1.94	-1.39	1.23	A
2006	Jul	09	2040	(-0.770, 0.638, -0.028)	140.34	357.45	64.58	409.06	2.64	-0.18	2.65	W
2006	Aug	15	1625	(-0.498, -0.032, -0.867)	119.85	182.11	88.36	211.96	1.65	2.00	1.60	W
2006	Aug	17	0633	(-0.907, -0.415, -0.071)	155.09	260.32	69.24	359.10	1.67	1.59	3.11	W
2006	Aug	18	1551	(-0.998, 0.021, 0.065)	176.09	18.10	63.72	761.97	1.12	3.64	5.01	A
2006	Aug	19	1051	(-0.873, 0.342, 0.348)	150.78	44.50	39.93	484.17	1.88	1.26	1.38	A
2006	Aug	21	1556	(-0.698, 0.716, -0.018)	134.28	358.54	33.25	456.48	1.25	0.25	1.90	A
2006	Sep	09	2329	(-0.905, 0.021, 0.424)	154.87	2.79	25.09	458.24	1.93	0.63	2.58	A
2006	Oct	27	0129	(-0.559, 0.129, 0.819)	123.96	8.95	85.73	255.83	1.40	-0.09	2.04	W
2006	Nov	03	0937	(-0.967, -0.110, -0.231)	165.16	205.45	84.46	395.01	1.46	1.08	1.40	W
2006	Dec	14	1353	(-0.891, -0.331, 0.310)	153.04	136.91	29.13	967.19	2.08	-1.85	5.15	A
2006	Dec	16	1753	(-0.486, 0.871, 0.068)	119.10	85.56	72.07	399.28	4.16	1.10	1.52	A
2006	Dec	18	0921	(-0.950, 0.195, 0.243)	161.86	38.67	61.18	445.68	1.79	-1.20	1.55	A
2007	Feb	12	0912	(-0.922, -0.384, 0.046)	157.26	173.15	87.38	373.63	1.85	0.51	1.39	A
2007	May	07	0702	(-0.838, -0.529, 0.135)	146.88	165.65	81.45	328.68	2.04	-2.02	2.40	W
2007	Jul	20	0327	(-0.559, -0.766, 0.318)	124.01	157.47	80.41	252.60	1.70	-0.15	1.65	W
2007	Aug	22	0434	(-0.979, -0.191, -0.075)	168.19	248.61	80.32	356.83	1.57	0.69	1.63	W
2007	Sep	20	0923	(-0.581, -0.637, 0.507)	125.51	141.51	89.27	296.98	1.60	2.80	1.92	W
2007	Sep	27	1053	(-0.961, 0.065, 0.270)	163.87	13.58	46.62	416.37	2.71	1.52	1.22	A
2007	Oct	25	1040	(-0.884, -0.224, 0.409)	152.18	118.71	60.94	425.00	2.65	-0.90	3.21	W
2007	Nov	12	2127	(-0.377, -0.483, 0.790)	112.15	121.41	42.56	261.63	1.40	-1.11	1.43	A
2007	Nov	18	2121	(-0.437, -0.807, 0.398)	115.88	153.78	82.39	248.05	1.96	-0.44	1.01	W
2007	Nov	19	1722	(-0.965, 0.051, 0.258)	164.75	11.26	34.88	454.85	1.72	1.43	1.75	W
2007	Dec	17	0204	(-0.713, -0.694, 0.103)	135.44	171.57	55.69	352.73	1.80	2.70	2.33	A
2008	Jan	12	1134	(-0.857, -0.382, -0.345)	149.02	227.90	21.79	505.72	1.04	-0.41	5.25	A
2008	Apr	23	0224	(-0.849, -0.296, 0.437)	148.14	124.17	88.12	433.11	1.23	2.71	1.08	A
2008	Apr	30	1502	(-0.810, 0.586, -0.027)	144.11	357.36	14.75	352.62	1.57	-0.33	1.73	W
2008	May	28	0117	(-0.890, -0.148, -0.431)	152.86	198.92	86.83	383.50	2.13	-2.84	2.03	W
2008	Jun	24	1910	(-0.712, -0.478, 0.514)	135.39	132.90	76.37	297.01	1.60	0.66	1.42	W
2008	Jul	22	0610	(-0.452, -0.335, 0.826)	116.89	112.10	84.15	240.06	1.17	-2.31	2.03	A
2008	Aug	08	2251	(-0.688, -0.560, -0.462)	133.48	230.48	61.77	349.66	1.65	4.55	0.83	A
2008	Sep	14	1813	(-0.781, -0.528, 0.334)	141.33	147.74	78.43	313.84	1.46	-1.17	1.57	W
2008	Nov	24	2229	(-0.880, -0.256, -0.400)	151.66	212.67	79.92	325.45	2.45	1.84	2.42	W
2009	Jan	14	0018	(-0.747, -0.510, 0.426)	138.34	140.18	49.06	312.75	1.53	0.46	1.63	W
2009	Feb	03	1921	(-0.985, 0.087, 0.147)	170.19	30.70	68.94	386.48	1.99	-0.81	1.31	W
2009	Feb	10	1209	(-0.635, -0.186, 0.749)	129.44	193.95	73.37	238.14	1.50	-1.18	2.53	W
2009	Mar	03	0504	(-0.878, -0.310, 0.366)	151.36	130.24	85.90	329.51	1.94	0.37	2.21	W
2009	Apr	23	2341	(-0.824, -0.510, 0.249)	145.44	153.99	69.09	362.40	1.95	1.03	2.11	W
2009	May	28	0404	(-0.926, -0.080, -0.369)	157.83	192.24	60.16	361.93	3.00	-0.49	3.71	W

Y	M	D	UT	shock normal	θ_{x_n}	φ_{y_n}	θ_{B_n}	v_s	X	B_z	Ms	SAT
2009	Jun	24	0952	(-0.943, -0.228, -0.243)	160.52	223.16	84.62	345.40	1.74	1.86	2.04	W
2009	Jun	24	1429	(-0.938, 0.031, -0.346)	159.65	275.09	62.33	377.94	1.67	0.03	2.05	W
2009	Jun	27	1104	(-0.938, -0.015, -0.348)	159.64	182.42	89.85	413.61	1.56	2.10	1.18	W
2009	Aug	30	0033	(-0.942, -0.307, -0.136)	160.39	246.06	55.12	394.66	1.76	1.12	1.78	W
2009	Sep	03	1458	(-0.999, 0.054, 0.002)	176.92	87.35	27.58	420.56	1.89	0.31	3.65	W
2009	Oct	04	0317	(-0.671, 0.617, -0.411)	132.14	326.33	22.32	252.72	2.23	1.30	2.41	W
2009	Oct	10	2250	(-0.690, -0.661, -0.295)	133.65	65.91	81.11	271.23	1.63	-0.99	2.80	W
2009	Oct	21	2315	(-0.781, 0.125, 0.612)	141.37	11.58	79.56	288.14	1.95	-1.51	2.04	W
2009	Dec	05	0526	(-0.913, -0.238, -0.332)	155.88	215.56	40.37	265.63	2.38	0.34	2.93	W
2010	Jan	11	0838	(-0.530, -0.668, -0.522)	121.98	232.00	35.24	257.17	1.61	-1.33	1.00	W
2010	Jan	30	0128	(-0.627, -0.682, 0.376)	128.81	151.12	53.77	313.30	1.31	-3.93	1.45	W
2010	Feb	10	2357	(-0.957, -0.011, 0.289)	163.17	92.19	60.39	412.03	2.13	1.82	2.83	W
2010	Feb	15	1739	(-0.791, -0.569, 0.228)	142.24	158.17	51.91	356.14	1.54	-3.57	1.76	W
2010	Mar	24	1204	(-0.738, 0.621, 0.264)	137.60	66.98	35.42	273.30	1.39	-1.55	1.20	W
2010	Apr	05	0754	(-0.987, -0.133, 0.093)	170.66	145.02	28.34	782.26	2.84	-0.12	2.16	A
2010	Apr	11	1220	(-0.903, -0.105, -0.416)	154.60	194.17	79.59	470.32	2.17	1.13	1.86	W
2010	Aug	03	1705	(-0.911, -0.108, 0.397)	155.69	105.16	71.83	555.74	2.18	-0.94	4.01	W
2010	Dec	19	2035	(-0.988, -0.134, 0.076)	171.11	150.43	18.18	398.86	2.41	0.13	1.18	W
2011	Feb	14	1506	(-0.908, -0.304, 0.287)	155.29	136.60	64.02	402.54	3.01	-1.28	3.71	W
2011	Feb	18	0049	(-0.792, 0.121, 0.598)	142.37	11.47	83.92	417.65	3.03	1.24	3.37	W
2011	Feb	20	1141	(-0.863, 0.004, 0.505)	149.64	0.44	72.04	499.53	1.49	-1.03	1.24	W
2011	Apr	18	0546	(-0.856, -0.044, 0.516)	148.83	94.93	23.35	359.16	2.60	0.93	3.40	W
2011	Jun	04	2006	(-0.817, -0.561, -0.130)	144.82	256.93	70.03	464.49	2.67	2.74	3.33	W
2011	Jul	06	0212	(-0.579, 0.237, 0.780)	125.38	16.87	88.72	315.34	1.54	-0.31	1.87	A
2011	Jul	11	0827	(-0.829, -0.298, 0.473)	146.00	122.19	85.89	564.57	2.05	0.33	2.48	W
2011	Aug	05	1732	(-0.951, -0.224, -0.215)	161.92	226.23	82.33	514.81	2.28	-0.65	2.09	W
2011	Sep	17	0257	(-0.938, -0.232, 0.259)	159.65	131.86	85.66	508.92	2.21	-2.16	2.52	W
2011	Sep	25	1046	(-0.530, -0.464, -0.710)	121.97	213.18	77.04	307.18	2.15	2.00	1.94	W
2011	Sep	26	1144	(-0.975, 0.179, -0.130)	167.23	324.11	51.43	517.37	2.50	-4.43	2.34	W
2011	Oct	05	0646	(-0.897, -0.176, 0.405)	153.79	113.47	80.60	483.19	1.64	2.49	2.37	W
2011	Oct	30	0840	(-0.832, -0.493, 0.254)	146.35	152.74	42.12	291.80	2.36	-0.45	2.32	W
2011	Nov	04	2027	(-0.760, 0.064, -0.646)	139.48	275.69	63.00	886.47	1.06	-2.79	7.09	W
2011	Nov	11	0301	(-0.993, -0.016, -0.118)	173.13	187.75	22.04	489.30	1.36	2.05	2.83	W
2011	Nov	28	2100	(-0.737, 0.608, -0.294)	137.48	334.17	64.43	499.74	2.05	-0.01	2.94	W
2011	Dec	18	1758	(-0.935, -0.324, 0.145)	159.22	155.86	73.03	318.67	1.63	-0.36	3.03	W
2011	Dec	28	1016	(-0.875, -0.480, 0.062)	151.03	172.70	80.24	282.61	1.57	0.41	1.70	W
2012	Jan	02	0112	(-0.638, -0.119, 0.761)	129.66	98.90	66.26	300.60	1.67	1.78	1.65	W
2012	Jan	21	0402	(-0.850, 0.526, 0.037)	148.19	85.93	82.03	329.18	1.58	-3.15	1.41	W
2012	Jan	22	0533	(-0.939, -0.292, -0.181)	159.90	238.29	86.08	445.90	2.00	11.15	1.98	W
2012	Jan	24	1440	(-0.881, -0.264, -0.393)	151.74	213.95	53.82	739.80	2.58	3.56	3.62	W
2012	Jan	30	1543	(-0.953, -0.298, 0.056)	162.38	169.36	35.03	370.47	3.05	0.73	1.25	W
2012	Mar	07	0328	(-0.879, -0.452, 0.154)	151.47	161.22	85.06	478.57	1.84	-3.24	1.78	W
2012	Mar	12	0841	(-0.895, -0.369, -0.252)	153.47	235.61	87.43	582.35	3.85	-3.96	2.35	A
2012	Apr	19	1713	(-0.936, 0.351, -0.012)	159.42	358.04	80.96	387.94	1.35	0.17	1.76	W
2012	May	20	0120	(-0.897, 0.387, 0.213)	153.76	61.17	15.28	445.26	1.85	-1.02	2.61	W
2012	May	21	1831	(-0.986, -0.013, -0.168)	170.29	184.59	60.88	413.57	2.69	1.05	2.55	W
2012	Jun	16	0903	(-0.977, 0.122, 0.175)	167.68	34.94	19.61	462.29	2.33	0.08	4.03	W
2012	Jun	16	1934	(-0.646, -0.109, 0.756)	130.22	98.19	27.09	345.52	1.77	2.35	1.61	W
2012	Jul	14	1739	(-0.971, 0.103, -0.217)	166.09	295.31	39.77	656.02	2.55	-2.57	3.57	W
2012	Sep	03	1121	(-0.961, -0.040, -0.272)	164.01	188.37	52.91	438.31	3.02	-0.18	2.34	W
2012	Sep	04	2202	(-0.893, -0.260, 0.367)	153.26	125.25	56.52	484.70	1.89	-1.04	1.03	W
2012	Sep	30	1014	(-0.403, -0.528, -0.747)	113.77	215.24	81.81	146.89	1.77	1.50	1.44	W
2012	Sep	30	2218	(-0.832, 0.550, 0.079)	146.28	81.86	63.55	424.31	2.10	-4.57	2.70	W
2012	Oct	08	0412	(-0.902, -0.396, -0.174)	154.36	246.26	82.74	446.71	1.87	-6.38	1.73	W
2012	Oct	31	1428	(-0.992, 0.111, 0.053)	172.95	64.59	83.01	396.25	2.11	-2.15	2.62	W
2012	Nov	12	2212	(-0.883, -0.460, -0.094)	151.96	258.43	76.87	390.34	2.19	-5.61	2.04	W
2012	Nov	23	2051	(-0.692, 0.405, -0.597)	133.79	304.14	76.21	364.90	2.41	-2.90	2.54	W
2012	Nov	26	0432	(-0.982, 0.082, 0.172)	169.04	25.46	46.97	608.88	1.84	1.99	2.90	W
2012	Dec	14	1851	(-0.550, -0.018, 0.835)	123.34	91.26	76.72	232.11	2.07	-0.47	1.09	A
2013	Jan	17	0023	(-0.875, -0.052, 0.482)	150.99	96.10	72.17	398.72	1.36	2.82	1.19	W
2013	Jan	19	1646	(-0.610, 0.787, 0.093)	127.62	83.29	14.22	345.80	2.94	1.79	1.77	A
2013	Feb	05	1246	(-0.665, -0.291, 0.688)	131.71	112.94	77.26	339.73	1.33	-0.27	1.87	W
2013	Feb	13	0047	(-0.378, 0.041, -0.925)	112.24	272.57	32.37	211.64	1.69	-0.62	1.36	W
2013	Feb	16	1121	(-0.986, 0.075, 0.150)	170.34	26.44	72.02	441.67	2.18	-0.93	1.79	W
2013	Mar	15	0433	(-0.699, -0.258, -0.667)	134.33	201.13	3.33	414.90	1.76	-2.79	2.88	W
2013	Mar	17	0521	(-0.992, -0.121, 0.027)	172.88	167.44	30.77	766.40	2.14	-1.11	5.60	W
2013	Apr	13	2213	(-0.710, 0.073, 0.701)	135.20	5.98	60.47	452.86	2.64	-0.29	3.14	W
2013	Apr	23	0329	(-0.944, -0.294, 0.153)	160.66	152.46	52.69	301.26	1.50	0.87	1.80	W
2013	Apr	30	0852	(-0.951, -0.077, 0.298)	162.08	104.41	72.02	436.06	1.63	-0.00	1.58	W
2013	May	18	0019	(-0.986, 0.131, -0.100)	170.48	322.60	70.67	494.98	1.67	-1.95	1.09	W

Y	M	D	UT	shock normal	θ_{x_n}	φ_{y_n}	θ_{B_n}	v_s	X	B_z	Ms	SAT
2013	May	19	2131	(-0.718, -0.420, -0.555)	135.92	217.14	49.16	423.79	2.14	-0.55	2.28	W
2013	May	24	1726	(-0.796, 0.476, -0.373)	142.79	321.89	57.48	561.01	2.80	-1.68	3.39	W
2013	May	25	0921	(-0.707, -0.674, -0.216)	134.96	252.21	73.44	555.22	2.16	0.87	2.27	W
2013	May	31	1511	(-0.883, 0.406, -0.237)	151.95	329.79	79.76	405.14	1.85	1.08	2.24	W
2013	Jun	10	0252	(-0.947, -0.057, 0.317)	161.21	100.13	84.28	374.50	1.74	-3.32	1.02	W
2013	Jun	19	2214	(-0.887, -0.174, -0.427)	152.54	202.18	73.59	315.28	1.48	-4.32	1.11	W
2013	Jun	27	1351	(-0.852, 0.503, 0.148)	148.38	73.65	69.98	450.27	2.64	-0.47	2.22	W
2013	Jul	09	2011	(-0.918, -0.181, -0.352)	156.70	207.26	69.84	514.70	1.41	7.79	1.89	W
2013	Jul	12	1643	(-0.650, -0.073, -0.757)	130.52	185.49	77.16	473.08	1.64	1.34	2.36	W
2013	Jul	18	1255	(-0.891, 0.078, -0.447)	153.04	279.95	76.30	550.51	1.39	-1.26	2.15	W
2013	Sep	02	0156	(-0.901, 0.098, -0.424)	154.24	282.99	84.50	553.19	1.59	0.23	1.72	W
2013	Oct	02	0115	(-1.000, -0.010, 0.009)	179.22	140.08	39.24	689.99	2.55	-1.76	4.62	W
2013	Oct	29	0933	(-0.846, -0.532, 0.043)	147.73	175.40	56.33	385.93	1.57	-4.78	1.58	W
2013	Dec	13	1232	(-0.830, -0.558, -0.013)	146.09	268.62	53.47	310.57	2.43	0.46	2.50	W

[1]In sequence, the columns indicate: Y, year; M, month; D, day; UT, universal time; n_x, X component of shock normal; n_y, Y component of shock normal; n_z, Z component of shock normal; θ_{x_n} , shock impact angle; φ_{y_n} , clock angle; θ_{B_n} , obliquity, angle between the upstream magnetic field vector and shock normal; v_s, shock speed, in km/s; X, compression ratio; B_z, z component of IMF prior to 1.5h before shock impact, Ms, fast magnetosonic Mach number; and SAT, spacecraft name, (A)CE and (W)IND.

Bibliography

Abraham-Shrauner, B. (1972), Determination of magnetohydronamic shock normals, *J. Geophys. Res.*, *77*(4), doi:10.1029/JA077i004p00736.

Abraham-Shrauner, B., and S. H. Yun (1976), Interplanetary shocks seen by Ames Plasma Probe on Pioneer 6 and 7, *J. Geophys. Res.*, *81*(13), doi:10.1029/JA081i013p02097.

Ahn, B.-H., H. W. Kroehl, Y. Kamide, and E. A. Kihn (2000), Universal time variations of the auroral electrojet indices, *J. Geophys. Res.*, *105*(A1), 267–275, doi:10.1029/1999JA900364.

Akasofu, S.-I. (1964), The development of the auroral substorm, *Planet. Space Sci.*, *12*(4), 273–282, doi:10.1016/0032-0633(64)90151-5.

Akasofu, S.-I., and J. Chao (1980), Interplanetary shock waves and magnetospheric substorms, *Planet. Space Sci.*, *28*(4), 381–385, doi:10.1016/0032-0633(80)90042-2.

Alfvén, H. (1942), Existence of electromagnetic–hydrodynamic waves, *Nature*, *150*, 405–406, doi:10.1038/150405d0.

Axford, W. I. (1962), The interaction between the solar wind and the earth's magnetosphere, *J. Geophys. Res.*, *67*(10), 3791–3796, doi:10.1029/JZ067i010p03791.

Balogh, A., and R. A. Treumann (2013), *Physics of Collisionless Shocks*, Springer, New York.

Bargatze, L. F., D. N. Baker, R. L. McPherron, and E. W. H. Jr. (1985), Magnetospheric impulse response for many levels of geomagnetic activity, *J. Geophys. Res.*, *90*(A7), 6387–6394, doi:10.1029/JA090iA07p06387.

Bartels, J. (1949), The standardized index, Ks, and the planetary index, Kp, *Int. Union Geod. Geophys. IATME Bull.*, *97*(12b).

Baumjohann, W., and R. Treumann (2009), *Basic Space Plasma Physics*, Imperial College Press, London, United Kingdom.

Bavassano, B., F. Mariani, and N. F. Ness (1973), Pioneer 8 observations and interpretations of sixteen interplanetary shock waves observed in 1968, *J. Geophys. Res.*, *78*(22), 4535–4546, doi:10.1029/JA078i022p04535.

Berdichevsky, D. B., A. Szabo, R. P. Lepping, A. F. Viñas, and F. Mariani (2000), Interplanetary fast shocks and associated drivers observed through the 23rd solar minimum by Wind over its first 2.5 years, *J. Geophys. Res.*, *105*(A12), 27,289 27,314, doi:10.1029/1999JA000367.

Biermann, L. (1957), Solar corpuscular radiation and the interplanetary gas, *Observatory*, *77*, 109–110.

Bolduc, L. (2002), GIC observations and studies in the Hydro-Québec power system, *J. Atmos. Sol. Terr. Phys.*, *64*(16), 1793–1802, doi:10.1016/S1364-6826(02)00128-1.

Borrini, G., J. T. Gosling, S. J. Bame, and W. C. Feldman (1982), An analysis of shock wave disturbances observed at 1 AU from 1971 through 1978, *J. Geophys. Res.*, *87*(A6), 4365–4373, doi:10.1029/JA087iA06p04365.

Boyd, T. J. M., and J. J. Sanderson (1969), *Plasma Dynamics*, Barnes & Noble, New York.

Boyd, T. J. M., and J. J. Sanderson (2003), *The Physics of Plasmas*, Cambridge University Press, Cambridge, United Kingdom.

Buffett, B. A. (2000), Dynamics of the Earth's core, in *Earth's Deep Interior: Mineral Physics and Tomography From the Atomic to the Global Scale*, edited by S. ichiro Karato, A. Forte, R. Liebermann, G. Masters, and L. Stixrude, pp. 37–62, American Geophysical Union, Washington, D.C., doi:10.1029/GM117p0037.

Burch, J. L. (1972), Preconditions for the triggering of polar magnetic substorms by storm sudden commencements, *J. Geophys. Res.*, *77*(28), 5629–5632, doi:10.1029/JA077i028p05629.

Burguess, D. (1995), Collisionless shocks, in *Introduction to Space Plasma Physics*, edited by M. G. Kivelson and C. T. Russell, Cambridge University Press, Cambridge, United Kingdom, Chapter 5.

Burlaga, L., R. Lepping, R. Weber, T. Armstrong, C. Goodrich, J. Sullivan, D. Gurnett, P. Kellogg, E. Keppler, F. Mariani, F. Neubauer, H. Rosenbauer, and R. Schwenn (1980), Interplanetary particles and fields, November 22 to December 6, 1977: Helios, Voyager, and IMP observations between 0.6 and 1.6 au, *J. Geophys. Res.*, *85*(A5), 2227–2242, doi:10.1029/JA085iA05p02227.

Burlaga, L. F. (1971), Hydromagnetic waves and discontinuities in the solar wind, *Space Sci. Rev.*, *12*(5), 600–657, doi:10.1007/BF00173345.

Burlaga, L. F. (1995), *Interplanetary Magnetohydrodynamics*, Oxford University Press, New York.

Burlaga, L. F., and J. K. Chao (1971), Reverse and forward slow shocks in the solar wind, *J. Geophys. Res.*, *76*(31), 7516–7521, doi:10.1029/JA076i031p07516.

Burlaga, L. F., N. F. Ness, and E. C. Stone (2013), Magnetic field observations as Voyager 1 entered the heliosheath depletion region, *Science*, *341*(6142), 147–150, doi:10.1126/science.1235451.

Cahill, L. J., and P. Amazeen (1963), The boundary of the geomagnetic field., *J. Geophys. Res.*, *68*(7), 1835–1843, doi:10.1029/JZ068i007p01835.

Chao, J., and K. Hsieh (1984), On determining magnetohydrodynamic shock parameters θ_{B_n} and M_A, *Planet. Space Sci.*, *32*(5), 641–646, doi:10.1016/0032-0633(84)90115-6.

Chao, J. K., and R. P. Lepping (1974), A correlative study of SSC's, interplanetary shocks, and solar activity, *J. Geophys. Res.*, *79*(13), 1799–1807, doi:10.1029/JA079i013p01799.

Chao, J. K., and S. Olbert (1970), Observation of slow shocks in interplanetary space, *J. Geophys. Res.*, *75*(31), 6394–6397, doi:10.1029/JA075i031p06394.

Chapman, S., and J. Bartels (1940), *Geomagnetism*, Oxford Univ. Press, London, United

Kingdom.

Chapman, S., and V. C. A. Ferraro (1930), A new theory of magnetic storms, *Nature*, *126*, 129–130, doi:10.1038/126129a0.

Chapman, S., and V. C. A. Ferraro (1931a), A new theory of magnetic storms, *Terr. Magn. Atmos. Electr*, *36*(2), 77–97, doi:10.1029/TE036i002p00077.

Chapman, S., and V. C. A. Ferraro (1931b), A new theory of magnetic storms (continued), *Terr. Magn. Atmos. Electr*, *36*(2), 171–186, doi:10.1029/TE036i003p00171.

Chapman, S., and V. C. A. Ferraro (1932), A new theory of magnetic storms (continued), *Terr. Magn. Atmos. Electr*, *37*(2), 147–156, doi:10.1029/TE037i002p00147.

Colburn, D. S., and C. P. Sonett (1966), Discontinuities in the solar wind, *Space Sci. Rev.*, *439*(A11), 506, doi:10.1007/BF00240575.

Connor, H. K., E. Zesta, D. M. Ober, and J. Raeder (2014), The relation between transpolar potential and reconnection rates during sudden enhancement of solar wind dynamic pressure: OpenGGCM–CTIM results, *J. Geophys. Res.*, *119*(5), 3411–3429, doi:10.1002/2013JA019728.

Craven, J. D., L. A. Frank, C. T. Russell, E. E. Smith, and R. P. Lepping (1986), Global auroral responses to magnetospheric compressions by shocks in the solar wind: Two case studies, in *Solar Wind-Magnetosphere Coupling*, edited by Y. Kamide and J. A. Slavin, pp. 367–380, Terra Scientific, Tokyo, Japan.

Davis, T. N., and M. Sugiura (1966), Auroral electrojet activity index AE and its universal time variations, *J. Geophys. Res.*, *71*(3), 785–801, doi:10.1029/JZ071i003p00785.

de Hoffmann, F., and E. Teller (1950), Magneto-hydrodynamic shocks, *Phys. Rev.*, *80*(4), doi:10.1103/PhysRev.80.692.

Dungey, J. W. (1961), Interplanetary magnetic field and the auroral zones, *Phys. Rev. Lett.*, *6*(2), 47–48, doi:10.1103/PhysRevLett.6.47.

Dungey, J. W. (1963), The structure of the exosphere or adventures in velocity space, in *Geophysics: The Earth's Environment*, edited by C. Dewitt, J. Hieblot, and A. Lebeau, pp. 505–550, Gordon and Breach, New York.

Eastwood, J. P., H. Hietala, G. Toth, T. D. Phan, and M. Fujimoto (2014), What controls the structure and dynamics of Earth's magnetosphere?, *Space Sci. Rev.*, pp. 1–36, doi:10.1007/s11214-014-0050-x.

Echer, E., W. D. Gonzalez, L. E. A. Vieira, A. D. L. F. L. Guarnieri, A. Prestes, A. L. C. Gonzalez, and N. J. Schuch (2003), Interplanetary shock parameters during solar activity maximum (2000) and minimum (1995-1996), *Braz. Jour. Phys.*, *33*(1), 2301, doi:10.1590/S0103-97332003000100010.

Echer, E., M. V. Alves, and W. D. Gonzalez (2004), Geoefectiveness of interplanetary shocks during solar minimum (1995) and solar maximum (2000), *Solar Phys.*, *221*, 361–380, doi:10.1023/B:SOLA.0000035045.65224.f3.

Echer, E., B. Tsurutani, F. Guarnieri, and J. Kozyra (2011), Interplanetary fast forward shocks and their geomagnetic effects: CAWSES events, *J. Atmos. Sol. Terr. Phys.*, *73*(11-12), 1330–1338, doi:10.1016/j.jastp.2010.09.020.

Eddy, J. A. (1976), The maunder minimum, *Science*, *192*(4245), 1189–1202, doi:10.1126/science.192.4245.1189.

Edmiston, J. P., and C. F. Kennel (1984), A parametric survey of the first critical Mach number for a fast MHD shock, *J. Plasma Phys.*, *32*(3), 429–441, doi:10.1017/S002237780000218X.

Fuller-Rowell, T. J., D. Rees, S. Quegan, R. J. Moffet, M. V. Codrescu, and G. H. Millward (1996), A coupled thermosphere-ionosphere model (CTIM), in *STEP Report*, edited by R. W. Schunk, p. 217, Scientific Commitee on Solar Terrestrial Physics (SCOSTEP), NOAA/NGDC, Boulder, Colorado.

Ge, Y. S., J. Raeder, V. Angelopoulos, M. L. Gilson, and A. Runov (2011), Interaction of dipolarization fronts within multiple bursty bulk flows in global MHD simulations of a substorm on 27 February 2009, *J. Geophys. Res.*, *116*, A00I23, doi:10.1029/2010JA015758.

Gilbert, W. (1600), *De Magnete*, (Translated from Latin by P. Fleury Mottelay in 1893, first published in 1893), Dover Publications, New York.

Gilson, M. L. (2011), Global structure of the nightside proton precipitation during substorms using simulations and observations, Ph.D. thesis, University of New Hampshire.

Gilson, M. L., J. Raeder, E. Donovan, Y. S. Ge, and L. Kepko (2012), Global simulation of proton precipitation due to field line curvature during substorms, *J. Geophys. Res.*, *117*(A5), doi:10.1029/2012JA017562.

Gjerloev, J. W. (2009), A global ground-based magnetometer initiative, *Eos Trans. AGU*, *90*(27), 230–231, doi:10.1029/2009EO270002.

Gjerloev, J. W. (2012), The SuperMAG data processing technique, *J. Geophys. Res.*, *117*(A9), doi:10.1029/2012JA017683.

Gjerloev, J. W., R. A. Hoffman, M. M. Friel, L. A. Frank, and J. B. Sigwarth (2004), Substorm behavior of the auroral electrojet indices, *Ann. Geophys.*, *22*(6), 2135–2149, doi:10.5194/angeo-22-2135-2004.

Gloecker, G., and L. A. Fisk (2014), A test for whether or not Voyager 1 has crossed the heliopause, *Geophys. Res. Lett.*, *41*(15), 5325–5330, doi:10.1002/2014GL060781.

Gold, T. (1955), Discussion on shock waves and rarefied gases, in *Gas Dynamics of Cosmic Clouds*, North Holland Publ. Co., Amsterdan, the Netherlands.

Gold, T. (1959), Motions in the magnetosphere of the Earth, *J. Geophys. Res.*, *64*(9), 1219–1224, doi:10.1029/JZ064i009p01219.

Gonzalez, W. D., J. A. Joselyn, Y. Kamide, H. W. Kroehl, G. Rostoker, B. T. Tsurutani, and V. M. Vasyliunas (1994), What is a geomagnetic storm?, *J. Geophys. Res.*, *99*(A4), 5771–5792, doi:10.1029/93JA02867.

Grib, S. A., and E. A. Pushkar (2006), Asymetry of nonlinear interactions of solar MHD discontinuities with the bow shock, *Geomagnetism and Aeronomy*, *46*(4), 417–423, doi:doi:10.1134/S0016793206040025.

Grygorov, K., L. Přech, J. Šafránková, Z. Němeček, and O. Goncharov (2014), The far magnetotail response to an interplanetary shock arrival, *Planet. Space Sci.*, doi:10.1016/j.pss.2014.07.016.

Guo, X.-C., and Y.-Q. Hu (2007), Response of Earth's ionosphere to interplanetary shocks, *Chinese J. Geophys*, *50*(4), 817–823, doi:10.1002/cjg2.1099.

Guo, X.-C., Y.-Q. Hu, and C. Wang (2005), Earth's magnetosphere impinged by interplanetary shocks of different orientations, *Chinese Phys. Lett.*, *22*(12), 3221–3224, doi:10.1088/0256-307X/22/12/067.

Gurnett, D. A., and A. Bhattacharjee (2005), *Introduction to Plasma Physics With Space and Laboratory Applications*, Cambridge University Press, Cambridge, United Kingdom.

Hada, T., and C. F. Kennel (1985), Nonlinear evolution of slow waves in the solar wind, *J. Geophys. Res.*, *90*(A1), 531–535, doi:10.1029/JA090iA01p00531.

Heinemann, M. A., and G. L. Siscoe (1974), Siscoe, shapes of strong shock fronts in an inhomogeneous solar wind, *J. Geophys. Res.*, *79*(10), 1349–1355, doi:10.1029/JA079i010p01349.

Hsieh, W.-C., J.-H. Shue, J.-K. Chao, T.-C. Tsai, Z. Němeček, and J. Šafránková (2014), Possible observational evidence of contact discontinuities, *Geophys. Res. Lett.*, *41*(22), doi:10.1002/2014GL062342.

Hudson, M. K., S. R. Elkington, J. G. Lyon, V. A. Marchenko, I. Roth, M. Temerin, J. B. Blake, M. S. Gussenhoven, and J. R. Wygant (1997), Simulations of radiation belt formation during storm sudden commencements, *J. Geophys. Res.*, *102*(A7), 14,087–14,102, doi:10.1029/97JA03995.

Hughes, W. J. (1994), Magnetospheric ULF waves: A tutorial with a historical perspective, in *Solar Wind Sources of Magnetospheric Ultra-Low-Frequency Waves*, edited by M. J. Engebretson, K. Takahashi, and M. Scholer, American Geophysical Union, Washington D.C., doi:10.1029/GM081p0001.

Hundhaunsen, A. J. (1972a), *Coronal Expansion and Solar Wind*, Springer Berlin Heidelberg, New York.

Hundhaunsen, A. J. (1972b), Interplanetary shock waves and the structure of solar wind disturbances, in *Solar Wind*, edited by C. P. Sonett, P. J. Coleman Jr., , and J. M. Wilcox, p. 393, NASA Spec. Publ., Washington, D.C.

Hundhaunsen, A. J. (1979), Solar activity and the solar wind, *Rev. Geophys.*, *17*(8), 2034–2048, doi:10.1029/RG017i008p02034.

Hundhausen, A. J., and R. A. Gentry (1969), Numerical simulation of flare-generated disturbances in the solar wind, *J. Geophys. Res.*, *74*(11), 2908–2918, doi:10.1029/JA074i011p02908.

Ivanov, K. G. (1971), Rotational discontinuities in the solar wind, *Geomagnetism and Aeronomia*, *11*, 767–770.

Jackson, J. D. (1999), *Classical Electrodynamics*, John Wiley &, Inc., Hoboken, Third Edition.

Jacobs, L. A. (1984), *Reversals of the Earth's Magnetic Field*, University of Cambridge Press, Cambridge.

Jeffrey, A., and T. Taniuti (1964), *Nonlinear Wave Propagation*, Academic Press, New York.

Jian, L., C. Russell, J. Luhmann, and R. Skoug (2006a), Properties of stream interactions at one AU during 1995-2004, *Solar Phys.*, *239*(1-2), 337–392, doi:10.1007/s11207-006-0132-3.

Jian, L., C. Russell, J. Luhmann, and R. Skoug (2006b), Properties of interplanetary coronal mass ejections at one AU during 1995-2004, *Solar Phys.*, *239*(1-2), 393–436, doi:10.1007/s11207-006-0133-2.

Jurac, S., J. C. Kasper, J. D. Richardson, and A. J. Lazarus (2002), Geomagnetic disturbances and their relationship to interplanetary shock parameters, *Geophys. Res. Lett.*, *29*(10), doi:10.1029/2001GL014034.

Kamide, Y. (2005), What determines the intensity of magnetospheric substorms?, in *Multiscale Coupling of Sun-Earth Processes*, edited by A. Lui, Y. Kamide, and G. Consolini, pp. 175–194, Elsevier Science B.V., Amsterdam, doi:10.1016/B978-044451881-1/50014-9.

Kamide, Y., B.-H. Ahn, S.-I. Akasofu, W. Baumjohann, E. Friis-Christensen, H. W. Kroehl, H. Maurer, A. D. Richmond, G. Rostoker, R. W. Spiro, J. K. Walker, and A. N. Zaitzev (1982), Global distribution of ionospheric and field–aligned currents during substorms as determined from six IMS meridian chains of magnetometers: Initial results, *J. Geophys. Res.*, *87*(A10), 8228–8240, doi:10.1029/JA087iA10p08228.

Kappenman, J. (2010), Geomagnetic storms and their impacts on the US power grid, *Tech. rep.*, Metatech Corp., Goleta, California.

Kawasaki, K., S.-I. Akasofu, F. Yasuhara, and C.-I. Meng (1971), Storm sudden commencements and polar magnetic substorms, *J. Geophys. Res.*, *76*, 6781–6789, doi:10.1029/JA076i028p06781.

Kellog, P. J. (1962), Flow of plasma around the Earth, *J. Geophys. Res.*, *67*, 3805–3811, doi:10.1029/JZ067i010p03805.

Kennel, C. F. (1987), Critical Mach numbers in classical magnetohydrodynamics, *J. Geophys. Res.*, *92*(A12), 13,427–13,437, doi:10.1029/JA092iA12p13427.

Kennel, C. F., J. P. Edmiston, and T. Hada (1985), A quarter century of collisionless shock research, in *Collisionless Shocks in the Heliosphere: A Tutorial Review*, edited by R. G. Stone and B. Tsurutani, American Geophysical Union, Washington, D.C., doi:10.1029/GM034p0001.

Kivelson, M. G., and C. T. Russell (1996), *Introduction to Space Physics*, Cambridge University Press, Cambridge.

Kokubun, S., R. L. McPherron, and C. T. Russell (1977), Triggering of substorms by solar wind discontinuities, *J. Geophys. Res.*, *82*(1), 74–86, doi:10.1029/JA082i001p00074.

Koval, A., and A. Szabo (2010), Multispacecraft observations of interplanetary shock shapes on the scales of the Earth's magnetosphere, *J. Geophys. Res.*, *115*(A12105), doi:10.1029/2010JA015373.

Koval, A., J. Šafránková, Z. Němeček, A. A. Samsonov, L. Přech, and J. D. Richardson (2006), Interplanetary shock in the magnetosheath: Comparison of experimental data with MHD modeling, *Geophys. Res. Lett.*, *33*(L1102), doi:10.1029/2006GL025707.

Krimigis, S. M., R. B. Decker, E. C. Roelof, M. E. Hill, T. P. Armstrong, G. Gloeckler, D. C. Hamilton, and L. J. Lanzerotti (2013), Search for the exit: Voyager 1 at heliospheres border with the galaxy, *Science*, *341*(6142), 144–147, doi:10.1126/science.1235721.

Lakhina, G. S., B. T. Tsurutani, and X.-Y. Zhou (2001), Excitation of plasma instabilities in the Earth's magnetotail by interplanetary shocks, *Adv. Space Res.*, in press, COSPAR-00.

Landau, L. D., and E. M. Lifshitz (1960), *Electrodynamics of Continuous Media*, Pergamon Press, New York.

Lee, M. A. (1983), Coupled hydromagnetic wave excitation and ion acceleration at interplanetary traveling shocks, *J. Geophys. Res.*, *88*(A8), 6109–6119, doi:10.1029/JA088iA08p06109.

Lepping, R., M. Acuña, L. Burlaga, W. Farrell, J. Slavin, K. Schatten, F. Mariani, N. Ness, F. Neubauer, Y. Whang, J. Byrnes, R. Kennon, P. Panetta, J. Scheifele, and E. Worley (1995), The WIND Magnetic Field Investigation, *Space Sci. Rev.*, *71*(1–4), 207–229, doi:10.1007/BF00751330.

Lepping, R. P., and P. D. Argentiero (1971), Single spacecraft method of estimating shock normals, *J. Geophys. Res.*, *76*(19), 4349–4359, doi:10.1029/JA076i019p04349.

Leroy, M. M., C. C. Goodrich, D. Winske, C. S. Wu, and K. Papadopoulos (1981), Simulation of a perpendicular bow shock, *Geophys. Res. Lett.*, *8*(12), 1269–1272, doi:10.1029/GL008i012p01269.

Livesey, W. A., C. F. Kennel, and C. T. Russell (1982), ISEE–1 and –2 observations of magnetic field strength overshoots in quasi–perpendicular bow shocks, *Geophys. Res. Lett.*, *9*(9), 1037–1040, doi:10.1029/GL009i009p01037.

Luhmann, J. G., T.-L. Zhang, S. M. Petrinec, C. T. Russell, P. Gazis, and A. Barnes (1993), Solar cycle 21 effects on the interplanetary magnetic field and related parameters at 0.7 and 1.0 AU, *J. Geophys. Res.*, *98*(A4), 5559–5572, doi:10.1029/92JA02235.

Lui, A. T. Y., R. E. Lopez, S. M. Krimigis, R. W. McEntire, L. J. Zanetti, and T. A. Potemra (1988), A case study of magnetotail current sheet disruption and diversion, *Geophys. Res. Lett.*, *15*(7), 721–724, doi:10.1029/GL015i007p00721.

Lui, A. T. Y., A. Mankofsky, C.-L. Chang, K. Papadopoulos, and C. S. Wu (1990), A current disruption mechanism in the neutral sheet: A possible trigger for substorm expansions, *J. Geophys. Res.*, *17*(6), 745–748, doi:10.1029/GL017i006p00745.

Lyons, L. R. (1995), A new theory for magnetospheric substorms, *J. Geophys. Res.*, *100*(A10), 19,069–19,081, doi:10.1029/95JA01344.

Lyons, L. R. (1996), Substorms: Fundamental observational features, distinction from other disturbances, and external triggering, *J. Geophys. Res.*, *101*(A6), 13,011–13,025, doi:10.1029/95JA01987.

Manchester, W., A. Ridley, T. Gombosi, and D. DeZeeuw (2006), Modeling the Sun-to-Earth propagation of a very fast CME, *Adv. Space Res.*, *38*(2), 253–262, doi:10.1016/j.asr.2005.09.044.

Marsch, E. (2006), Kinetic physics of the solar corona and solar wind, *Living Rev. in Solar Phys.*, *3*(1), doi:10.12942/lrsp-2006-1.

Mayaud, P. N. (1980), The AU, AL and AE indices, in *Derivation, meaning and use of geomagnetic indices*, vol. 22, American Geophysical Union, Washington, D.C., doi:10.1029/GM022, chapter 7.

McComas, D., S. Bame, P. Barker, W. Feldman, J. Phillips, P. Riley, and J. Griffee (1998), Solar Wind Electron Proton Alpha Monitor (SWEPAM) for the Advanced Composition Explorer, *Space Sci. Rev.*, *86*(1–4), 563–612, doi:10.1023/A:1005040232597.

McComas, D., H. Elliott, N. Schwadron, J. Gosling, R. Skoug, and B. Goldstein (2003), The three–dimensional solar wind around solar maximum, *Geophys. Res. Lett.*, *30*(10), doi:10.1029/2003GL017136.

McPherron, M. L. (1991), Physical processes producing magnetospheric substorms and magnetic storms, in *Geomagnetism, Volume 4*, edited by J. Jacobs, Academic Press Ltd., Landing, Chapter 7.

Ness, N. F., C. S. Scearce, and J. B. Seek (1964), Initial results of the IMP-1 magnetic field experiment, *J. Geophys. Res.*, *69*(17), 3531–3569, doi:10.1029/JZ069i017p03531.

Neugebauer, M., and C. W. Snyder (1962), Solar plasma experiment, *Science*, *138*(3545), 1095–1097, doi:10.1126/science.138.3545.1095-a.

Newbury, J. A. (2000), Plasma heating and thermal transport in the solar wind near 1 AU, Ph.D. thesis, University of California, Los Angeles.

Newell, P. T., and G. W. Gjerloev (2012), SuperMAG-based partial ring current indices, *J. Geophys. Res.*, *117*(A5), doi:10.1029/2012JA017586.

Newell, P. T., and J. W. Gjerloev (2011a), Evaluation of SuperMAG auroral electrojet indices as indicators of substorms and auroral power, *J. Geophys. Res.*, *116*(A12), doi:10.1029/2011JA016779.

Newell, P. T., and J. W. Gjerloev (2011b), Substorm and magnetosphere characteristic scales inferred from the SuperMAG auroral electrojet indices, *J. Geophys. Res.*, *116*(A12), doi:10.1029/2011JA016936.

Newell, P. T., and J. W. Gjerloev (2014), Local geomagnetic indices and the prediction of auroral power, *J. Geophys. Res.*, *119*(12), 9790–9803, doi:10.1002/2014JA020524.

Ogilvie, K., D. Chornay, R. Fritzenreiter, F. Hunsaker, J. Keller, J. Lobell, G. Miller, J. Scudder, J. Sittler, E.C., R. Torbert, D. Bodet, G. Needell, A. Lazarus, J. Steinberg,

J. Tappan, A. Mavretic, and E. Gergin (1995), SWE, a comprehensive plasma instrument for the WIND spacecraft, *Space Sci. Rev.*, *71*(1–4), 55–77, doi:10.1007/BF00751326.

Oliveira, D. M., and J. Raeder (2014), Impact angle control of interplanetary shock geoeffectiveness, *J. Geophys. Res.*, *119*(10), 8188–8201, doi:10.1002/2014JA020275.

Oliveira, D. M., and J. Raeder (2015), Impact angle control of interplanetary shock geoeffectiveness: A statistical study, *J. Geophys. Res.*, under review.

Oliveira, D. M., J. Raeder, B. T. Tsurutani, and J. W. Gjerloev (2015), Effects of interplanetary shock inclinations on auroral power intensity, *J. Atmos. Sol. Terr. Phys.*, in process of submission.

Papadopoulos, K. (1979), The role of microturbulence on collisionless reconnection, in *Dynamics of the Magnetosphere*, vol. 78, edited by S.-I. Akasofu, pp. 289–309, Springer Netherlands, Amsterdam, The Netherlands, doi:10.1007/978-94-009-9519-214.

Parker, E. N. (1958), Dynamics of the interplanetary gas and magnetic fields, *Astrophys. J.*, *128*, 664, doi:10.1086/146579.

Parker, E. N. (1961), Sudden expansion of the corona following a large solar flare and the attendant magnetic field and cosmic ray effects, *Astron. J.*, *133*, 1014–1033, doi:10.1086/147105.

Parker, E. N. (1963), *Interplanetary Dynamic Processes*, Intersicence.

Parks, G. K. (2004), *Physics of Space Plasmas*, Westview Press, Boulder, CO.

Paschmann, G., Schwartz, S., C. Escoubet, and S. Haaland (Eds.) (2005), *Outer Magnetospheric Boundaries: Cluster Results*, vol. 20, Springer Netherlands, Amsterdam, The Netherlands, doi:10.1007/1-4020-4582-4.

Pizzo, V. (1978), A three-dimensional model of corotating streams in the solar wind, 1. Theoretical foundations, *J. Geophys. Res.*, *83*(A12), 5563–5572, doi:10.1029/JA083iA12p05563.

Pizzo, V. J. (1991), The evolution of corotating stream fronts near the ecliptic plane in the inner solar system: 2. Three-dimensional tilted-dipole fronts, *J. Geophys. Res.*, *96*(A4), 5405–5420, doi:10.1029/91JA00155.

Priest, E. F. (1981), *Solar Magnetohydrodynamics*, D. Reidel Publishing, Holland.

Pulkkinen, A., K. Kuznetsova, A. Ridley, J. Raeder, A. Vapirev, D. Weimer, R. S. Weigel, M. Wiltberger, G. Millward, L. Rastätter, M. Hesse, H. J. Singer, and A. Chulaki (2011), Geospace environment modeling 2008-2009 challenge: Ground magnetic field perturbations, *J. Geophys. Res.*, *9*, doi:10.1029/2010SW000600.

Pulkkinen, A., L. Rastatter, M. Kuznetsova, H. Singer, C. Balch, D. Weimer, G. Toth, A. Ridley, T. Gombosi, M. Wiltberger, J. Raeder, and R. Weigel (2013), Community-wide validation of geospace model ground magnetic field perturbation predictions to support model transition to operations, *Space Weather*, *11*, 369, doi:10.1002/swe.20056.

Přech, L., Z. Němeček, and J. Šafrnková (2008), Response of magnetospheric boundaries to the interplanetary shock: THEMIS contribution, *Geophys. Res. Lett.*, *35*(17), doi:10.1029/2008GL033593.

Raeder, J. (2003), Global Magnetohydrodynamics: A Tutorial Review, in *Space Plasma Simulation*, edited by J. Buchner, C. T. Dum, and M. Scholer, pp. 1–19, Springer Verlag, Berlin Heilderberg, New York, doi:10.1007/3-540-36530-311.

Raeder, J., and G. Lu (2005), Polar cap potential saturation during large geomagnetic storms, *Adv. Space Res.*, *36*(1804), doi:10.1016/j.asr.2004.05.010.

Raeder, J., J. Berchem, and M. Ashour-Abdalla (1998), The Geospace Environment Modeling Grand Challenge: Results from a Global Geospace Circulation Model, *J. Geophys. Res.*, *103*(A7), 14,787–14,797, doi:10.1029/98JA00014.

Raeder, J., Y. Wang, and T. J. Fuller-Rowell (2001a), Geomagnetic storm simulation with a Coupled Magnetosphere-Ionosphere-Thermosphere model, in *Space Weather*, edited by P. Song and H. J. Siscoe, pp. 377–384, American Geophysical Union, Washington, D.C., doi:10.1029/GM125p0377.

Raeder, J., R. L. McPherron, L. A. Frank, S. Kokubun, G. Lu, T. Mukai, W. R. Paterson, J. B. Sigwarth, H. J. Singer, and J. A. Slavin (2001b), Global simulation of the Geospace Environment Modeling substorm challenge event, *J. Geophys. Res.*, *106*(A1), 381–395, doi:10.1029/2000JA000605.

Raeder, J., D. Larson, W. Li, E. L. Kepko, and T. Fuller-Rowell (2008), OpenGGCM simulations for the THEMIS mission, *Space Sci. Rev.*, *141*, 535–555, doi:10.1007/978-0-387-89820-9-22.

Raeder, J., P. Zhu, Y. Ge, and G. Siscoe (2013), Auroral signatures of ballooning mode near substorm onset: OpenGGCM simulations, in *Auroral Phenomenology and Magnetospheric Processes: Earth And Other Planets*, vol. 197, edited by A. Keiling, E. Donovan, and T. Karlson, pp. 389–396, American Geophysical Union, Washington, D.C., doi:10.1029/2011GM001200.

Rastätter, L., M. M. Kuznetsova, A. Glocer, D. Welling, X. Meng, J. Raeder, M. Wiltberger, V. K. Jordanova, Y. Yu, S. Zaharia, R. S. Weigel, S. Sazykin, R. Boynton, H. Wei, V. Eccles, W. Horton, M. L. Mays, and J. Gannon (2013), Geospace Environment Modeling 2008-2009 challenge: Dst index, *Space Weather*, *11*, 187, doi:10.1002/swe.20036.

Rastogi, R. G. (1999), Signatures of storm sudden commencements in geomagnetic H, Y and Z fields at Indian observatories during 1958-1992, *Adv. Space Res.*, *17*, 1426–1438, doi:10.1007/s00585-999-1426-1.

Richardson, I. G., and H. V. Cane (2010), Interplanetary circumstances of quasi-perpendicular interplanetary shocks in 1996-2005, *J. Geophys. Res.*, *115*(A7), doi:10.1029/2009JA015039.

Richter, A. K., K. C. Hsieh, A. H. Luttrell, E. Marsch, and R. Schwenn (1985), Review of interplanetary shock phenomena near and within 1 AU, in *Collisionless Shocks in the Heliosphere: Reviews of Current Research*, edited by B. T. Tsurutani and R. G. Stone, pp. 33–50, American Geophysical Union, Washington, D.C., doi:10.1029/GM035p0033.

Ridley, A. J., D. L. De Zeeuw, W. B. Manchester, and K. C. Hansen (2006), The magnetospheric and ionospheric response to a very strong interplanetary shock and coronal mass ejection, *Adv. Space Res.*, *38*, 263–272, doi:10.1016/j.asr.2006.06.010.

Rostoker, G. (1972), Geomagnetic indices, *Rev. Geophys.*, *10*(4), 935–950, doi:10.1029/RG010i004p00935.

Russell, C. T. (1985), Planetary bow shocks, in *Collisionless Shocks in the Heliosphere: Reviews of Current Research*, edited by B. T. Tsurutani and R. G. Stone, American Geophysical Union, Washington, D.C., doi:10.1029/GM035p0109.

Russell, C. T. (2001), Solar wind and interplanetary magnetic field: A tutorial, in *Space Weather*, edited by P. Song, H. J. Singer, and G. L. Siscoe, American Geophysical Union, Washington, D.C., doi:10.1029/GM125p0073.

Russell, C. T. (2005), An introduction to the physics of collisionless shocks, in *4th Annual IGPP International Astrophysics Conference on the Physics of Collisionless Shocks*, edited by G. Li, G. P. Zank, and C. T. Russell, pp. 3–16, AIP Conference Proceedings, Am. Inst. of Phys., Washington, D.C., doi:10.1063/1.2032667.

Russell, C. T., and C. J. Alexander (1984), Multiple spacecraft observations of interplanetary shocks: Shock-normal oscillations and their effects, *Adv. Space Res.*, *4*(2-3), 277–282, doi:10.1016/0273-1177(84)90321-1.

Russell, C. T., M. M. Hoppe, and W. A. Livesey (1982), Overshoots in planetary bow shocks, *Nature*, *296*(5852), 45–48, doi:10.1038/296045a0.

Russell, C. T., J. T. Gosling, R. D. Zwickl, and E. J. Smith (1983a), Multiple spacecraft observations of interplanetary shocks: ISEE three-dimensional plasma measurements, *J. Geophys. Res.*, *88*(A12), 9941–9947, doi:10.1029/JA088iA12p09941.

Russell, C. T., M. M. Mellott, E. J. Smith, and J. H. King (1983b), Multiple spacecraft observations of interplanetary shocks: Four spacecraft determination of shock normals, *J. Geophys. Res.*, *88*(A6), 4739–4748, doi:10.1029/JA088iA06p04739.

Russell, C. T., Y. L. Wang, J. Raeder, R. L. Tokar, C. W. Smith, K. W. Ogivie, A. J. Lazarus, R. P. Lepping, A. Szabo, H. Kawano, T. Mukai, S. Savin, Y. L. Yermolaev, X. Zhou, and B. T. Tsurutani (2000), The interplanetary shock of Septermber 24, 1998: Arrival at Earth, *J. Geophys. Res.*, *105*(A1), 25,143–25,154, doi:10.1029/2000JA900070.

Šafránková, J., Z. Němeček, L. Přech, A. Samsonov, A. Koval, and K. Andréeovaá (2007), Interaction of interplanetary shocks with the bow shock, *Planet. Space Sci.*, *55*(15), 2324–2329, doi:10.1016/j.pss.2007.05.012.

Sagdeev, R. Z., and C. F. Kennel (1991), Collisionless Shock Waves, *Scientific American*, *40*(April).

Samson, J. C., D. D. Wallis, T. J. Hughes, F. Creutzberg, J. M. Ruohoniemi, and R. A. Greenwald (1992), Substorm intensifications and field line resonances in the nightside magnetosphere, *J. Geophys. Res.*, *97*(A6), 8495–8518, doi:10.1029/91JA03156.

Samsonov, A. A. (2011), Propagation of inclined interplanetary shock through the magnetosheath, *J. Atmos. Sol. Terr. Phys.*, *73*, doi:10.1016/j.bbr.2011.03.031.

Samsonov, A. A., Z. Němeček, and J. Šafránková (2006), Numerical MHD modeling of propagation of interplanetary shock through the magnetosheath, *J. Geophys. Res.*, *111*(A082), doi:10.1029/2005JA011537.

Samsonov, A. A., D. G. Sibeck, and J. Imber (2007), MHD simulation for the interaction of an interplanetary shock with the Earth's magnetosphere, *J. Geophys. Res.*, *112*(A12220), doi:10.1029/2007JA012627.

Samsonov, A. A., D. G. Sibeck, and Y. Yu (2010), Transient changes in magnetospheric-ionospheric current caused by the passage of an interplanetary shock: Northward interplanetary magnetic field case, *J. Geophys. Res.*, *115*(A05207), doi:doi:10.1029/2009JA014751.

Schieldge, J., and G. Siscoe (1970), A correlation of the occurrence of simultaneous sudden magnetospheric compressions and geomagnetic bay onsets with selected geophysical indices, *J. Atmos. Sol. Terr. Phys.*, *32*(11), 1819–1830, doi:10.1016/0021-9169(70)90139-X.

Schrijver, C. J., and G. L. Siscoe (2009), *Heliophysics - Plama Physics of the Local Cosmos*, Cambridge University Press, New York.

Schrijver, C. J., R. Dobbins, W. Murtagh, and S. M. Petrinec (2014), Assessing the impact of space weather on the electric power grid based on insurance claims for industrial electrical equipment, *Space Weather*, doi:10.1002/2014SW001066.

Schwartz, S. J. (1998), Shock and discontinuity normals, Mach numbers, and related parameters, in *Analysis Methods for Multi-Spacecraft Data*, edited by G. Paschmann and P. W. Daly, ESA Publications Division, ISSI Scientific Report, Volume 01, Noordwijk, The Netherlands.

Shi, Q. Q., M. Hartinger, V. Angelopoulos, Q.-G. Zong, X.-Z. Zhou, X.-Y. Zhou, A. Kellerman, A. M. Tian, J. Weygand, S. Y. Fu, Z. Y. Pu, J. Raeder, Y. S. Ge, Y. F. Wang, H. Zhang, and Z. H. Yao (2013), THEMIS observations of ULF wave excitation in the nightside plasma sheet during sudden impulse events, *J. Geophys. Res.*, *118*, 284–298, doi:10.1029/2012JA017984.

Siscoe, G. L. (1976), Three-dimensional aspects of interplanetary shock waves, *J. Geophys. Res.*, *81*(34), 6235–6241, doi:10.1029/JA081i034p06235.

Siscoe, G. L., J. M. Turner, and A. J. Lazarus (1969), Simultaneous plasma and magnetic–field measurements of probable tangential discontinuities in the solar wind, *Solar Phys.*, *6*, 456–464, doi:10.1007/BF00146479.

Smith, C., J. L'Heureux, N. Ness, M. Acuña, L. Burlaga, and J. Scheifele (1998), The ACE magnetic fields experiment, *Space Sci. Rev.*, *86*(1–4), 613–632, doi:10.1023/A:1005092216668.

Smith, C. W., K. G. McCracken, N. A. Schwadron, and M. L. Goelzer (2014), The heliospheric magnetic flux, solar wind proton flux, and cosmic ray intensity during the coming solar minimum, *Space Weather*, *12*(7), 499–507, doi:10.1002/2014SW001067.

Smith, E. J. (1973), Identification of interplanetary tangential and rotational discontinuities, *J. Geophys. Res.*, *78*(13), 2054–2063, doi:10.1029/JA078i013p02054.

Smith, E. J. (1983), Observations of interplanetary shocks: Recent progress, *Space Sci. Rev.*, *34*(1), 101–110, doi:10.1007/BF00221200.

Smith, E. J., J. A. Slavin, R. D. Zwickl, and S. J. Bame (1986), Shocks and storm sudden commencements, in *Solar Wind and Magnetosphere Coupling*, edited by Y. Kamide and J. A. Slavin, p. 345, Terra Scientific, Tokyo, Japan.

Sonett, C. P., and I. J. Abrams (1963), The distant geomagnetic field: 3. Disorder and shocks in the magnetopause, *J. Geophys. Res.*, *68*(5), 1233–1263, doi:10.1029/JZ068i005p01233.

Sonett, C. P., E. J. Smith, and A. R. Sims (1960), Surveys of the distant magnetic field: Pioneer I and Explorer IV, in *Proceedings of the First International Space Sciences Symposium*, edited by H. K. Bijl, North Holland Publishing Co., Amsterdam, The Netherlands, doi:10.1002/qj.49708737327.

Spreiter, J. R., A. L. Summers, and A. Y. Alksne (1966), Hydromagnetic flow around the magnetosphere, *Planet. Space Sci.*, *14*(3), 223–253, doi:10.1016/0032-0633(66)90124-3.

Stacey, F. D., and P. M. Davis (2008), *Physics of the Earth*, Cambridge Universuty Press, Cambridge.

Sugiura, M. (1964), Hourly values of equatorial Dst for the IGY, *Ann. Int. Geophys. Year*, *35*(5).

Sun, T. R., C. Wang, H. Li, and X. C. Guo (2011), Nightside geosynchronous magnetic field response to interplanetary shocks: Model results, *J. Geophys. Res.*, *116*(A4), doi:10.1029/2010JA016074.

Sun, T. R., C. Wang, and Y. Wang (2012), Different B_z response regions in the nightside magnetosphere after the arrival of an interplanetary shock: Multipoint observations compared with MHD simulations, *J. Geophys. Res.*, *117*(A05227), doi:10.1029/2011JA017303.

Sun, T. R., C. Wang, J. J. Zhang, V. A. Pilipenko, Y. Wang, and J. Y. Wang (2014), The chain response of the magnetospheric–and–ground magnetic field to interplanetary shocks, *J. Geophys. Res.*, doi:10.1002/2014JA020754.

Szabo, A. (1994), An improved solution to the "Rankine-Hugoniot" problem, *J. Geophys. Res.*, *99*(A8), 14,737–14,746, doi:10.1029/94JA00782.

Szabo, A. (2005), Multi-spacecraft observations of interplanetary shocks, in *4th Annual IGPP International Astrophysics Conference on the Physics of Collisionless Shocks*, edited by G. Li, G. Zank, and C. T. Russell, pp. 37–41, AIP Conference Proceedings, Am. Inst. of Phys., Washington, D.C., doi:10.1063/1.2032672.

Takeuchi, T., C. T. Russell, and T. Araki (2002), Effect of the orientation of interplanetary shock on the geomagnetic sudden commencement, *J. Geophys. Res.*, *107*(A12), 1423, doi:10.1029/2002JA009597.

Thomsen, M. F. (1988), Multi–spacecraft observations of collisionless shocks, *Adv. Space Res.*, *8*(9–10), 157–166, doi:10.1016/0273-1177(88)90126-3.

Tsurutani, B., G. Lakhina, O. Verkhoglyadova, W. Gonzalez, E. Echer, and F. Guarnieri

(2011), A review of interplanetary discontinuities and their geomagnetic effects, *J. Atmos. Sol. Terr. Phys.*, *73*(1), 5–19, doi:10.1016/j.jastp.2010.04.001.

Tsurutani, B. T., and G. S. Lakhina (2014), An extreme coronal mass ejection and consequences for the magnetosphere and Earth, *Geophys. Res. Lett.*, *41*, 287–292, doi:10.1002/2013GL058825.

Tsurutani, B. T., and R. P. Lin (1985), Acceleration of >47 keV ions and >2 keV electrons by interplanetary shocks at 1 AU, *J. Geophys. Res.*, *90*(A1), 1–11, doi:10.1029/JA090iA01p00001.

Tsurutani, B. T., and X. Y. Zhou (2003), Interplanetary shock triggering of substorms: Wind and Polar, *Adv. Space Res.*, *31*(4), doi:10.1016/S0273-1177(02)00796-2.

Tsurutani, B. T., E. Echer, K. Shibata, O. P. Verkhoglyadova, A. J. Mannucci, W. D. Gonzalez, J. U. Kozyra, and M. Pätzold (2014), The interplanetary causes of geomagnetic activity during the 7-17 March 2012 interval: A CAWSES II overview, *J. Space Weather Space Clim.*, *4*(A02), doi:10.1051/swsc/2013056.

Viñas, A. F., and J. D. Scudder (1986), Fast and optimal solution to the "Rankine-Hugoniot" problem, *J. Geophys. Res.*, *91*(A1), 39–58, doi:10.1029/JA091iA01p00039.

Wang, C., Z. H. Huang, Y. Q. Hu, and X. C. Guo (2005), 3D global simulation of the interaction of interplanetary shocks with the magnetosphere, in *4th Annual IGPP International Astrophysics Conference on the Physics of Collisionless Shocks*, edited by G. Li, G. Zank, and C. T. Russell, pp. 320–324, AIP Conference Proceedings, Am. Inst. of Phys., Washington, D.C., doi:10.1063/1.2032716.

Wang, C., C. X. Li, Z. H. Huang, and J. D. Richardson (2006), Effect of interplanetary shock strengths and orientations on storm sudden commencement rise times, *Geophys. Res. Lett.*, *33*(14), doi:10.1029/2006GL025966.

Wang, C., J. B. Liu, H. Li, Z. H. Huang, J. D. Richardson, and J. R. Kan (2009), Geospace magnetic field responses to interplanetary shocks, *J. Geophys. Res.*, *114*(A5), doi:10.1029/2008JA013794.

Wang, C., H. Li, J. D. Richardson, and J. R. Kan (2010), Interplanetary shock characteristics and associated geosynchronous magnetic field variations estimated from sudden impulses observed on the ground, *J. Geophys. Res.*, *115*(A9), doi:10.1029/2009JA014833.

Wang, C., X. G. H. Li, K. Ding, and Z. Huang (2012), Numerical study on the response of the Earth's magnetosphere-ionosphere system to a super solar storm, *Science China: Earth Sciences*, *55*(6), 1037, doi:10.1007/s11430-012-4405-4.

Whang, Y. C. (1982), Slow shocks around the Sun, *Geophys. Res. Lett.*, *9*(9), 1081–1084, doi:10.1029/GL009i009p01081.

Whang, Y. C. (1983), Corotating shocks in the inner heliosphere, in *Solar Wind Five*, p. 719, NASA Conf. Publ., CP 2280.

Whang, Y. C., J. Zhou, R. P. Lepping, and K. W. Ogilvie (1996), Interplanetary slow shock observed from WIND, *Geophys. Res. Lett.*, *23*(10), 1239–1242, doi:10.1029/96GL01358.

Wu, C.-C., S. T. Wu, and M. Dryer (1996), Generation and evolution of interplanetary slow shocks, *Ann. Geophys.*, *14*, 375–382, doi:10.1007/s00585-996-0375-1.

Yan, M., and L. C. Lee (1996), Interaction of interplanetary shocks and rotational discontinuities with the Earth's bow shock, *J. Geophys. Res.*, *101*(A3), 4835–4848, doi:10.1029/95JA02976.

Yue, C., Q. G. Zong, H. Zhang, Y. F. Wang, C. J. Yuan, Z. Y. Pu, S. Y. Fu, A. T. Y. Lui, B. Yang, and C. R. Wang (2010), Geomagnetic activity triggered by interplanetary shocks, *J. Geophys. Res.*, *115*(A5), doi:10.1029/2010JA015356.

Zhang, H., D. G. Sibeck, Q.-G. Zong, J. P. McFadder, D. Larson, K.-H. Glassmeier, and V. Angelopoulos (2012), Global magnetosphere response to an interplanetary shock: THEMIS observations, *Ann. Geophys.*, *30*(2), 379–387, doi:10.5194/angeo-30-379-2012.

Zhou, X., and B. T. Tsurutani (2001), Interplanetary shock triggering of nightside geomagnetic activity: Substorms, pseudobreakups, and quiescent events, *J. Geophys. Res.*, *106*(A9), 18,957–18,967, doi:10.1029/2000JA003028.

Zhou, X.-Y., and E. J. Smith (2015), Supercriticality of ICME and CIR shocks, *J. Geophys. Res.*, *120*(1), doi:10.1002/2014JA020700.

Zhou, X.-Y., and B. T. Tsurutani (1999), Rapid intensification and propagation of the dayside aurora: Large scale interplanetary pressure pulses (fast shocks), *Geophys. Res. Lett.*, *26*(8), 1097–1100, doi:10.1029/1999GL900173.

Zhou, X.-Y., R. J. Strangeway, P. C. Anderson, D. G. Sibeck, B. T. Tsurutani, G. Haerendel, H. U. Frey, and J. K. Arballo (2003), Shock aurora: FAST and DMSP observations, *J. Geophys. Res.*, *108*(A4), doi:10.1029/2002JA009701.

Zong, Q.-G., X.-Z. Zhou, Y. F. Wang, X. Li, P. Song, D. N. Baker, T. A. Fritz, P. W. Daly, M. Dunlop, and A. Pedersen (2009), Energetic electron response to ULF waves induced by interplanetary shocks in the outer radiation belt, *J. Geophys. Res.*, *114*(A10), doi:10.1029/2009JA014393.

Zurbuchen, T. H., and I. G. Richardson (2006), In-situ solar wind and magnetic field signatures of interplanetary coronal mass ejections, *Space Sci. Rev.*, *123*(1-3), doi:10.1007/s11214-006-9010-4.